

## ABSTRACT

HAN, YIWEI. High-Resolution Electrohydrodynamic (EHD) 3D Printing of Function Materials (Under the direction of Dr. Jingyan Dong)

This study focuses on developing high-resolution printing processes for multi-functional materials. First, we investigated a high-resolution EHD printing technology for the fabrication of micro-scale 3D structures with phase change ink. A series of experiments have been performed to characterize the EHD printing process. In this study, the droplet size and droplet printing frequency can be directly determined by the applied voltage. For a better controlling of the printing frequency and droplet size, a DC pulse voltage based printing process was developed and characterized. We also characterized the printing process using AC voltage, which allows neutralizing the charges on the droplets and will benefit high-resolution 3D printing especially with conductive material on insulating substrates. After finding the optimal parameters for the e-jet printing, a few 3D structures were directly fabricated with good quality and high-resolution.

To understand the mechanism of the drop-on-demand EHD printing, FEA-based simulation models were created, which is capable of modeling drop-on-demand printing process that ranges from droplet formation to droplet spreading and settlement on the substrate. In-field experiments were performed to verify the simulation results, with the printed droplet volume and footprint measured by the Atomic Force Microscope (AFM). It was shown that the simulation results have a good match with the experiment results, which validates the created models. This model not only gives a better understanding of the mechanism of EHD printing but also provide valuable guidelines to control the printing process as it has the potential to be used to predicate droplet size under different conditions.

In the traditional EHD printing system, a substrate is placed between the ground electrode and the printing nozzle, which limits the maximum height of the printed structures. In order to have substrate independent printing, a ring electrode was designed and fabricated in this study. The ring electrode has a circular hole in the middle of a thin glass slide coated with conductive material. This grounded ring electrode was integrated into the printing nozzle that free the ground electrode under the substrate in the traditional printing system. FEA simulations were performed to find the best design parameters that can provide the enough electric field to start EHD printing. With the help of the FEA model, the best design parameters can be found, and with this new electrode design, high-resolution 3D structures with large aspect ratio can be fabricated.

Lastly, this study investigated high-resolution EHD fabrication of flexible and stretchable conductors with two advanced materials. The first material is low melting point metal alloy. A high-resolution EHD printing process was developed and characterized for the molten metal, which was capable of producing metallic features with a sub-50 $\mu$ m resolution. High-resolution 2D patterns and 3D structures have been printed to demonstrate the printing capability for flexible and stretchable electronics. Bending test and stretching test of the printed conductors showed the excellent performance on the flexibility and stretchability. A high-resolution and high-density capacitance sensor has been successfully printed and tested. An FEA model was created to simulate the behavior of the capacitance sensor. The second material is one dimensional AgNW. An EHD printing process was developed for the AgNW ink. To obtain the best formula of the ink, different AgNW inks were synthesized and tested. With the optimal printing conditions, features with linewidth less than 50 $\mu$ m were successfully printed. The printed AgNW features have the best conductive of  $5.6 \times 10^6$  S/m. Bending test and stretching test

showed excellent performance in both flexibility and stretchability. Two wearable devices were fabricated and tested to demonstrate the potential application of this EHD printing technique for AgNW based flexible and stretchable devices.

© Copyright 2018 by Yiwei Han

All Rights Reserved

High-Resolution Electrohydrodynamic (EHD) 3D Printing of Function Materials

by  
Yiwei Han

A dissertation submitted to the Graduate Faculty of  
North Carolina State University  
in partial fulfillment of the  
requirements for the degree of  
Doctor of Philosophy

Industrial and Systems Engineering

Raleigh, North Carolina

2018

APPROVED BY:

---

Jingyan Dong  
Committee Chair

---

Paul Cohen

---

Yuan-Shin Lee

---

Yong Zhu

**DEDICATION**

To my family

To the girl I love, Mengqi Xing

## **BIOGRAPHY**

Yiwei Han received B.S. degree in Industrial and Manufacturing Engineering from North Dakota State University in 2013. Then in 2013, he joined Prof. Jingyan Dong's group in Edward P. Fitts Department of Industrial and Systems Engineering at North Carolina State University. His research focuses on the Electrohydrodynamic (EHD) high-resolution 3D printing technology for multi-function materials, modeling for EHD printing, and printing system design for the EHD printing process.

## ACKNOWLEDGMENTS

First of all, I would like to express my most profound appreciation to my advisor, Prof. Jingyan Dong for his knowledge, guidance, and support in the last five years. I also would like to express my gratitude to my committee, Prof. Paul Cohen, Prof. Yuan-shin Lee, and Prof. Yong Zhu for their valuable thoughts and feedback. In addition, I would like to thank Prof. Mohamed Bourham for taking the role of Graduate School representative on my committee.

I would like to thank my talented and motivated colleagues, Yang Cao, Zheng Cui, Jia Deng, Xiangcheng Kong, Kai Liu, Hantang Qin, Ping Ren, Chuang Wei, and Shanshan Yao for their support. It is also fun to have you around, Xingbo Du, Rui Liu, Xubiao Wei, Ling Zhang, Last, I would like to thank all the people that helped and supported me in this five years. My work would never be accomplished without you.

## TABLE OF CONTENTS

LIST OF TABLES .....	vii
LIST OF FIGURES .....	viii
<b>CHAPTER 1 INTRODUCTION.....</b>	<b>1</b>
1.1 Motivation .....	1
1.2 Research Objectives and Scope.....	4
1.3 Dissertation Outline.....	8
1.4 Chapter Summary.....	8
<b>CHAPTER 2 LITERATURE REVIEW.....</b>	<b>9</b>
2.1 Overview of Traditional Additive Manufacturing .....	9
2.1.1 Liquid Based Additive Manufacturing .....	9
2.1.2 Solid Based Additive Manufacturing .....	13
2.1.3 Powder Based Additive Manufacturing.....	14
2.2 Overview of Current Printing Technologies .....	19
2.2.1 Inkjet Printing .....	20
2.2.2 EHD Printing .....	21
2.2.3 pyroelectrodynamic printing.....	21
2.2.4 Saw Printing.....	22
2.2.5 Screen Printing.....	23
2.2.6 Offset Printing .....	24
2.2.7 Gravure Printing .....	25
2.3 Overview of EHD Printing Technology.....	26
2.4 Chapter Summary.....	31
<b>CHAPTER 3 HIGH-RESOLUTION EHD 3D STRUCTURE PRINTING.....</b>	<b>32</b>
3.1 EHD 3D Printing System and Material.....	32
3.1.1 Printing Material.....	32
3.1.2 Printing System.....	33
3.1.3 Pattern Characterization.....	35
3.2 EHD Printing Processes and Characterization Under Continous DC voltage .....	36
3.3 EHD Printing Process Under Controlled Voltage.....	39
3.3.1 EHD printing process under DC pulsed voltage.....	39
3.3.2 EHD printing process under AC voltage .....	46
3.4 EHD 3D Structures Printing.....	50
3.5 Chapter Summary.....	53
<b>CHAPTER 4 MODELING OF EHD 3D PRINTING PROCESS.....</b>	<b>55</b>
4.1 Modeling for Droplet Formation.....	55
4.2 Modeling for Droplet In-Flight Velocity .....	55
4.3 Modeling of Droplet Settlement on Substrate.....	65
4.4 Modeling Results of EHD Printing .....	67
4. 5 Chapter Summary.....	70
<b>CHAPTER 5 Ring Electrode Design for EHD Printing.....</b>	<b>71</b>
5. 1 EHD 3D Printing System with Ring Electrode .....	71
5.1.1 EHD Printing System .....	71

5.1.2 Printing Material .....	72
5. 2 Ring Electrode Design .....	72
5. 3 FEA Modeling of Ring Electrode Design .....	75
5.4 Characterization of Ring Electrode Design.....	82
5.4.1 Verification of Ring Extractor Design.....	82
5.4.2 Characterization of EHD printing using Ring Extractor .....	85
5.5 EHD Filament Printing of 3D Structures .....	89
5. 6 Chapter Summary.....	90
<b>Chapter 6 EHD printing of electronics with advanced materials .....</b>	<b>92</b>
6.1 High-resolution EHD direct metal printing of electronics .....	93
6.1.1 printing system and printing material .....	93
6.1.2 EHD Metal printing process and characterization.....	95
6.1.3 Direct molten metal printing of 2D and 3D features .....	101
6.1.4 Direct Fabrication of Flexible and Stretchable Conductors .....	103
6.2 EHD printing of electronics with silver nanowire .....	114
6.2.1 EHD printing of AgNW.....	114
6.2.2 Morphology and Electrical Properties of Printed AgNW.....	118
6.2.3 EHD Printing of AgNW Devices .....	123
6.3 Chapter Summer.....	125
<b>CHAPTER 7 FUTURE WORK, SUMMARY AND TIMELINE .....</b>	<b>128</b>
7.1 Research Summary.....	128
7.2 Future Work .....	131
<b>References .....</b>	<b>133</b>

**LIST OF TABLES**

Table 6.1 AgNW density at the center and along the edge at two different printing speeds.....	119
---	-----

## LIST OF FIGURES

Figure 2.1	Principle of FDM process [44].....	10
Figure 2.2	Schematic of polyjet 3D printing process [50].....	11
Figure 2.3	Schemes of two types of stereolithography systems. (a) Laser-based (b) digital light projection.[54].....	12
Figure 2.4	(a) Mechanism of the LOM machine. (b)LOM building process. [70].....	13
Figure 2.5	3D printing process: 1 and 2 place a layer of powder. 3 Binder is printing to this powder layer. 4 The whole will be repeated for every layer [73] .....	14
Figure 2.6	Schematic of LENS system setup [77].....	16
Figure 2.7	Schematic of EBM system setup [82] .....	17
Figure 2.8	Schematic overview of SLS system [90]. .....	18
Figure 2.9	Schematic of SLM system setup [96].....	19
Figure 2.10	Schematic of drop on demand inkjet printing [97].....	20
Figure 2.11	(a) Schematic of the pyroelectrodynamic printing system, including two plates and a heat source. (b) Droplet deposited onto substrate.[106].....	22
Figure 2.12	Schematic of nanoscale wave propagation and atomization [108]. .....	23
Figure 2.13	Schematic of the screen printing process [111].....	24
Figure 2.14	Schematic of the offset printing process [111].....	25
Figure 2.15	Schematic of the gravure printing process [112].....	25
Figure 2.16	EHD printing system set-up [7].....	28
Figure 3.1	Schematic of the EHD printing set-up.....	33
Figure 3.2	(a) interchangeable nozzle base (b) Nozzle glued with base (c) Syringe.....	35
Figure 3.3	(a) Cone-shape at initial start voltage under pulsation mode (b) Printed larger size droplet at initial start voltage. (Scale bar 50 $\mu$ m).....	37
Figure 3.4	(a) Cone shape at voltage of 850V. (b) Droplet size and printing frequency at different positive voltages (Droplet size from top to bottom: 17 $\mu$ m, 14 $\mu$ m, 11 $\mu$ m, 8 $\mu$ m) .....	38

Figure 3.5	(a) Printed satellite droplets (b) Multi-jet in EHD printing. Scale bar: 100 $\mu\text{m}$ . .....	39
Figure 3.6	The regular DC pulsed voltage signal .....	40
Figure 3.7	The result of printed droplet under pulsed DC voltage with different voltage amplitudes; (scale bar: 50 $\mu\text{m}$ ) .....	41
Figure 3.8	The result of printed droplet under pulsed DC voltage with different duty cycles (scale bar: 50 $\mu\text{m}$ ) .....	42
Figure 3.9	The result of printed droplet under pulsed DC voltage with different pulse frequencies. (Scale bar: 25 $\mu\text{m}$ ) .....	43
Figure 3.10	Different combinations of voltage and duty cycle for a printing frequency of 50Hz. (scale bar: 50 $\mu\text{m}$ ) .....	44
Figure 3.11	(a) The modified DC pulsed voltage signal (b) 50Hz of printing frequency under voltage of 1250V (scale bar: 50 $\mu\text{m}$ ) .....	45
Figure 3.12	(a) Square AC voltage signal pattern (b) generated square AC voltage in function generator .....	47
Figure 3.13	Printing result under different AC voltage frequency (Scale bar: 50 $\mu\text{m}$ ) .....	48
Figure 3.14	Printed droplet under continuous DC voltage of (a) 900V and (b) - 900V .....	49
Figure 3.15	Printed droplet under different duty cycle (a) 60% positive voltage and 40% negative voltage (b) 70% positive voltage and 30% negative voltage .....	50
Figure 3.16	Micro-structures printed from EHD printing process (a) pyramid (b) Single layer wall (c) Rectangle tube (d,e) circular tube with thin walls. (f) Close view of a single pillar (g,h ) Micro-pillar array matrix (i) 3D letter of NCSU. ....	51
Figure 4.1	Schematic configuration for FEA modeling of the electrostatic force and surface tension on the droplet .....	57
Figure 4.2	(a) The created model for the simulation (b) and (c) The zoomed in picture around the nozzle tip. ....	58
Figure 4.3	The model after applying voltage load to the nozzle and bottom surface of the substrate. ....	59
Figure 4.4	(a) The picture of the model after solved. (b) and (c) The electric field distribution round the meniscus. (d) Electric field intensity around the nozzle tip during droplet ejection. ....	60

Figure 4.5	FEA model of droplet in-flight between tip and substrate. ....	62
Figure 4.6	(a) Electric field distribution along center axis. (b) The amount of charge of droplet under different voltages. (c) Droplet velocity under different voltage and different flight time (d) Droplet impact velocity with different printing voltages.....	63
Figure 4.7	Modeling of the four stages (a) Initial statue of droplet impact (b) Droplet impact on substrate. c) Droplet spreading on substrate surface. d) Droplet settlement and solidification.....	66
Figure 4.8	(a) In-flight droplet before impact the substrate. (b) Initial impact of the droplet on substrate. (c) Droplet spreading on substrate surface. (d) Droplet settlement and solidification.....	68
Figure 4.9	Comparison between droplets height (a) and diameter (b) from FEA (lines) and experimentally measured results (data points) at different process conditions. (c) Experimentally measured droplet cross section on substrate. (Unit of x and y coordinates is $\mu\text{m}$ , and measurement is shown as red line). ....	69
Figure 5.1	Schematic of EHD printing system with a ring extractor.....	72
Figure 5.2	(a) Schematic of ring extractor design. (b) Ring extractor and tip picture that taken from experiment camera. ....	73
Figure 5.3	(a) Microscope cover glass (b) Vertical view of the cover glass .....	74
Figure 5.4	Schematic configuration for FEA modeling of the electrostatic force on droplets. ....	76
Figure 5.5	(a) Electric field potential distribution (b) electric field strength around the printing tip of non-extractor at 825v with a standoff of 150 $\mu\text{m}$ (unit of the scale bar is $\text{V}/\mu\text{m}$ ).....	77
Figure 5.6	(a) (b) FEA model of the cross-section of the nozzle, ring extractor, ejected material and substrate. (c) Electric field strength around the printing tip at 1600V (unit of the scale bar is $\text{V}/\mu\text{m}$ ). ....	78
Figure 5.7	The relationships between the electric field strength and (a) standoff height, (b) ring diameter, and (c) tip to ring extractor z-distance. ....	80
Figure 5.8	The printing behavior at the nozzle tip (a) without ring-extractor at 1s, 7s, and 20s, and (b) with ring-extractor at 1s, 3.5s, and 9s.....	83
Figure 5.9	Printed filaments at different voltage from 1400v to 1800v (scale bar: 100 $\mu\text{m}$ ). ....	86

Figure 5.10	Printed filaments under different printing speed from 10mm/s to 20mm/s (Scale bar: 100 $\mu$ m) .....	88
Figure 5.11	EHD filament printing of 3D microstructures. (a) Thin wall structure with a tilt angle of 45 degree. (b) Thin wall structure with a tilt angle of 80 degree. (c) Thin wall structure from top view. (d) Ring structure. (e) Square corner. (f) Top view of a square corner. ....	90
Figure 6.1	Schematic of EHD printing system .....	93
Figure 6.2	(a) large droplet of molten metal ink extruded under a pressure of 5 psi at the nozzle tip. (b) Optical image of the pneumatically extruded metal filaments at printing speed of 20, 25, 30, 35, 40, 45, 50mm/s respectively from top to bottom with a constant pressure of 10 psi. Scale bar: 5mm .....	95
Figure 6.3	(a) EHD printing behavior around the nozzle (b) EHD printed metallic filaments on glass at different voltage of 500, 1500, 1600, 1700, 1800, 1900, 2000V respectively from top to bottom. (c) Printed metallic filaments on glass substrate at printing speeds pf 0.5, 1, 1.5, 2, 3, 4mm/s respectively from top to bottom (d) Line width of the EHD printed filaments as a function of the printing voltage at constant printing speed of 0.5mm/s. (e) Line width of the EHD printed filaments as a function of the printing speed at a constant voltage of 1900V. Scale bar: 500 $\mu$ m.....	97
Figure 6.4	(a) to (c) EHD printed patterns from Field's metal, Wood's metal and solder on different substrates (from left to right: microscope glass slide, PDMS, PET, photo paper) (d) Contact angle for different materials on different substrates. (e) Contact angle between Field's metal and PDMS substrate. Scale bar: 5mm .....	100
Figure 6.5	(a) EHD printed high-resolution 2D patterns (b) Vertical metal wire (c) Metal bridge structure. (d) Thin wall. Scale bar: 500 $\mu$ m .....	102
Figure 6.6	(a) EHD printed conductor on PDMS with a Christmas tree pattern that connected a battery to light a LED (Sale bar: 500 $\mu$ m). (b) The conductor remained conductive at the bending state. (c) Resistance of the Christmas tree conductor as a function of bending diameter. (d) Resistance of the Christmas tree conductor as a function of the number of bending tests at the bending diameter of 10mm and 5mm.....	104
Figure 6.7	(a) Optical image of printed different designed conductor pattern (from top to bottom: a straight-line, Half-circle, and horseshoe.) (b) Resistance changes as a function of tensile strain (0-70%) for three different designed pattern. (c) Optical image of a metallic conductor with horseshoe pattern under tensile strains of 0%, 25%, 50%. (d) Resistance as a function of tensile strain (0-70%) for the metallic conductor from the first to fifth stretching cycles. ....	106

- Figure 6.8 (a) and (b) Printed feature before and after healing process (c) Optical image of break point in the printed feature before and after healing. (e) Bended feature after healing process (f) Horseshoe pattern on stretching test table (g) and (h) optical image of break point in half circle pattern before and after healing (i) Resistance as function of tensile strain in the initial to third time of healing process. .... 108
- Figure 6.9 (a) schematic of printed touch sensor. (b) Working principle of touch sensor matrix. (c) Optical images and SEM image of a 20x20 touch sensor array and compared with a one cent coin. (d) A microcontroller board (ARDUINO MEGA 2560) was used to map the signal from 4x4 touch sensors array to a 4x4 LED matrix. (e) The change of the capacitance when touch point under different sampling point. (f) and (g) Activated LED on point 1 and point 2. .... 111
- Figure. 6.10 (a) FEA model for touch sensor design. (b) Cross section of electric potential of touch sensor with and without a touch pen (c) Simulation result of the changing capacitance ( $\Delta C$ ) of points when the touch pen touch red point (point 1) (unit: pF). .... 113
- Figure 6.11 (a) and (b) Printing behavior for extrusion printing and EHD printing. Scale bar: 150 $\mu$ m. (c) Three different high-resolution AgNW patterns. (d) Large-scale AgNW pattern printed by EHD method. Scale bar: 5mm. .... 116
- Figure 6.12 (a) and (b) Printed line width as a function of printing speed and stand-off. (c) Optical image shows the clean and smooth edge. Scale bar: 50 $\mu$ m. .... 117
- Figure 6.13 AgNW alignment at edge and center of the printed line with a printing of (a) 10mm/s and (b) 1mm/s. Scale bar: 10 $\mu$ m ..... 118
- Figure 6.14 (a) The resistance of printed AgNW lines with different line widths. (b) The conductivity of the printed AgNW lines with different line widths. .... 120
- Figure 6.15 Optical image of printed AgNW lines on various substrates. (a) (a) Printed on a variety of substrates (a) letter paper, (b) glass, (c) PET, (d) nanofiber paper, (e) PDMS and (f) polycarbonate filter. .... 121
- Figure 6.16 (a) Optical image of bending test of bending angle from 0° to 180°. (b) Resistance of printed AgNW pattern under different bending curvature. (c) Resistance under 200 bending cycles with a bending curvature of 0.37 (bending radius 2.7mm). (d) Resistance as a function of different strain under different stretching and releasing cycle. (e) Resistance under 300 cycles of stretching and releasing ..... 122
- Figure 6.17 (a) IR image of printed AgNW heater under activated/de-activated condition. Scale bar: 5mm (b) IR image of AgNW heater printed on a lab-use gloves. .... 124

Figure 6.18	(a) Printed dry ECG on PDMS film. Scale bar: 5mm. (b) ECG signals collected from the AgNW dry ECG electrode and a commercial 3M wet electrode for comparison .....	125
-------------	--	-----

## CHAPTER 1 INTRODUCTION

### 1.1 MOTIVATION

Additive manufacturing [1-5] has the capability for rapid prototyping and small volume production of components for many applications such as aerospace, medical device fabrication, electronic device fabrication and automotive industries. Most of the existing additive processes, including selective laser sinter (SLS), electron beam melting (EBM), stereolithography, 3D printing, and fused deposition modeling (FDM) have the best resolution of no better than 50 $\mu$ m, and the improvements of their resolutions are usually very challenging. For example, for laser or electron beam based additive manufacturing, the resolution is limited by the beam or laser spot size; for extrusion-based additive manufacturing, the resolution is limited by the nozzle size; for particle-based technology, the used particle size will limit the fabrication resolution, and in order to improve those require large energy, high investment cost, high material requirement, high pressure, etc.

High-resolution additive manufacturing is critical for many engineering applications. Lousy accuracy and surface finishing part will significantly limit the applications of the current additive manufacturing process in the production of high precision parts. The high-resolution 3D printing can provide high accuracy and quality surface finishing, which can effectively reduce the post-processing time and cost. High-resolution printing technology can also reduce the complexity of manufacturing process in many industrial areas such as aerospace, automotive, healthcare, etc. For instance, in the aerospace industry, with the high precision printing technology, tiny fuel injection nozzle and high precision parts in the engine turbo can be directly printed, which reduce a significant amount of material waste, simplified the manufacturing process and save a lot of time. In the healthcare, especially in the dental area, high precision

printing allows printing the unique model for different patients without increasing any workload when compared with traditional manufacturing technologies. In the tissue engineering, the biocompatible scaffolds are crucial to support cell functions and regulate cell response to the scaffold such as cell alignment and cell contact guidance [6,7].

EHD printing [8-10] has been developed for several decades, and it is a high-resolution printing approach, in which the ink is subjected to the electric field to form a Taylor-cone and produce fine jet or droplet from the apex of the cone, thus to overcome the limitation from the nozzle size in tradition 3D printing. Drop-on-demand EHD printing with phase change ink has a unique advantage of quick solidification after printed on the substrate that would provide a promising process for micro-scale 3D structure fabrication. For other widely used aqueous or solvent-based inks, usually a small portion of functional materials can be preserved after solvent evaporation or post-process, which leads to a very low layer thickness of the printed feature. However, with phase-change ink, the printed layer will have a higher thickness about  $1\mu\text{m}$  that usually hundred times larger than that using aqueous or solvent-based inks. The reason is that phase-changed ink will get solidified very quickly once it printed on the substrate; and with the short solidification time, limited ink spreading will also result in a higher thickness.

Currently, most of the EHD printing process are focused on the one dimension or two dimension printing, and only a few of the research has investigated the 3D EHD printing [11,12], so it is a great challenge to develop a 3D multi-materials EHD printing process that has the ability to printing arbitrary 3D structures. Though lots of efforts have been put into EHD printing, truly understanding of the mechanism of the EHD printing is still unsolved. Some of the researchers have developed some models to simulate EHD printing processes, but most of the models are limited by many aspects, which cannot apply to other conditions, so a universal

model should be created for EHD printing process, which can apply to more general printing conditions. For the traditional planar EHD print 3D structure, the process is becoming more and more difficult to control, and the height of printed parts is also limited because of the ground electrode is placed under the substrate, which makes this printing process not substrate independent. So a new printing system has to be developed for EHD printing, and this system can overcome the substrate effect and standoff distance (distance between the substrate and the nozzle), which can allow the system to print higher structure with better controllability and process stability.

Flexible and stretchable electronics are vital for the next generation electrical devices, but the materials used for printing electronics such as metal nanoparticles [13-15], conductivity polymers [16-18] and liquid metal [19-24] are either expensive or low conductivity or low resolutions. Moreover, most of the fabrication approaches for those materials need post-treatment, which increase the fabrication time and cost. Currently, only a few research investigated direct writing of molten metal [14,25-27] for the fabrication of electronics but also with limited resolution. Since EHD printing has the potential to provide high-resolution and cost-effective printing, molten metallic materials can be applied to this method for fabrication of high-resolution and high conductivity flexible and stretchable electronics. Metallic nanowires is another advanced material for fabrication of flexible and stretchable electronics because a random network of nanowires can provide high conductivity and good flexibility and stretchability [28-32]. Longer nanowires can lead to even higher conductivity and provide a good optical transmittance [33], which is critical for fabrication of transparent electrodes. However, for most of the printing methods [29,34-39], it is very difficult to produce high-resolution and good conductivity nanowire features at the same time. For example, for inkjet printing, based on

the “rule of thumb,” the size of the particles in ink is suggested not to exceed 1/100 times of the nozzle size to prevent from nozzle clogging, the printed resolution is limited by the nozzle size. Since EHD printing does not require very small nozzle to produce high-resolution, it is an ideal technique for printing of AgNW based flexible and stretchable electronics. Few studies have investigated the EHD printing with metallic nanowires. However, they are focusing on the alignment of the NWs, which has a very low NWs density in ink and the printed lines are not conductivity.

This study is focused on developing a high-resolution EHD 3D printing process using polymeric and metallic materials; modeling of drop-on-demand EHD printing process and a new printing head model to simulate the EHD printing process; developing EHD printing process for the fabrication of high-resolution flexible and stretchable electronics. These research objectives and the scope of this research are discussed in the following section.

## **1.2 RESEARCH OBJECTIVES AND SCOPE**

The broader objective of this dissertation is to develop a new printing method, which can provide high-resolution DoD printing; create a model that will give a hand to better understand the insight of the printing mechanism and process optimization; design a new printing head for substrate-independent printing; apply EHD technology to metal nanowire to fabricate high-resolution flexible and stretchable electronics; and high-resolution direct EHD printing of molten metal to fabricate 3D structure and electronics.

The specific objective of this dissertation proposals are as follows:

- To understand the affection of different printing conditions to the printing process, a series of EHD printing characterization tests will be performed to find the relationship between droplet size, printing frequency, and other printing parameters. The overall characterization

process will be performed for printing with different types of printing voltages, DC voltage, and AC voltage. In DC voltage characterization, two different types of voltage signal will be applied to the system. When using the regular DC voltage signal in printing, the characterization will focus on the influence of the voltage amplitude to the droplet size and droplet printing frequency. When using the DC pulsed voltage signal, three main parameters (voltage amplitude, pulse frequency, and duty cycle) will affect the droplet size and printing frequency, and each of those parameters will be characterized in the experiments. When using the DC voltage, the printed droplet will contain charges especially for printing on a highly insulating substrate. In order to reduce the charges, an AC voltage will be introduced for printing process. In the characterization process for using AC voltage, three parameters (voltage amplitude, frequency, and duty cycle) will be investigated for finding the relationship between those parameters and droplet size and ejection frequency.

- Process models will be developed to simulate the overall EHD printing process that includes droplet formation around the meniscus, droplet inflight in the electric field between the nozzle and substrate, droplet impact and spreading on the substrate and final droplet solidification. Due to the highly complex mechanism of this printing process, only the pending state of droplet detaching from the apex of the meniscus will be studied in the droplet formation stage. The droplet formation phase will be modeled by Finite Element Analysis (FEA) with respect to the surface tension force and electrostatic force on the pending droplet, and the simulation results will be compared with the experiment results, which can be observed from Atomic Force Microscope (AFM). If there is a good match between the experiment result and the simulation result that will indicate that model has a good fit to the printing process, and it can provide a guideline to predict the droplet dimension with given printing parameters. Droplet in-

flight velocity is also simulated by FEA, and the simulated final droplet impact velocity will be used for the droplet impact and spreading phase. Droplet impact spreading and solidification will be simulated together, and the simulation results will be used to compare with the experiment results for validation. If the final experiment results have reasonable agreement with the simulation result, which indicated that this printing model has the capability to predicate the final droplet size and shape.

- For E-jet 3D printing, the most significant challenge is that the printing system is not substrate independent. The ground electrode is normally placed under the substrate. While building the structure layer by layer, the built structure will distort the electric field and cause an unstable printing condition because of the distorted field from the uneven surface. This will make the whole printing process difficult to control. In order to solve this problem, an integrated ring ground electrode will be designed for the printing system. The ring electrode will be combined with the printing nozzle that will free the traditional planar ground electrode and make this printing system substrate independent so that the substrate and the printed structure will have zero or less effect to the printing system. The new printing head design will be first designed and studied using the FEA to find the optimal design parameters, and then the design will be validated by experimental tests. If promising experimental results could obtain, which indicate that this design could overcome the difficulty of the traditional electrode setup, and improve the stability and controllability of the printing system effectively. 3D structures with high aspect ratio can also be fabricated with this integrated ring electrode design

- Currently, the materials used in EHD printing are mostly liquid-phase inks. Many of the conductive materials such as conductive polymer, metal nanoparticles, metal nanowires, and nanotubes are used in EHD printing. However, the cost of those materials is tremendous, and the

production efficiency is low especially in large scale electronics traditional production. Directly metal printing can provide low cost with high fabrication efficiency. However, most of the printing technologies cannot provide high-resolution, which is not suitable to be used in micro-fabrication industry. Here, the EHD printing technologies will be applied to the molten metal ink. The overall printing process will be studied in the first place to find out the best combination of printing voltage, printing speed, temperature, back pressure, and standoff distance. Then 3D metallic structures will be fabricated to demonstrate the capability of EHD printing in 3D printing. Moreover, electronic devices will be produced to illustrate its ability to produce high-resolution micro-scale electronics using EHD printing technology. Bending, stretching, and self-healing test will be performed for the printed features to find their best performances.

- A few groups have investigated the printing metal nanowires using EHD technology. However, the printed features with nanowires in the filament is not conductive because of the low density of the nanowire, which does not suitable for electronic fabrications. High-resolution printing will benefit micro-electronic industry in the aspect of reducing post-process, high conductivity features, and low cost. The material used in EHD printing is the solution that mixed silver nanowires and PEO solution. The different concentrations of the PEO will be first printed and characterized. Then, the different concentrations of AgNW will be mixed with the chosen concentration of PEO solution to find the optimal AgNW density. After obtained the value to AgNW density and PEO concentration, the characterization process will focus on the voltage amplitude, printing speed, and applied back pressure. With the optimal printing parameters, conductive features will be printed for bending and stretching test. Last, some high-resolution micro-scale electronics such as ECG and heater will be fabricated and tested for their performances.

### **1.3 DISSERTATION OUTLINE**

This dissertation proposal is composed of seven chapters. Chapter 2 is the literature review which includes traditional additive manufacturing, current printing technologies, and EHD printing technology. In the EHD printing review section, some limitations have been pointed out and which will be solved in this research. Chapter 3 first discussed the characterization process for high-resolution EHD printing. The characterization includes printing process under both DC and AC voltage. Then the 3D structure printing process is discussed in the next part of chapter 3. In order to better understand the mechanism of the EHD printing, in chapter 4, an EHD printing model was developed for simulating of EHD printing process from droplet formation at the apex of the nozzle to the final droplet settlement on the substrate. The simulation results have a good match with the experimental results that indicate that this model can be used to predicate the droplet footprint under different given printing parameters. Chapter 5 presented an integrated designed of printing nozzle, which can overcome the substrate limitation. The designed printing head was a substrate independent, which can improve the stability and controllability of the printing processes. The chapter 6 will discuss high-resolution EHD printing of molten metal and AgNW for fabrication of flexible and stretchable electronics. The chapter 7 will summarize the research and discussion about the expected research contributions and some of the future works.

### **1.4 CHAPTER SUMMARY**

This chapter discusses the research motivation of developing a new 3D printing technology for function materials, which can print high-resolution micro-scale 3D structures and their applications. The detailed research objective was proposed in the following section. The outline of this dissertation was presented at last.

## **CHAPTER 2 LITERATURE REVIEW**

This chapter began with literature reviews on traditional additive manufacturing. Some unique advantages and some limitations of traditional additive manufacturing such as stereolithography, selective laser sintering (SLS), electron beam melting (EBM), 3D printing, etc. would be discussed in this chapter. The second section will discuss about current printing technologies, which include inkjet printing, screen printing, Electrohydrodynamic (EHD) printing, etc. As one of the high –resolution printing methods, EHD printing will be discussed in the third part of this chapter, which included some backgrounds, developments, current research and some critical issues need to be solved.

### **2.1 OVERVIEW OF TRADITIONAL ADDITIVE MANUFACTURING**

Additive manufacturing has been developed for over 30 years, and it is one of the best technologies for producing small volume parts and rapid prototyping for many applications. The major advantage of this technology is the reduction of the time and cost [40]. Many different kinds of traditional additive manufacturing technologies have been developed since the first time of this idea came up. Based on the material types, traditional additive manufacturing can be divided into three categories: liquid-based process, solid-based process, and powder-based process [41].

#### **2.1.1 Liquid Based Additive Manufacturing**

Liquid-based additive manufacturing includes three different technologies: Fused Deposition Modeling (FDM), polyjet and stereolithography.

In the FDM process, usually, a thin filament of thermoplastic polymer feeds into a machine, where a temperature controlled extruder will semi-melt the material and force the material out from the extruder, and deposited the material onto the desired position on the substrate layer by layer [42,43]. The substrate will be lowered, or the printing nozzle will be lifted when a layer is finished and start to print next layer. The printing path and other parameters such as extruder moving speed, temperature setting, fill-gap, hatch pattern, strand-strand distance and layer thickness will be determined by the material used, required mechanical properties, part requirements and the application. Based on the shape of the final part, post-processing will be selected to perform accordingly. Figure 2.1 shows the scheme of FDM process [44]. The material used in this process are acrylonitrile butadiene styrene (ABS), polycarbonate (PC), PC-ABS blends, PC-ISO (medical grade PC), and polyphenylsulfone (PPSF) [43,45,46]. Another

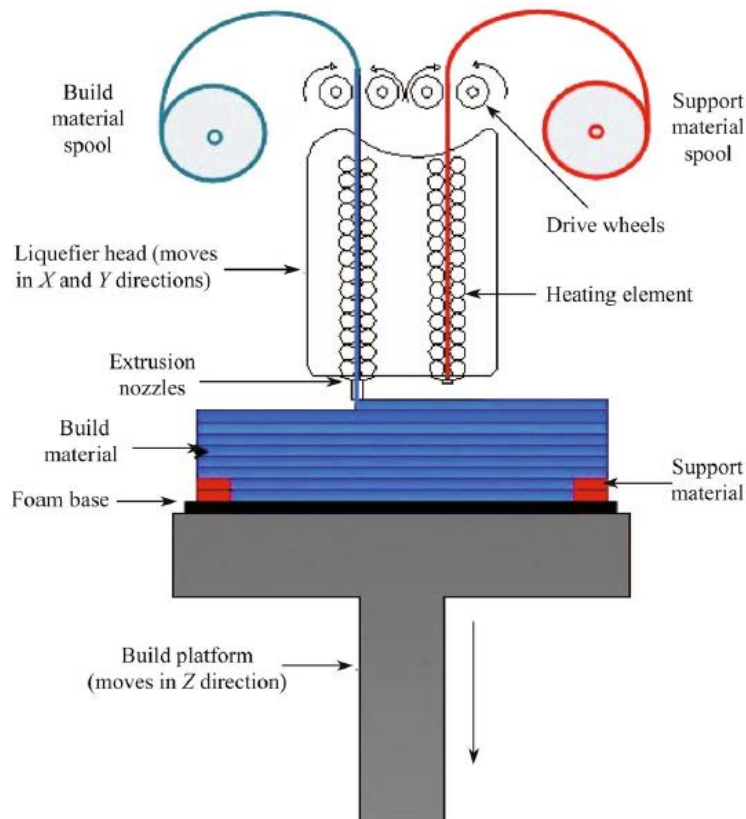


Figure 2.1 Principle of FDM process [44]

type of the materials, for example, the thermoset polymers are difficult to be used in this technology, because they need curing process to solidify and form a structure once they deposited on the substrate. The advantage of this technology is that no chemical post-processing required and cost-effective [47,48]. The main disadvantage of the FDM is that the typical resolution is not high enough to produce high precision parts for many applications, the common resolution of this process is greater than 100 micros, because the material is extruded from the nozzle, the produced jet size is larger than the nozzle size. When reducing the nozzle size, the required pressure is increasing rapidly, which usually difficult to obtain. Another reason is that it requires high accuracy flow delivery and temperature control system, and this will tremendously increase the system cost.

Polyjet is an additive manufacturing process using inkjet technology to printing parts. The printing nozzle will move on the X and Y axis, and the printed material will be cured by the UV light, which the light is acted as a catalyst after finished each layer [49]. Figure 2.2 gives a schematic view of polyjet printing process [50]. The best layer thickness of the technology is

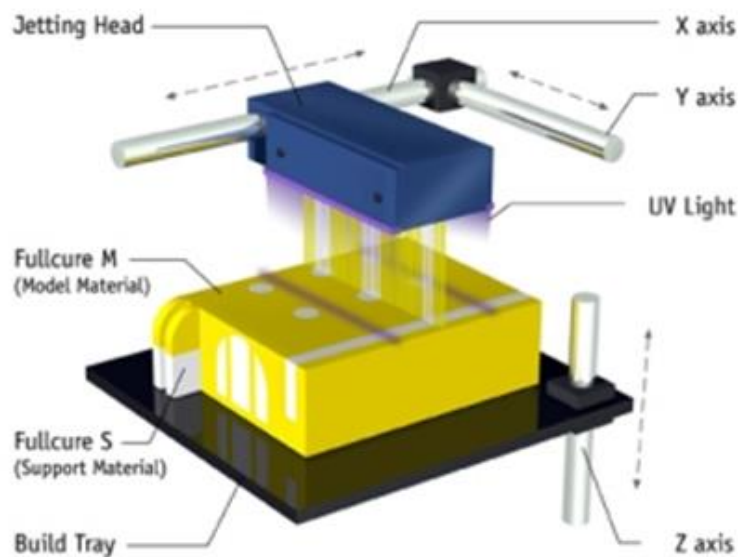


Figure 2.2 Schematic of polyjet 3D printing process [50]

about 20 microns, but the X-Y resolution is still around 200 microns, and the mechanical properties are weaker due to the properties of the materials [51,52].

For stereolithography technology [41,53], the liquid photosensitive polymer will be placed in the ink bed, and a UV light will cure the material cross-section by cross-section. A platform will be used during the printing if some overhanging structures are designed. Once the overhanging layer is finished, the platform will be lowered down. Figure 2.3 shows the schemes for two type of stereolithography system [54]. Currently, many different low-molecular weights, multi-functional monomers, highly cross-linked materials have been used in this technology [55,56], and many more advanced materials have also been developed in recent years, such as liquid crystalline polymers [57-59] which have high stiffness and thermal stability,

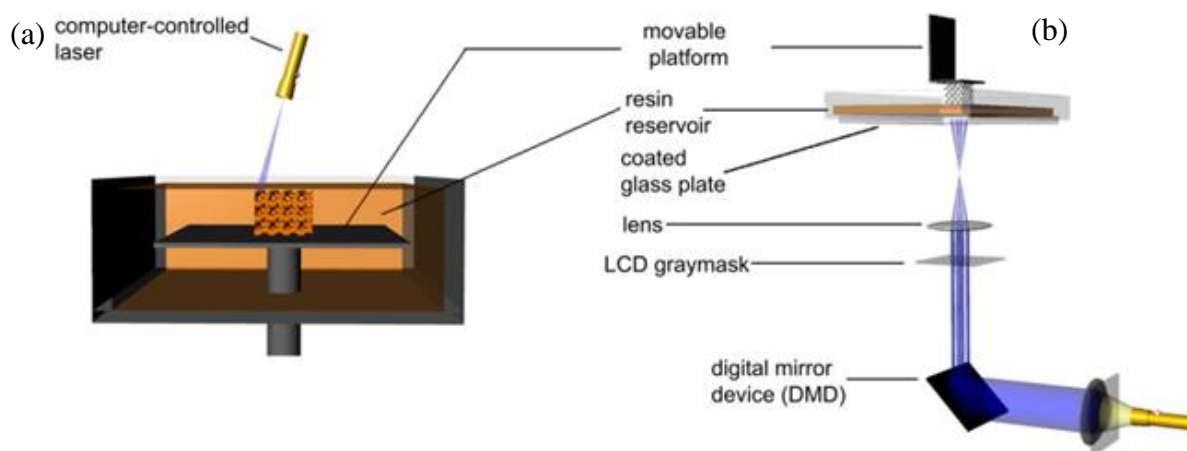


Figure 2.3 Schemes of two types of stereolithography systems. (a) Laser-based (b) digital light projection.[54]

hydroxyapatite [54,60,61], ceramics [62-65], and some metals [66,67]. For those advanced materials, a UV-curable prepolymer, photoinitiator, and other additives have to be mixed with those materials to form a suspension. Stereolithography can provide high-resolution, good surface finishing parts, but the two main limitations of this technology are the high requirement of the materials, and the difficulty of improvement of the printing resolution, which is limited by the UV-light size. Some of the other disadvantages of this method are that sometimes a final

piece will be overcured for the overhanging part and the scanned line shape due to the scanning process [68].

### 2.1.2 Solid Based Additive Manufacturing

Laminated object manufacturing (LOM) process is a solid based additive manufacturing process, which the laser beam will be used to cut the desired shape from the material with a sheet

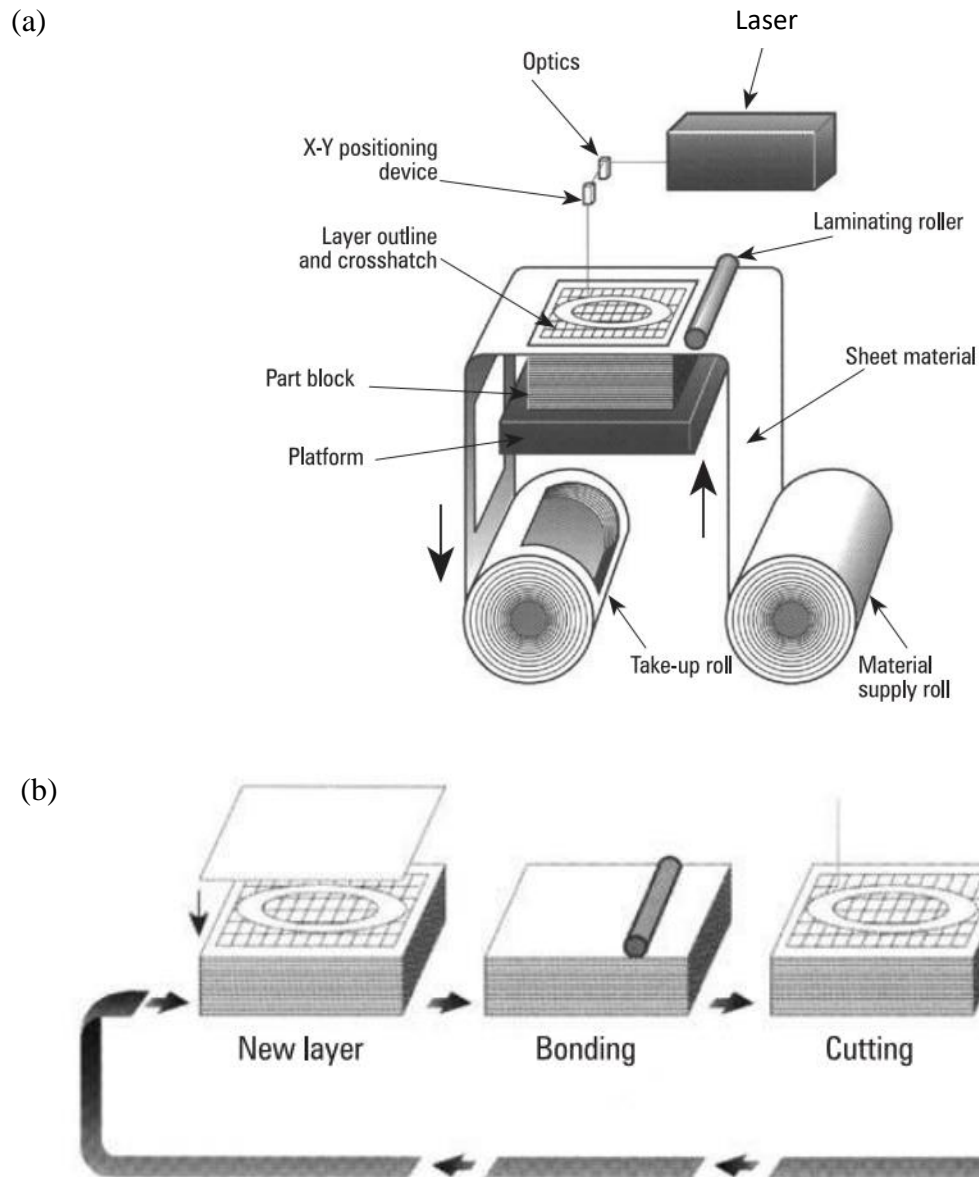


Figure 2.4 (a) Mechanism of the LOM machine. (b)LOM building process. [70]

shape. Each layer will be stick together by applying heat activated plastic [69]. Figure 2.4 has shown the components and the mechanism of the LOM machine and the schemes of the LOM processes [70]. This process is a low cost, no deformation or phase change process, and also it does not require any supporting structures. This technology has the potential to build large parts with internal cavities when compared with other additive manufacturing method. The drawback of this process is that it cannot produce high-resolution parts due to the laser beam size, and this process will generate a large amount of waste material. The produced part will have a large shrinkage in exchange for better strength after the thermal post-process [40].

### 2.1.3 Powder Based Additive Manufacturing

3D printing, Laser Engineered Net Shaping (LENS), Electron Beam Melting (EBM), Selective Laser Sintering (SLS), and Selective Laser Melting are the most common used powder-based additive manufacturing technology.

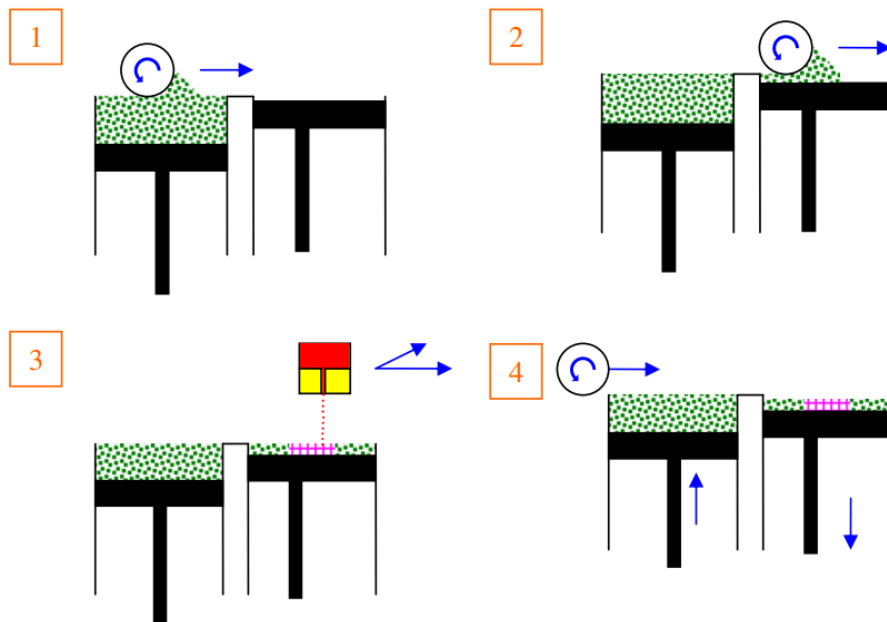


Figure 2.5 3D printing process: 1 and 2 place a layer of powder. 3 Binder is printing to this powder layer. 4 The whole will be repeated for every layer [73]

3D printing is an inkjet-based process, which the water-based liquid binder will be printed from the nozzle onto a starch-based powder bed during the printing process. The powders in the powder bed stick together when the liquid binder is deposited on the bed [71]. The structure will be built layer by layer by lowering the powder bed, and a fresh layer of powder is spread over the previous layers [72]. Once the final part is finished, post-processing is required to wash away the residue. Figure 2.5 shows the printing sequences of this printing process [73]. This printing technology has the capability to be used for a variety of materials such as metal, shape memory alloy (SMA), polymers, and ceramic [69,74-76]. This process does not require support material, because 3D printing uses powder as a substrate in each layer. However, the drawbacks of this process are inadequate surface quality, limited printed feature size, and porosity. Due to the almost identical printing process as inkjet, the jetted droplet size is directly determined by the nozzle size, and currently it is very difficult to improve the nozzle size to obtain a better droplet size for a higher resolution. Also, once the droplet is deposited on the powder bed, the wetting of the droplet will reduce the resolution.

Laser Engineered Net Shaping (LENS), which the schematic of system setup is shown in Figure 2.6 [77], is an additive manufacturing process that a part is fabricated by melting metallic powder, which the powder is injected into a specific location. A high-powered laser beam will be used to melt the powder. The material will get solidified when it cooled down to form the structure. The process occurs in a closed chamber with an argon atmosphere. This process can be used to fabricate a number of metallic alloys (for example stainless steel, nickel-based alloys, alumina, titanium-6 aluminium-4 vanadium, tooling steel and copper alloys) with improved mechanical and physical material properties [78-80]. This process can also be used to repair parts that are impossible or more expensive for other methods to do, but one of the significant

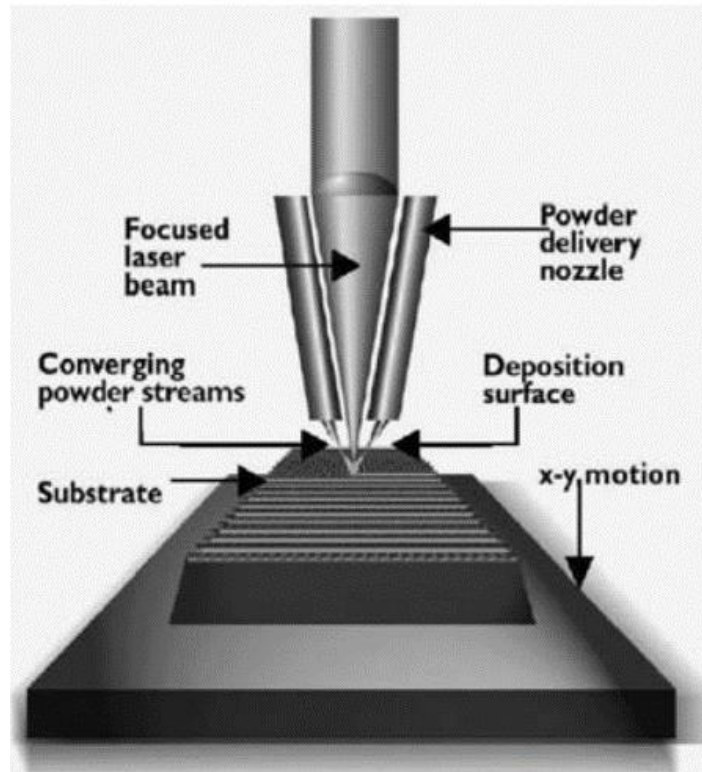


Figure 2.6 Schematic of LENS system setup [77]

problems of this process is that the residual stresses by uneven heating and cooling processes will be significant in high precision processes.

In EBM process, a heated tungsten filament emits electrons, which are collimated and accelerated to a very high kinetic energy level, and this electron laser beam will be used as a heating source to melt or fused the powder [81]. The electron beam will first scan over the powder layer with a predefined pattern and consolidates the desired areas into solid and dense metals. Then the laser beam will preheat powders to a sintered state with fast scanning on the powder bed. During the melting or fusing process, the laser beam will scan the powder bed at a very low speed for each layer. After finished the current layer, a new powder layer is laid on top, and the scanning process is repeated until final part are completed. Figure 2.7 shows a typical EBM system [82]. The process takes place in a high vacuum chamber and to avoid build-up of

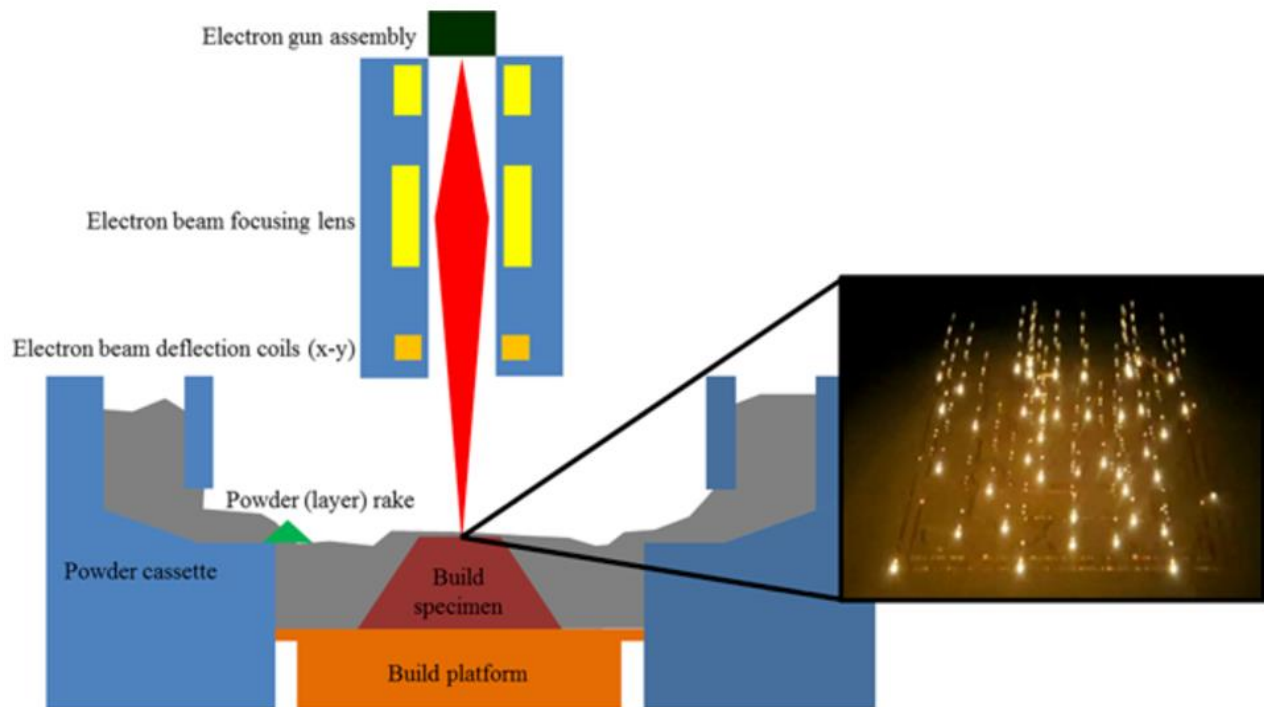


Figure 2.7 Schematic of EBM system setup [82]

electrical charges in powder, very low amount of helium gas is added to the chamber [83]. This process can be used for a variety of metal powders, such as aluminum alloys, niobium, nickel alloys, beryllium alloys, tool steel, etc [83-88]. Typically, this method is used for industries like aerospace that require high precision manufacturing and doesn't need large volume production. The advantages of using this process are that it can melt metal powder with a very high melting point which only a few additive manufacturing processes can achieve the same, and it also can produce very high precision parts. The drawbacks of this process are also very obvious. This process requires vacuum chamber, which will cost lots of money; and this is a laser-based process, which means it also requires large energy and the printing resolution will be limited by the laser spot size.

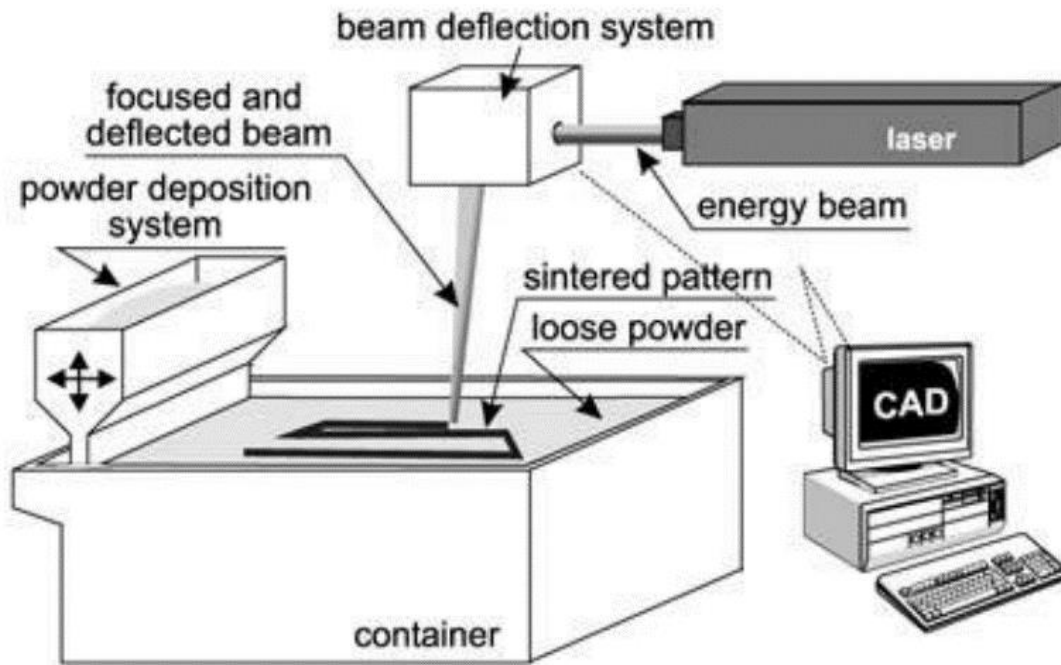


Figure 2.8 Schematic overview of SLS system [90].

SLS is also a laser-based powder additive manufacturing process, in which a high-temperature laser is used to sinter a layer of fine powder with the selected pattern. Once the layer is finished, a roller will spread fresh layers of powder on the top of the bed to create a new powder layer for the next laser sintering [89]. Figure 2.8 shows the consists of the SLS system [90]. When using fine powders to achieve high-resolution printing, a vacuum chamber has to be used in this process, because those fine powders will have higher reactivity against humidity and oxygen. Moreover, due to prevailing interparticle forces, layers of finer powders are very loose, and those fine powder will also easily get agglomerated [91,92]. Some unique methods [93] have to be performed to prevent the agglomeration, especially for the fresh powder layer. A variety of materials can be used in SLS, for example, plastics, metals ceramic and polymers [94,95]. The resolution of this process is usually larger than 500 micron for the commercial SLS system because the laser spot size is limited and also the limitation that comes from the powder size.

SLM process that shows in Figure 2.9 is very similar to SLS process [82], but the powder will be fully melted in the SLM process, which gives a chance to make much denser structure than the parts made by SLS [96]. Another advantage of SLM process than the SLS is that it can produce much more precision parts as high as 40 microns. However, this process requires much more energy and higher system cost than SLS.

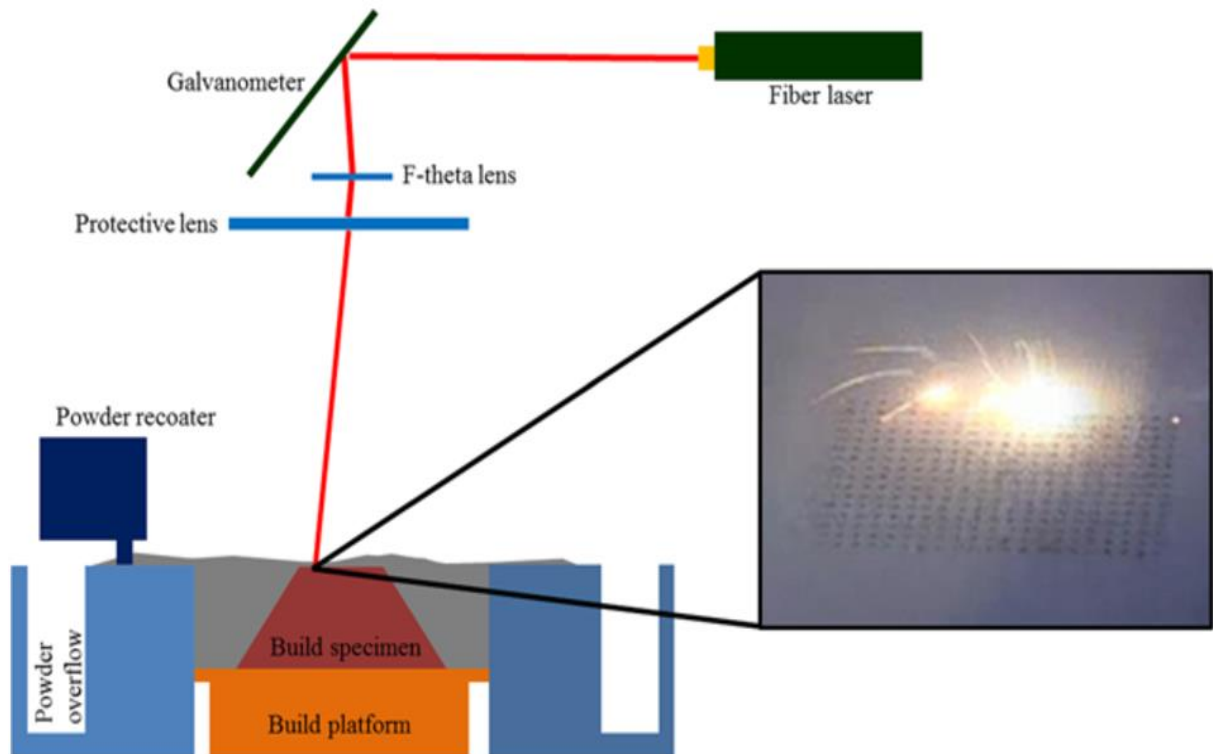


Figure 2.9 Schematic of SLM system setup [96]

## 2.2 OVERVIEW OF CURRENT PRINTING TECHNOLOGIES

Printing is a process that can reproduce text or images, and it is widely used in many areas such as manufacturing (food, prototyping, tooling), medical (pills, medical devices, bio-printing), industrial (apparel, automotive, aerospace), and sociocultural (art, communication, publication). This section will review some of the current printing technologies, which include

inkjet, EHD printing, pyroelectrodynamic printing, saw printing, screen printing, offset printing and gravure printing.

### 2.2.1 Inkjet Printing

There are two different printing mechanisms in inkjet printing, piezoelectric and thermal, and the scheme of inkjet printing is shown in Figure 2.10 [97]. Traditional inkjet printing use a binary operated electrostatic field to control the system to produce droplet [98], and usually, this kind of technology cannot provide high-resolution printing. However, some groups have demonstrated an inkjet technology that can produce a droplet with a diameter of 5 microns. They bonded a thin piezoelectric annular disc to a thin edge clamped circular plate to eject a droplet.

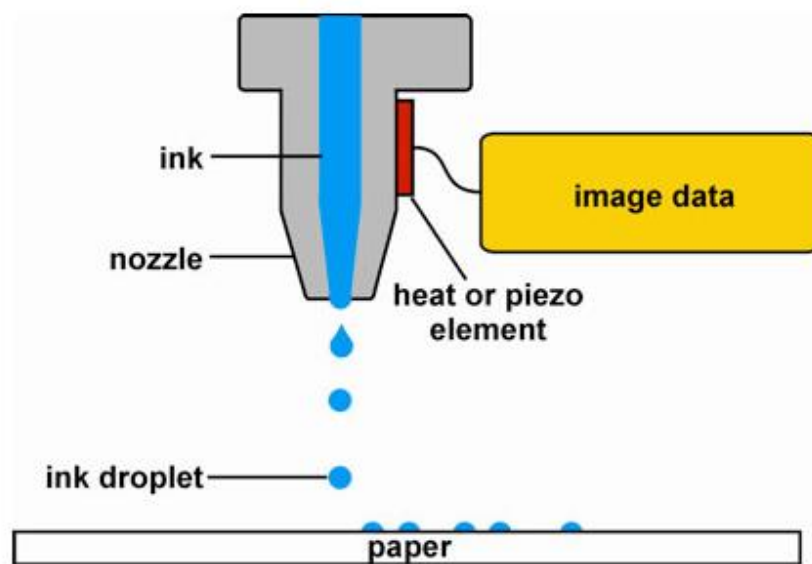


Figure 2.10 Schematic of drop on demand inkjet printing [97].

By controlling the different frequency, droplets with different size will be produced. This technology can apply to many fluids and fine solid particles [99-101]. Currently, most of the inkjet is applied to print 2D pattern, only a few groups have demonstrated the capability of printing 3D structure by using inkjet [102,103], but higher system setup or material is required to achieve the 3D fabrication.

### 2.2.2 EHD Printing

In the EHD printing, the ink will be subject to an electric field, and the mobile ions in the ink will generate an electrostatic force, which will drag ink out from the nozzle to produce a droplet or jet. By relying on the electrostatic force, it can overcome the nozzle limitation and produce high-resolution structures. The detail of the EHD printing will be introduced in section 2.3.

### 2.2.3 pyroelectrodynamic printing

Different from EHD printing, pyroelectrodynamic printing does not require a nozzle and high voltage. In this printing, when the ink is subject to a very large electric field, thin fluid jets will be induced to emit out from the reservoir [104]. Ferraro's group has demonstrated this technique to draw a droplet from a liquid reservoir [105,106], and Figure 2. 11 shows one of the system setups for this printing technology [106]. In their system, there are only two plates and a heat source, and no electrode or nozzle is required. The bottom plate is a glass, and a drop of ink will be placed on the glass. The second plate is lithium niobate (LN) crystal wafer, which will be used as the printing substrate. They used a hot tip or an infrared laser as their heating source. Once the heat source stimulates the LN substrate, a polarization will be induced and bring uncompensated charges on the LV substrate. Because of the existence of another plate (glass), the electrohydrodynamic phenomenon will be generated. When the electric field between the two plates exceeds a critical value, the small droplet will be produced and fly to the LN substrate. The smallest droplet size is about 300nm, and the required ink volume is reduced. Only non-conductivity materials can be used for this process.

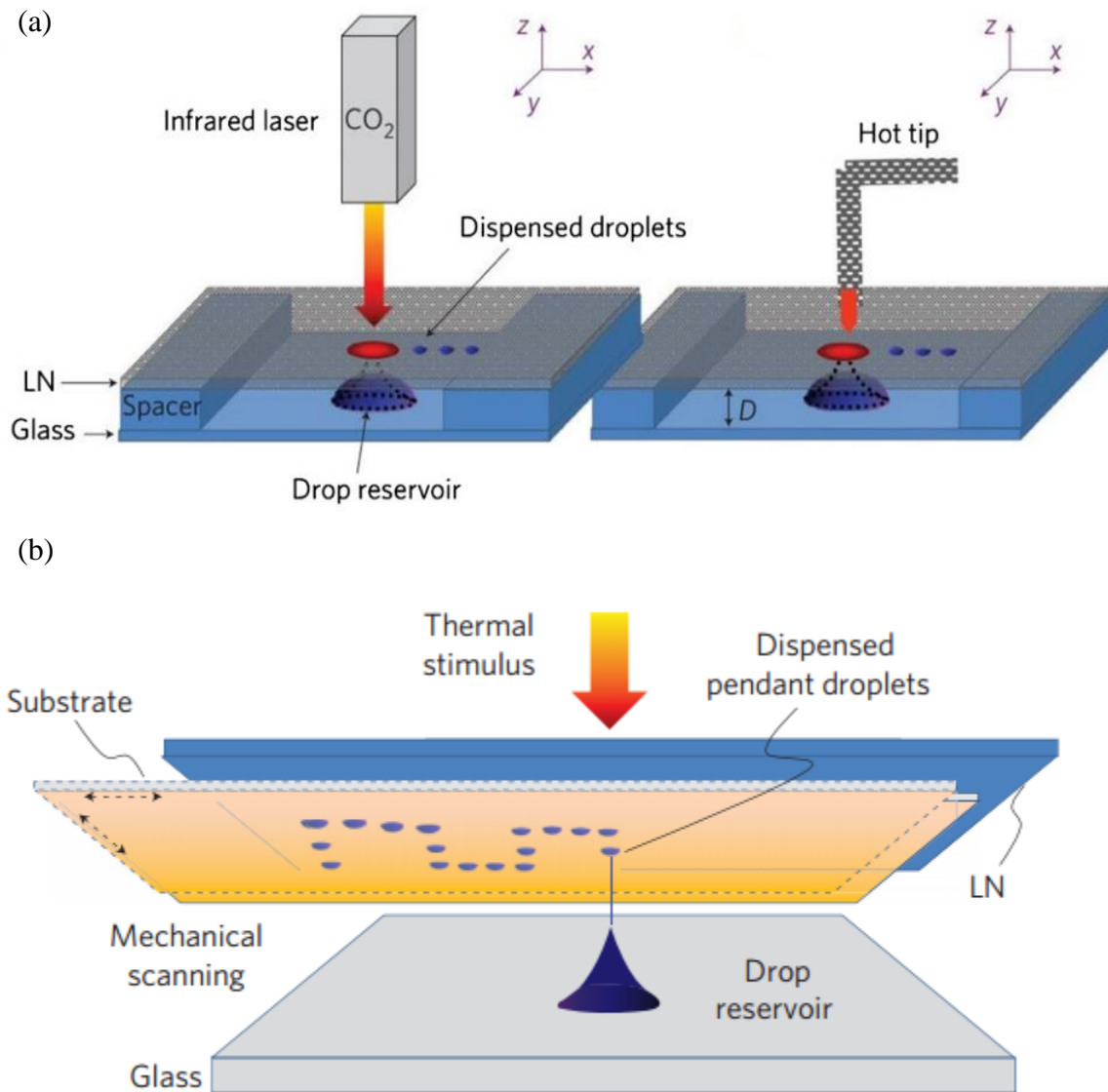


Figure 2.11 (a) Schematic of the pyroelectrodynamic printing system, including two plates and a heat source. (b) Droplet deposited onto substrate.[106]

#### 2.2.4 Saw Printing

The surface acoustic waves (SAW) printing [107] uses acoustic fields to drive the fluid's movement, which generate nanometer scale (1-10nm) amplitude waves. The nanoscale wave will spread on the surface of the substrate that is made of elastic material. The energy from those waves will be confined to a depth of 3-4 times of the wavelength into the substrate, and finally,

other energy will be concentrated to a spot, which has a size equal to the wavelength of the radiation using focusing transducers [107]. Once the energy gathers around the spot, it can generate a large surface acceleration ( $\sim 10^7 \text{ m/s}^2$ ) that will distort the fluid-air interface, and then a single elongated column of liquid is produced. Figure 2.12 shows the schematic of this method [108]. With this technology, the best resolution can be archived is about 100nm when using nanoparticles [108,109]. The drawbacks of this printing method are that it cannot print free-form geometries, for example, text or pictures, which means it does not have the capability to produce 3D structures.

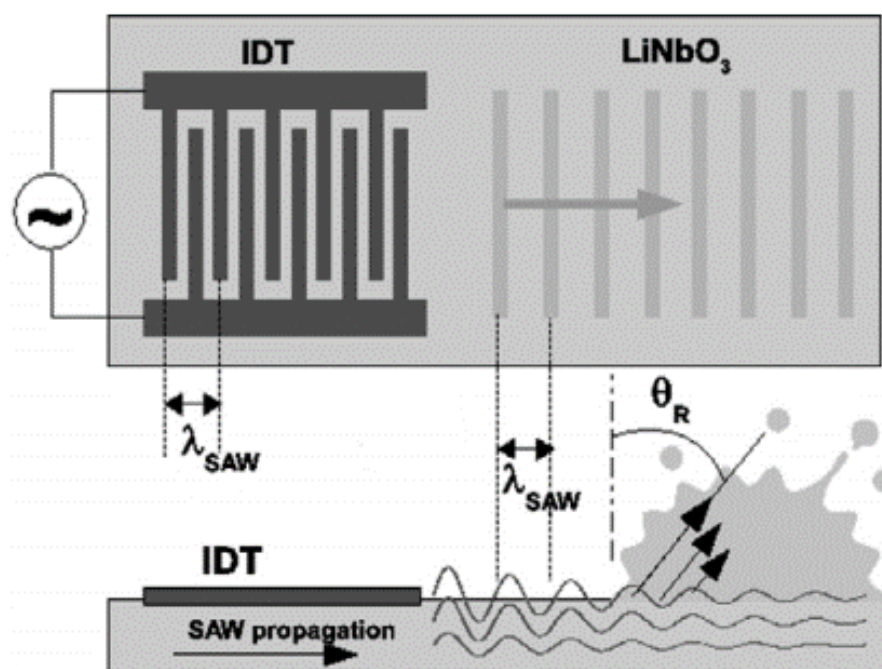


Figure 2.12 Schematic of nanoscale wave propagation and atomization [108].

### 2.2.5 Screen Printing

The screen printing is developed back to the early of the 20th century. It is a versatile printing approach, which allows for full 2-dimensional patterning of the printed layer [110,111].

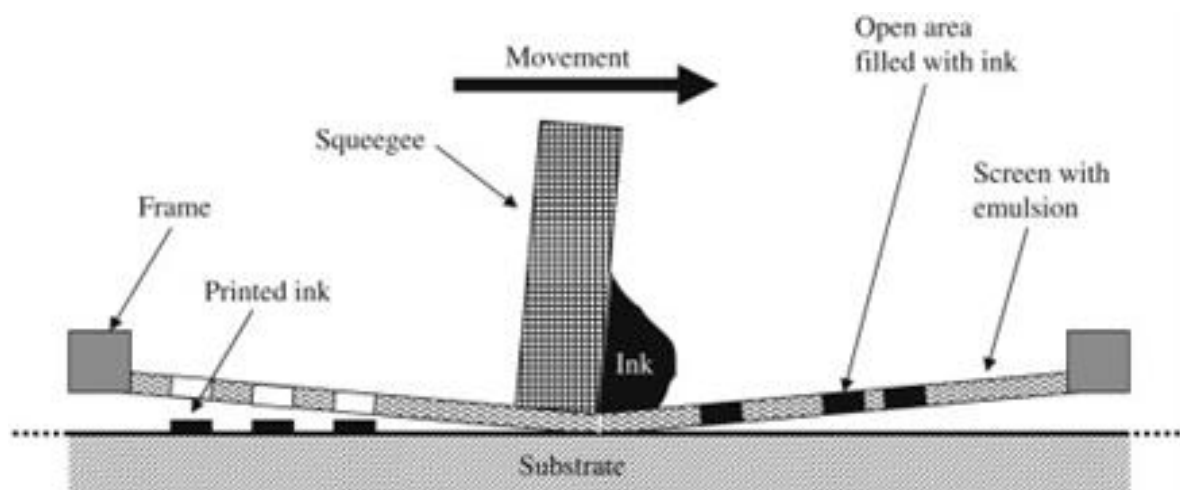


Figure 2.13 Schematic of the screen printing process [111].

The main distinction from all other printing techniques is a large wet film thickness and a requirement for relatively high viscosity and low volatility of the ink. In the screen printing process, a squeegee will be forced into a screen that will bring it into contact with the substrate. Then the squeegee will go linearly across the whole screen and force the ink to go through the blank areas that in the screen onto the substrate to produce the desired pattern. Figure 2.13 shows the screen printing process [111]. The main advantage of this method is the unique visual result it can create. The ink used is very durable and can either print larger or small size pattern. The disadvantage of this process is that it requires multi-steps process (such as place screen and align) to finish the final product. Also, this method cannot provide a high-resolution printing,

### 2.2.6 Offset Printing

In the offset printing shows in Figure 2.14 [111], the ink image or roller is transferred to an image roller or plate that only the pattern area will be printed ink. The printed ink pattern will offset to a roller and transfer to the web. Usually, most of the process is water chemistry based, and the printed area is made of hydrophobic material, which can be easily wetted by the ink.

Offset printing is a fast process with relatively low cost on system and material [112].

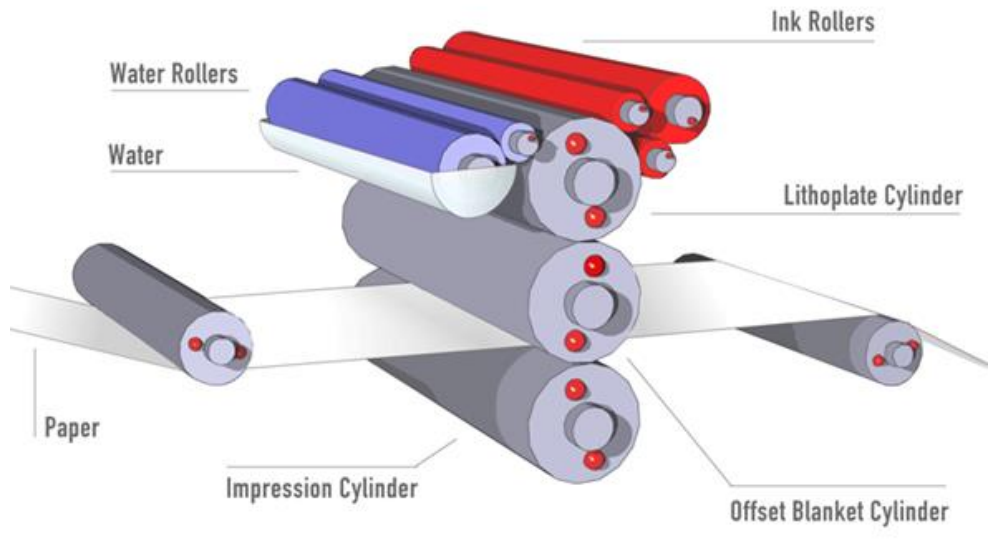


Figure 2.14 Schematic of the offset printing process [111].

### 2.2.7 Gravure Printing

Gravure printing directly transfers of inks through physical contact of the engraved structures to the substrate. This technology can provide a high-quality image with low system cost. The printing system consists of a giant roller electroplated with copper and engraved with

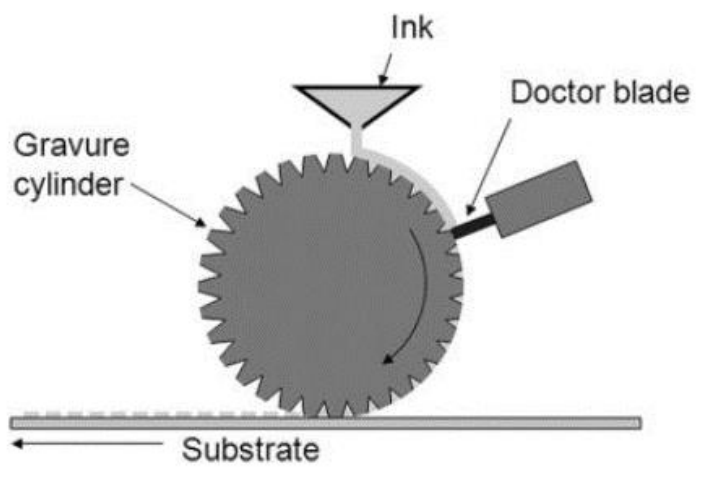


Figure 2.15 Schematic of the gravure printing process [112]

micro cells that show in Figure 2.15 [112]. The microcells are fabricated by using either electromechanical or laser [113]. The cylinder is coated with a thin layer of chrome to protect from wear and tear during the printing process. Once the cells are filled with ink, a doctor blade is used for removing extra ink from the rotating roller. Ink will be transferred through capillary action onto the substrate, and Surface properties of the substrate will also be modified to assist the transferring process.

### **2.3 OVERVIEW OF EHD PRINTING TECHNOLOGY**

EHD printing is a high-resolution printing technology, which has the ability to produce droplet or jet with a very high resolution that will overcome the nozzle size limitation. A Typical EHD printing system is displayed in Figure 2.16 [7]. Compare with the thermal or piezoelectric printing it will be easier to drag ink out from the nozzle using electrostatic force rather than applying high pressure. In the EHD printing, a voltage will be applied between the nozzle and ground electrode, which will generate an electric field around the nozzle. This electric field will accumulate the mobile ions in the ink to gather around the surface of the meniscus. With the Coulombic repulsion, a cone shape that also named as Taylor Cone will form at the apex of the nozzle [114]. When the electric field reaches a sufficient level, the electrostatic force will overcome the surface tension, and small dimension droplets or jet will be ejected from the Taylor cone. Currently, a variety of materials such as polymers, nanoparticles, biomaterials have been successfully used in EHD printing [6,115-117], and printing resolution can reach to a few microns or nanoscale. EHD printing process depends on many different parameters (e.g., applied voltage, printing speed, standoff distance, ink viscous, ink surface tension, etc.). Different printing parameters will bring different EHD printing modes [114,118-124], such as electrospinning and electrospray. Both of those two printing modes are unstable to be used for

3D printing because it is very difficult to control the printing process to printing desired pattern. For example, during the electrospinning, the printed fiber on the substrate is usually random because of whipping behavior (bending instability). This unstable printing behavior is caused by the evaporating of the solvent in the printing ink, which is essential to the electrospinning. For electrospray, the electrostatic force will break jet into numerous tiny droplets. Although this is an axis-symmetric process, the produced tiny droplets cannot be controlled, which result in an unstable EHD printing. Those instabilities are necessary for those two printing modes, but for high-resolution EHD 3D printing, they are no longer have the capability to meet the requirement obviously. To achieve a high-resolution EHD 3D printing, very stable printing modes have to be used, which are EHD drop-on-demand printing [104,125-128] and EHD direct jet plotting [129,130]. In the drop-on-demand printing, a meniscus will be formed under the electrostatic force, and droplet will detach from the apex of the meniscus once the electrostatic force that applied on the droplet is large enough to overcome the surface tension force. In the direct jet plotting, due to the high viscosity of the ink, no droplet will detach from the apex of the meniscus, the only fine filament will form at the apex of the meniscus and plot on the substrate when applying a proper voltage value to the system.

Drop-on-demand EHD printing with phase-change ink in pulsation mode can produce single tiny droplet each time, and this process has good controllability, which gives a potential to be used for high-resolution 3D structure printing. Many studies have already revealed the printing principle at macro-scale and lots of effects have already been put into the EHD printing [131], but the mechanism of the EHD printing process is still under development from the printing processes control perspective. It is very important to understand the mechanism of the printing process, and developing a model to simulate the printing processes will provide helpful

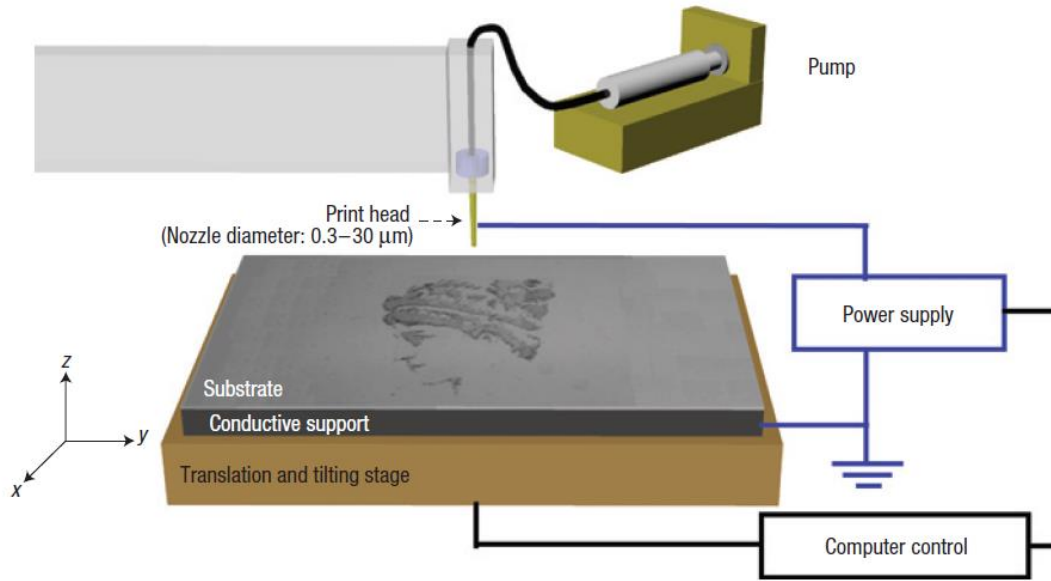


Figure 2.16 EHD printing system set-up [7].

information for the controlling of the printing process and predicting of printing behavior. However, it is still very challenging to predict the droplet formation [104,125], in-flight size, and droplet footprint on the substrate under the different printing conditions. Computational modeling based methods can provide promising result on the droplet formation in electrospray [132-136], but when dealing with the micro-scale droplet with high inflight velocity, this method is very difficult to be used for simulation or prediction for the EHD printing processes due to the highly complex coupled physics (electrostatic force, fluid dynamic, and singularity from the droplet pinch-off). Currently, there is no commercially available numerical solver that can successfully apply to the EHD drop-on-demand printing. Some of the groups [132-134] have developed their own solver to study some sub-set problems during the EHD printing processes. However, those solvers are very sophisticated and requiring high computational ability. Thus lots of computational load needs to be taken during the simulation. Few groups have created some highly simplified printing model to just provide the insight of this processes from engineering

perspective [133,137-139]. However, all of those models cannot simulate the overall printing process, so a model that can simulate the entire EHD printing processes that include droplet formation, droplet in-flight, and droplet settlement is remain.

EHD printing with phase-change ink has the capability to produce high-resolution 3D structures. Currently, most of the EHD printing systems have a planar ground electrode configuration, which the ground electrode is placed under the substrate. In this system setup, usually the applied voltage is a constant value during the printing, and the structures will be printed on the substrate. Once the ink is reached to the substrate, it will have some affections on the overall electric field distribution and intensity because the dielectric constant of the printing materials is different from that of the air. The effect of a single droplet or single layer is limited, and sometimes it can be neglected, but once the structure is building up, this influence cannot be ignored, and the electric field distribution and intensity will be changed extensively. Also, during the 3D printing, the height of the structure is limited by the distance between the printing nozzle and the substrate. For the traditional EHD printing system, the standoff distance is a constant value, which cannot allow the system to print higher structure. One of the methods to overcome this distance is to increase this standoff distance accordingly while printing. However, when lifting this z-direction, the electric field will be changed, and it is very challenging for process control to keep a constant electric field distribution and intensity due to the distortion effect of the electric field by the printed structure. Moreover, if higher structure needs to be printed, it will result in the large nozzle to substrate distance, and the required voltage will be very large, and this value is usually difficult to obtain.

Some electrode based electrode (e.g., pole, pin, and plate) printheads have already used in many areas. Borra's group use a plane electrode that connected with a positive voltage to help to

generate the electrosprays for pollution filtration [140]. Mahoney's research is using a plate ground electrode to generate ion source [141]. Some groups used pole integrated electrode to produce droplet [142,143]. The pole type nozzle will increase the efficiency of the jetting.

In order to solve this standoff problem in EHD printing, some of the groups have developed a method, which allows integrating the ground electrode into the printing head [133,144-147]. In Leo Tse's study, they used an electric field shaping printing, which is capable of controlling high-resolution EHD printing for different materials such as optical adhesive ink and silver nanoparticle. In their design, they use a double-layer ring electrode with an insulating layer between the two conductive layers. The upper layer connected to a voltage supply and the bottom layer is connected to the ground as the ground electrode. They have used this design to print 2D patterns onto non-conductive and uneven surface substrate [147]. Some of the groups, they have used a hole type electrode or gate with a stainless steel nozzle to print 2D patterns or tiny droplets. The hole type electrode is connected to the ground as a ground electrode, and the nozzle is connected with high voltage [142]. For the gated head design, both of the nozzle and the gated are connected with a high voltage, and the ground electrode is still located under the substrate. Thus the electric field vector distribution will be guided directly through the gate, which will improve the stability of printing processes [145]. Park's work is focused on the different design of the electrode such as a plane, hole, and pin type. They have simulated the electric field distribution on different designs, and also they have performed some experiments with different electrode design [144]. A cone shape lens around the printing nozzle was also used to concentrate the electric field near the nozzle for EHD printing [146]. With this forced lens, the electric field will be guided together to provide a more stable printing process. All of those researchers on the integrated electrode design reduce the effect of the standoff height and

improve the stability and controllability of the printing processes. However, those studies only focus on the characterization phase of the designed electrode for the printing process, and a few groups have performed some experiment on the 1D (droplet or lines) and 2D patterns. The investigation of the influence of this ring electrode to the 3D structure printing is still unraveled.

## **2.4 CHAPTER SUMMARY**

This chapter is about the overview of current additive manufacturing. Some traditional additive manufacturing technologies (EBM, SLS, 3D printing, FDM, etc.) have been discussed in the first section and included both of the advantage and disadvantage of those technologies. Some of the current printing technologies have discussed in the next section, which include printing system, printing materials, and some pros and cons of those printing technology. The last section has reviewed the current EHD printing progresses, which has the ability to fabricate high-resolution features. Some of the limitations of current EHD printing processes have been identified and need to be solved in the following research.

## **CHAPTER 3 HIGH-RESOLUTION EHD 3D PRINTING**

High-resolution fabrication is very important for modern manufacturing. It can provide good surface finishing, high precision, and good mechanical properties. Traditional 3D printing technologies are very challenging of producing high-resolution structures due to many limitations such as high energy required, high pressure required, laser or nozzle spot-size limitation, etc. In order to solve those problems, large amount money or energy has to be invested into the system, which makes those systems very expensive. Even with some expensive equipment, it is also very challenging to improve some limitations, like laser size and nozzle size, so it will be difficult to fabricate high-resolution structures with traditional printing technologies, which brings the high-resolution printing technologies to the front. In this chapter, a high-resolution printing technology (EHD printing) will be introduced, which has the capability to produce structures with a sub-10 $\mu\text{m}$  resolution. The printing processes will be characterized using Direct Current (DC) and Alternate Current (AC) Pulsed voltage. Optimal parameters will be obtained after characterization process, and those parameters will be used for 3D structure printing.

### **3.1 EHD 3D PRINTING SYSTEM AND MATERIAL**

#### **3.1.1 Printing Material**

In this study, a phase-change ink will be used for e-jet printing. Phase-change ink is one of the most commonly used material in additive manufacturing, especially in FDM. Most of the phase-change inks have a relatively low melting point so that it will be easily heated to semi-liquid or liquid phase. The other advantage of the phase-change is that it will get solidified quickly after deposited on the substrate while still keeping a good bonding strength between previous droplet or filament. This bonding strength provides the printed structure with good

mechanical strength. Phase-change materials also have a good corrosion resistance, and the cost is relatively low when compared with other printing materials. So this kind of material becomes very popular in the additive manufacturing. Commonly used phase changed ink in FDM include ABS, PLA, PC, etc. The paraffin wax belongs to phase-change inks, but it is seldom used in the additive manufacturing industry. The paraffin wax has a very low cost with the melting temperature about 55 °C, which is very easy to melt it into the liquid phase, and this makes it a good candidate material for our EHD 3D printing,

### 3.1.2 Printing System

The EHD 3D printing platform consisted of four sub-systems: a three-axis (XYZ) precision stage, a thermal control system, a high voltage supply, and a pneumatic dispersion system. The precision stage was installed on an anti-vibration table to reduce vibrational noise, and three linear stages were installed to the precision stage in XYZ directions with repeatability and accuracy of 100nm, and the linear stage was used to move the printing nozzle and substrate to the programmed locations. This precision stage had a working envelope of 100 x 100 x 50mm.

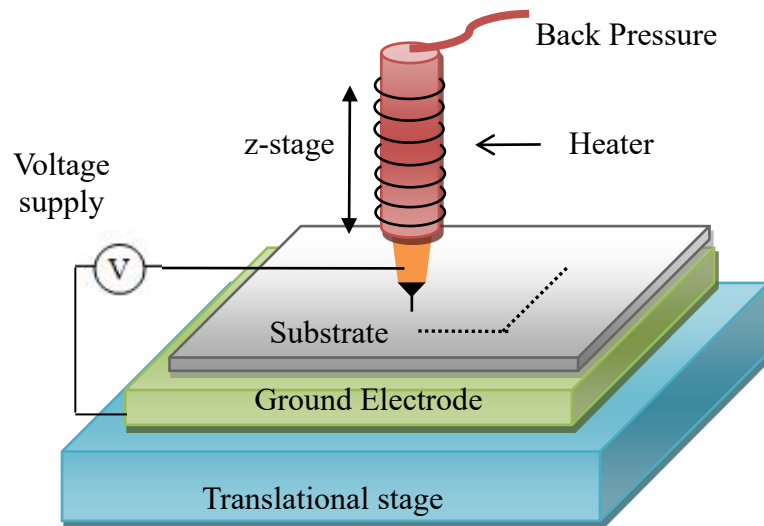


Figure 3.1 Schematic of the EHD printing set-up

The thermal control system consisted of three parts, a heating rope, which could provide a temperature up to 900 °F (482 °C) for the printing syringe; a thermocouple was used to measure the heating temperature of the syringe; a proportional – integral – derivative (PID) controller was used to control the power of the heating rope. The heating rope was wrapped around the syringe to provide heat for the ink inside the syringe, and the thermocouple was inserted to the top of the syringe that was closed to the nozzle to measure the syringe temperature and provide temperature feedback to the thermal controller (PID). The entire thermal control system had a resolution of 0.5 °C. A function generator (Agilent 3220A) was used to generate a required voltage signal, and the signal was amplified by a voltage amplifier. The voltage amplifier (Trek Model 610E) was purchased from Trek, Inc., which could provide a maximum voltage of 10KV. The pneumatic dispersion system was used to provide the pressure for the EHD printing process and keep the required ink flow rate. The back pressure was provided by an air pump and controlled by a precision regulator, which would provide a maximum pressure of 6 psi. A high resolution (0.5 $\mu$ m) camera was used to monitor the printing processes.

The substrate was microscope glass slide, which purchased from Fisher Scientific. The dimension of the slide was 75mm x 26mm x 1mm with a measured relative permittivity of 7.78, which measured by Stanford Research System LCR Meter SR715. Before using as a printing substrate, the slide was placed in three liquids (water, acetone, and ethanol in sequence) in an ultrasonic cleaner to clean the surface. Then the slide was placed on a hotplate for drying after ultrasonic cleaning, and those cleaned slides would cool down to ambient temperature before placed on the XY precision stage. The substrate was placed on the top of the aluminum coated silicon wafer, which could provide a ground electrode for the printing system. The thickness of

the aluminum film was 50nm, and it was coated to the silicon wafer by using thermal evaporation. The substrate and the ground electrode were located on the XY-stage.

In this research, the 5ml syringe was purchased from CADENCE SCIENCE with a metal Luer lock. The syringe temperature was set to 110 °C, which would perfect melt the wax and also reduce the surface tension and viscosity of the melting wax. The printing precision core that was purchased from Subrex was made of nickel silver and has an ID of 51  $\mu\text{m}$  and an orifice of 150  $\mu\text{m}$ . The precision core was connected with an interchangeable nozzle base (Figure 3.2 (a)) that was purchased from Integrated Dispersion Solution, Inc. to form the printing head by using super glue (Figure 3.2 (b)), and then the printing head was screwed into syringe that shows in Figure 3.2 (c). In this study, the distance between the substrate and printing head was set to 150  $\mu\text{m}$ .

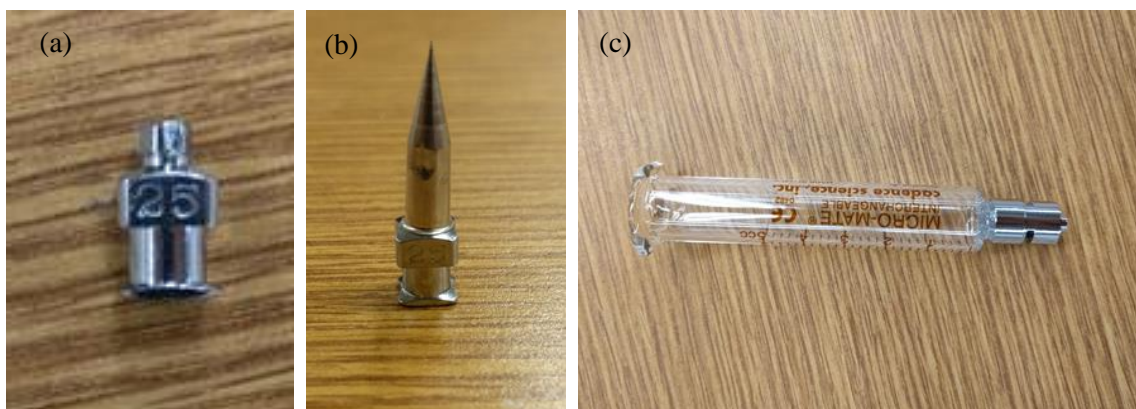


Figure 3.2 (a) interchangeable nozzle base (b) Nozzle glued with base (c) Syringe

### 3.1.3 Pattern Characterization

The filaments or micro-droplets will be printed on the substrate by using EHD printing method. The printed filaments or droplets was inspected under optical microscope, Atomic Force Microscopy (AFM) or Scanning Electron Microscope (SEM). The morphology of printed filaments or droplets and printed micro 3D structures were measured by using AFM or SEM.

### **3.2 EHD PRINTING PROCESS AND CHARACTERIZATION UNDER CONTINUOUS DC VOLTAGE**

In EHD-jet printing, a large voltage was applied between substrate and printing head, which would gather mobile ions in the printing ink near the surface of the printing tip to form chargers. The charges would bring an electrostatic force to deform the meniscus at the tip of the nozzle to form a conical shape (Taylor cone). When increased the voltage, the electrostatic force will increase, which dragged more ink out from the nozzle to form a larger meniscus. When increased voltage to a certain intensity, the electric field was large enough to provide an electrostatic force at the apex of the cone that exceeded the surface tension force at the Taylor cone, a jet or a droplet would be injected from the meniscus onto the grounded substrate. Mostly, the plotting results will be affected by the fluid properties of the ink, printing process conditions (i.e., ink temperature, standoff distance), and applied printing voltage. In this study, only one material will be used during the characterization process, and the ink temperature and standoff distance will keep a constant value of 110 °C and 150µm. Small standoff distance makes it hard for us to observe the process and larger standoff will bring more disturbance during the printing process.

Generally, three different printing modes, pulsation mode, stable jet, and the unstable jet could be observed during the increasing of the printing voltage. By working with wax-based supporting material and building material, stable pulsation printing mode can provide drop-on-demand printing capability, which has a potential to be applied in the high-resolution micro-3D printing and additive manufacturing. In the stable mode, a fine droplet will be injected on demand and deposited onto the substrate to form 3D structures layer by layer. For the unstable jet mode, multi-jet or satellite droplet can be found during the printing.

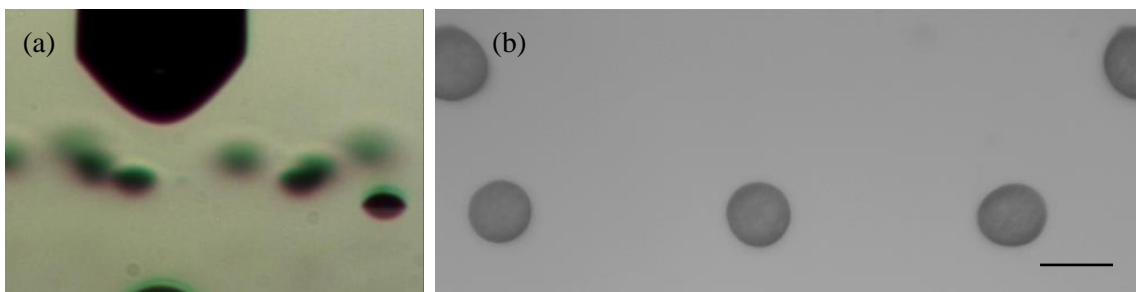


Figure 3.3 (a) Cone-shape at initial start voltage under pulsation mode (b) Printed larger size droplet at initial start voltage. (Scale bar 50 $\mu$ m)

In this study, a positive voltage will be applied to the system, and only the value of this voltage will be changed during the characterization process. For melted wax in EHD printing, at the voltage of zero, no meniscus can be observed at the apex of the nozzle. When we gradually increased the printing voltage, a meniscus and Taylor cone was gradually forming at the tip of the nozzle, and due to the wetting of the printing material (wax), the diameter of the cone shape was equal to the orifice of the nozzle and only a small cone shape can be observed. When continuing increasing the voltage to a threshold value, the cone shape will increase (Figure 3.3 (a)), and when the applied voltage was larger enough (around 650v in this system setup) to provide enough electrostatic force to overcome the surface tension, a micro droplet was ejected from the apex of the Taylor cone and printed onto the glass substrate. At this initial stage, the printed droplet that shows in Figure 3.3 (b) has a large diameter and the printing frequency was very low that can be explained as the following, at this initial voltage value, it required more mobile ions to provide enough electrostatic force to separate ink from Taylor-cone. More mobile ions mean it has to bring more volume of ink and longer charge migration waiting time for the mobile ions to gather around at the apex of the nozzle. When continuing increasing voltage, the cone shape will be further increased (Figure 3.4 (a)), because the larger electrostatic force will take out more ink from the nozzle. The droplet ejecting speed will increase, and the droplet size

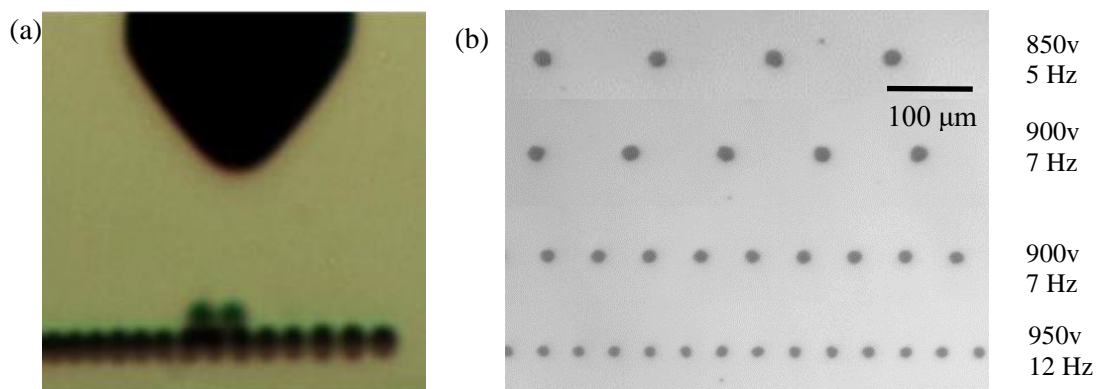


Figure 3.4 (a) Cone shape at voltage of 850V. (b) Droplet size and printing frequency at different positive voltages (Droplet size from top to bottom: 17μm, 14μm, 11 μm, 8 μm)

will decrease. Figure 3.4 (b) has shown the droplet footprint size and printing frequency under different voltages from 850v to 1000v. It is obvious that increasing the voltage will lead to increase the printing frequency (from 5 Hz to 19Hz) but decrease the size of the printed droplets (from 17 μm to 8 μm), this can be easily explained by the mechanism of EHD printing. When increased the voltage, the surface charge density of the printing ink at Taylor cone would also be increased, so smaller volume of ink (smaller size of the droplet) will be needed to obtain large enough electrostatic force to overcome surface tension force and eject from the apex of the Taylor cone. Increasing the voltage will also increase the charge migration rate, which give a result of faster charge accumulation time at the apex of the cone to initiate ejection that will increase the printing frequency. Continuing increasing the voltage to a certain threshold, which 1500V in this study, satellite droplets or multi-jet which show in Figure 3.5 will be printed. Satellite droplets are very tiny droplets that occur when the voltage is too high, because high voltage can provide high electrostatic force, which had the ability to shred droplet into several small droplets (satellite droplets), so the satellite droplet indicates unstable printing condition. High voltage will also split the meniscus to form multi emitting sites around the nozzle so that

multi-jet will be observed during the printing. Multi-jet mode usually has a higher flow rate but smaller droplet dimension when compared with pulsated mode printing.

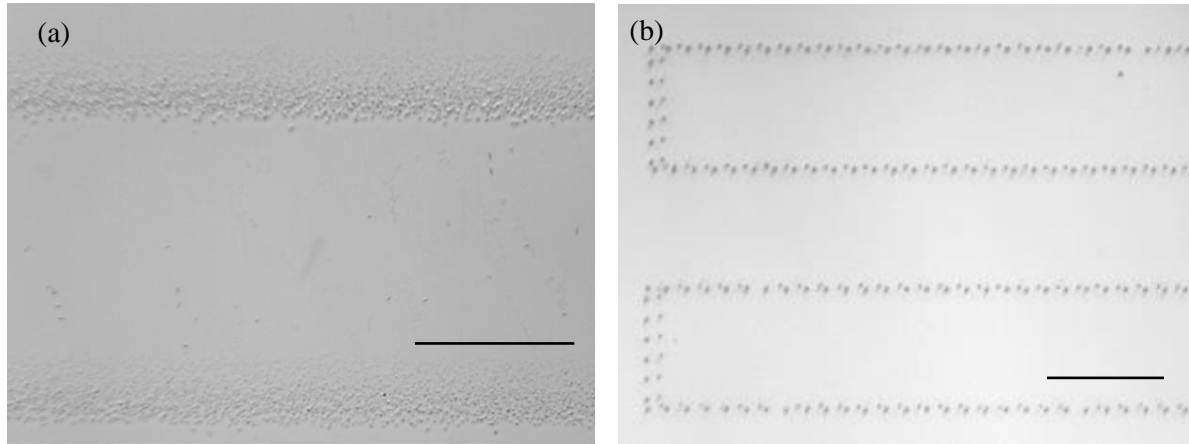


Figure 3.5(a) Printed satellite droplets (b) Multi-jet in EHD printing. Scale bar: 100  $\mu\text{m}$ .

### 3.3 EHD PRINTING PROCESS UNDER CONTROLLED VOLTAGE

#### 3.3.1 EHD printing process under DC pulsed voltage

The voltage used in the experiments above is the DC voltage. The only controlling factor in the voltage is the value. From the last results, the droplet size and droplet jetting speed is directly determined by the applied voltage. The small voltage will result in a large droplet and slow jetting speed, and larger voltage will result in a small droplet and fast jetting speed. So, it is very difficult to obtain small droplet with a controllable jetting speeding when only apply continuous DC voltage to the system. In the E-jet printing, a controlled printing frequency can bring many advantages, especially in 3D printing. During the 3D printing, a controllable printing speed can reduce many disturbances and deposit droplet more precisely. The DC pulsed voltage shows in Figure 3.6 will be controlled by three factors, amplitude of the voltage, duty cycle and

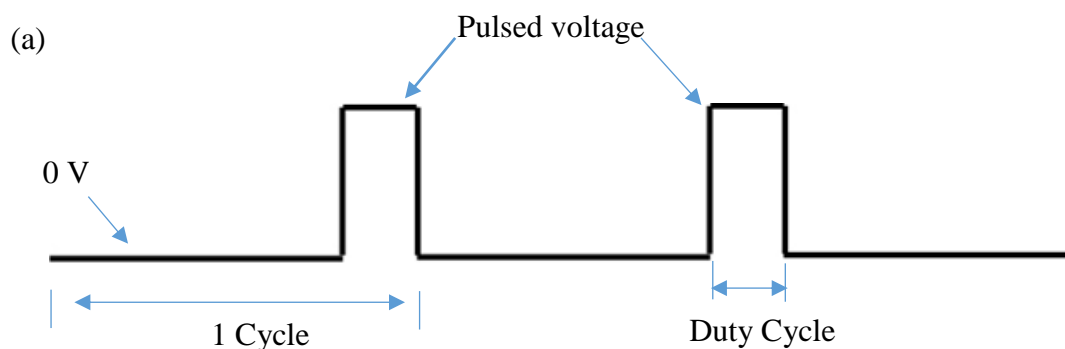


Figure 3.6 The regular DC pulsed voltage signal

pulse frequency. The frequency will be used to control the droplet printing frequency, and voltage and duty cycle will match with each other to produce a droplet in a single cycle. To characterize the affection of those three factors to the printing process, we have to characterize one factor each time, and the printing frequency and droplet size will be used to verify the printing process. The designed DC pulsed voltage wave pattern was created in the computer with Waveform Builder software. This signal will be sent to function generator and stored in the function generator. Once the function generator is on, it will send the pulsed voltage signal to the voltage amplifier, which will amplify the voltage to the required level, before sent to the printing system.

To study the effect of the voltage on the printing, the pulse frequency, and duty cycle will be fixed as 20Hz and 20%. Based on the characterization process in the previous section, when applying a continuous DC voltage of 1000V, the printed frequency is close to 20Hz. So choosing 20Hz will provide a relatively large voltage range that will allow us to perform the test because the start voltage is 650V and the highest voltage level is 1500V. Large duty cycle will easily generator two or more droplets in a cycle with a relatively low voltage, and a small duty cycle will be difficult for the system to generate single droplet in a cycle with a high voltage. So 20% duty cycle was chosen to ensure the easy observation and process control. The standoff distance

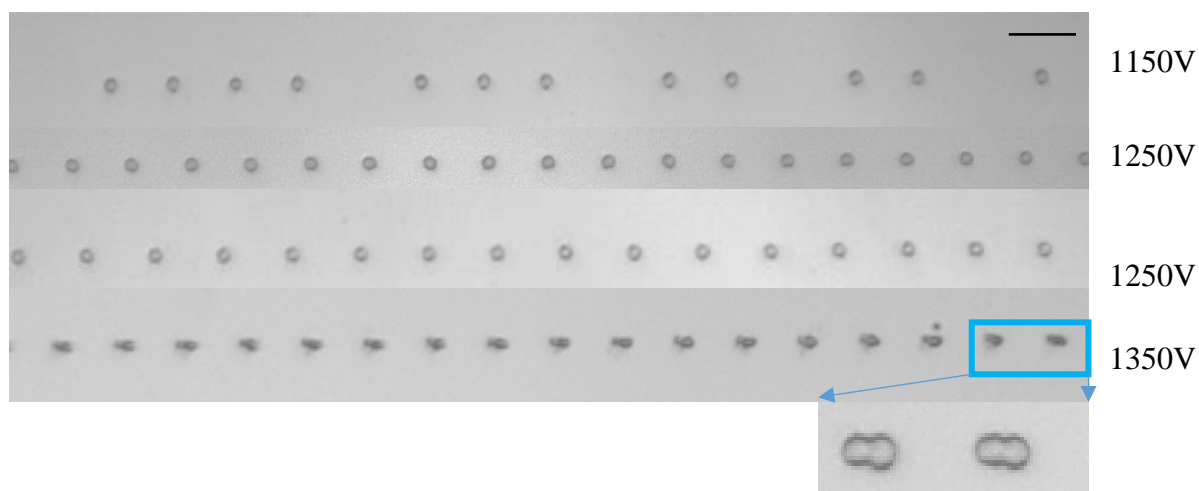


Figure 3.7 The result of printed droplet under pulsed DC voltage with different voltage amplitudes; (scale bar: 50  $\mu\text{m}$ )

and stage moving speed for all printing will still keep as a constant of 150  $\mu\text{m}$  and 1 mm/s. The result of the printed droplet is shown in Figure 3.7. Obviously, when the voltage is less than 1000V, no droplet with 20Hz frequency can be found. When the applied voltage is low (1150V in the Figure 3.7), there are some missing droplets on the substrate, which means during some cycles, no droplet is generated. At this time, the voltage is little insufficient, the electrostatic force generated during the pulse section cannot drag droplet out every time. When increasing the voltage to 1250V, the printed droplets have a printing frequency of 20Hz, which is match with the setting pulsed frequency. This time, the voltage reached a working level that can produce droplets with the desired frequency. Continuing increasing the voltage to a certain range, the printed droplet will keep a constant printing frequency of 20Hz. The increasing voltage will not lead to high printing frequency that is because the 20% duty cycle pulsed voltage does not have enough time to produce more than one droplet, which limited the number of generation of the droplet, which means the droplet printing frequency is under controlled. There is no obviously changing in droplet size, however, once the voltage exceeds a critical value (1450V in this

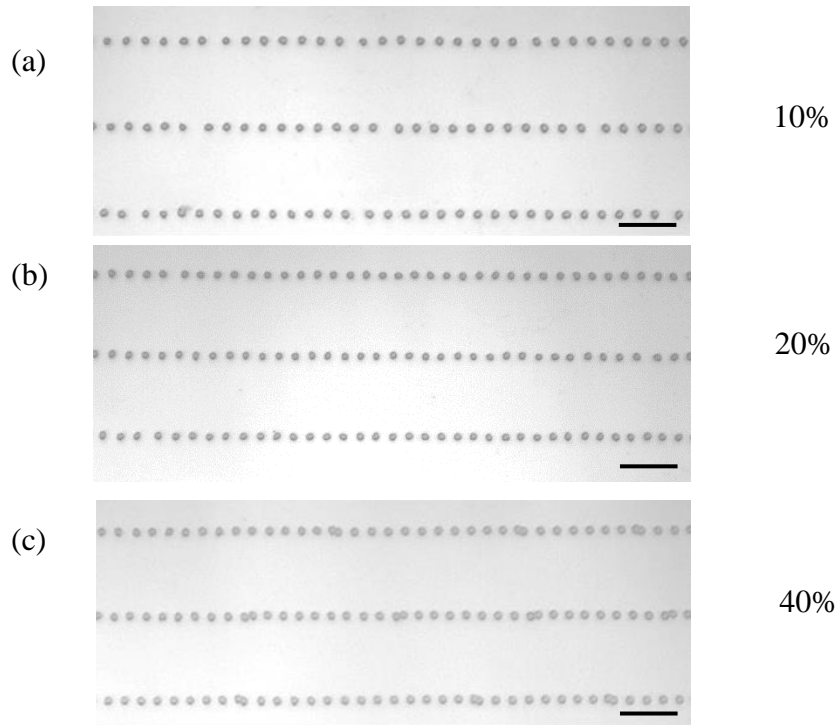


Figure 3.8. The result of printed droplet under pulsed DC voltage with different duty cycles (scale bar: 50  $\mu\text{m}$ )

study), two combined droplets is found on the substrate. This may occur due to the reason that when applying a high voltage, the charging time is short and the electrostatic force is large enough to drag multiple droplets during a 20% duty cycle time. So the set pulse frequency cannot control the droplet printing anymore, which indicated an infeasible printing condition.

To evaluate the effect of the duty cycle on the printing process, a constant voltage of 1200V and frequency of 20Hz will be used during the test. When the duty cycle is too small, no droplet will be printed on the substrate because of the insufficient charges and electrostatic force. When start to increase the duty cycle, droplets will be found on the substrate, but still, some of the droplets are missing (Figure 3.8 (a)) if the duty cycle is not large enough that may due to the insufficient charging time. As continuing increasing the duty cycle, the printing frequency (Figure 3.8 (b)) will match with the pulse frequency, which gives a stable and feasible printing

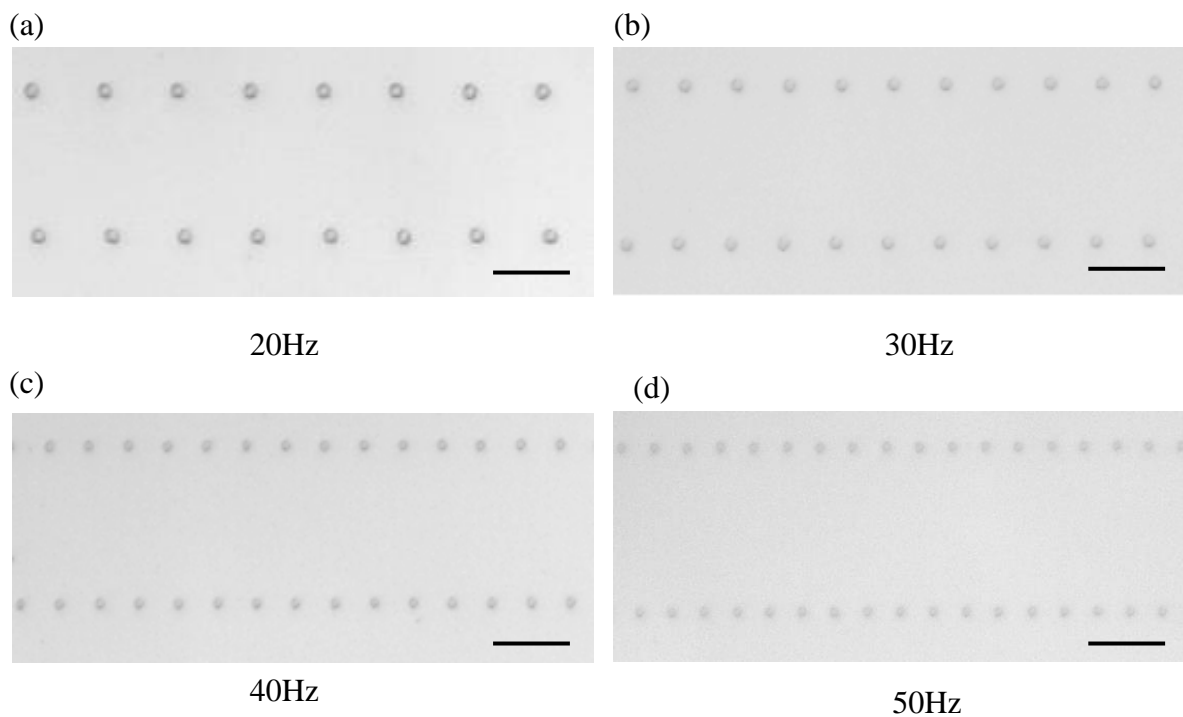


Figure 3.9 The result of printed droplet under pulsed DC voltage with different pulse frequencies. (Scale bar: 25  $\mu\text{m}$ )

condition for EHD printing. When the duty cycle is increased to a higher level, for example, 40%, multi-droplets are printed within a cycle, which indicated the unstable printing. Based on those results, for a fixed voltage and pulse frequency, a duty cycle range exists that allow the system to print droplet with expected frequency. Once the duty cycle is above or below this range, printing process will become unstable.

To test the effect of the frequency on printing behavior, printing voltage of 1400V and duty cycle of 10% will be kept as constant in this test. Using a small duty cycle will ensure that only one droplet is generated in a cycle, which will make the printing process easy to control. Because of the small duty cycle, a relatively large voltage has to be selected. If the voltage is too small, no droplet will be produced when the set pulse frequency reaches a relatively high level, because the charging time isn't enough. The printed result is shown in the Figure 3.9, and based

on the observation, the printed frequency is precisely controlled by the pulse frequency. However, there is a changing in the printed droplet size. When a low pulse frequency is used, the printed droplet has a larger size than the droplet that printed under high pulse frequency. This can be explained that a low pulse frequency will provide a large pulse duration time, which allows ink to charge more ions and obtain larger electrostatic force, and a large droplet will eject from the nozzle. When the pulse frequency is high, the pulse duration time is short, which will lead to a small size droplet.

Another test has been conducted to find the combination of voltage and duty cycle for a fixed printing frequency. In the experiment, the pulse frequency was set to 50Hz, and when gradually increase the voltage, the duty cycle will be adjusted accordingly in order to get printing frequency of 50Hz. When the voltage is reaching to initial starting voltage, a droplet will be produced, but the printing frequency is much less than 50Hz obviously. Continuing increasing the voltage, the printing frequency will increase accordingly but still less than 50Hz. When the voltage is set to 1000v with a duty cycle of 100%, the printing frequency reaches to 50Hz. At this time, 1100v is the minimum required voltage to produce a printing frequency of 50Hz.

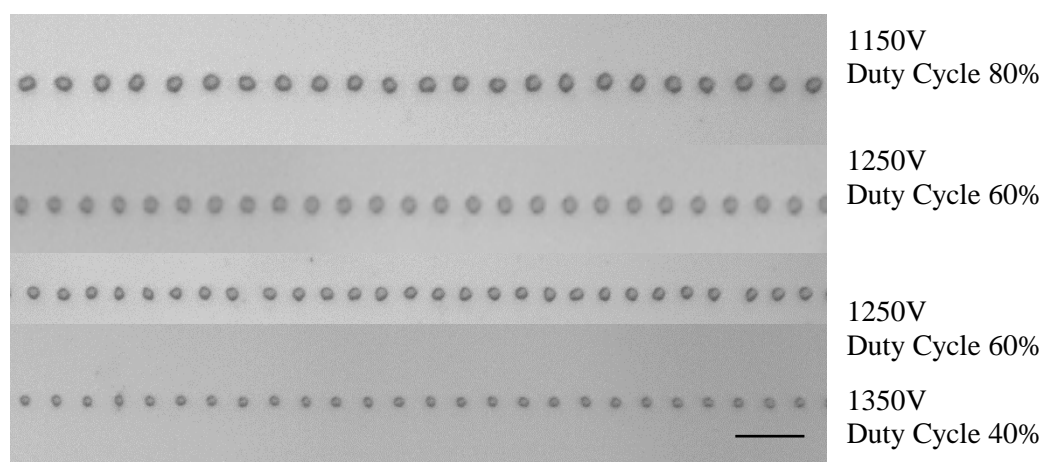


Figure 3.10 Different combinations of voltage and duty cycle for a printing frequency of 50Hz. (scale bar: 50  $\mu\text{m}$ )

When future increases the voltage, the printing frequency will be higher than 50Hz, if the duty cycle is set to 100%. So adjusting of duty cycle process has to be performed to keep the 50Hz. Figure 3.10 shows the different voltage and duty cycle combinations that can produce 50Hz printing frequency. From results above, increasing the voltage will reduce the required duty cycle length. However, when the voltage exceeds 1500V as mentioned in the last section, the change of getting satellites or multi-jet will raise. To reduce the chance of getting unstable jetting mode, a modified voltage signal is developed.

In the pulse voltage above, times will be required for the mobile ion gather around the apex of the nozzle, thus it will need higher voltage to induce this process. In this modified voltage signal, a constant voltage 600V will be applied along the whole printing process. This purpose of applying this voltage is to assist the pulsed voltage to produce the droplet. In the pulse voltage above, times will be required for the mobile ions gather around the apex of the nozzle,

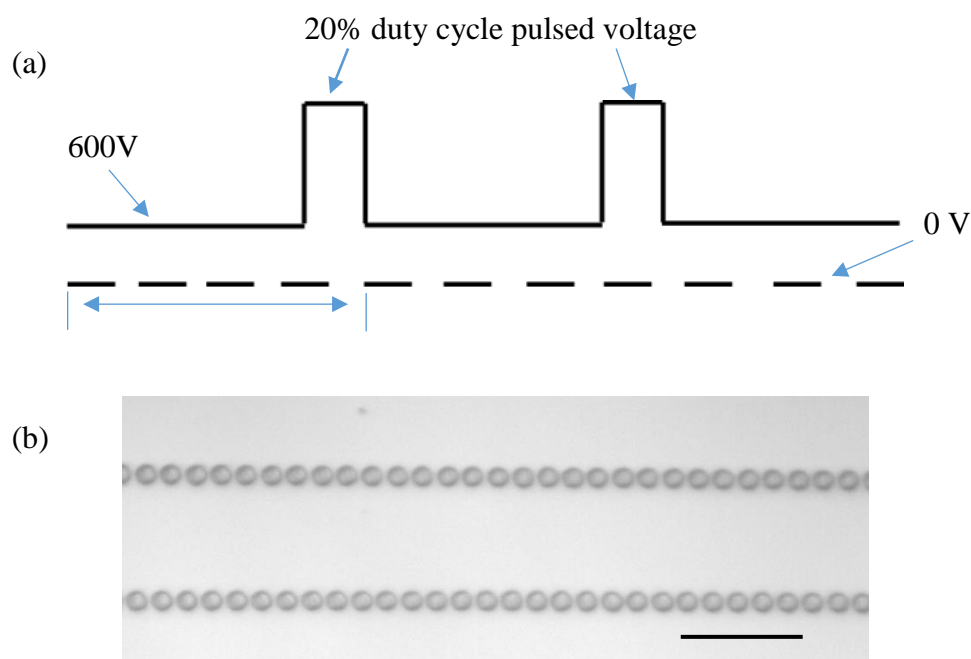


Figure 3.11 (a) The modified DC pulsed voltage signal (b) 50Hz of printing frequency under voltage of 1250V (scale bar: 50  $\mu\text{m}$ )

thus it will need higher voltage to induce this process. This 600V will provide an electrostatic force to drag ink out from the nozzle to form a cone shape and also let mobile ion gather at the apex of the cone shape; but it also will prevent to produce a droplet at the apex of the nozzle, because the initial start voltage is about 650V. Once a pulse voltage is applied to the system, the system will easily produce a droplet, and the required pulse voltage is also reduced. With this assistant DC voltage, the duty cycle of this pulse voltage can be reduced. In this experiment, the duty cycle is set to 20% that is less than the minimum duty cycle used in Figure 3.6 to verify the function of the assist DC voltage. The final modified voltage signal is shown in Figure 3.11 (a) and Figure 3.11 (b) shows the printed droplet with a printing frequency of 50Hz with a pulse voltage of 1250V and duty cycle of 20%. The printed droplet still has almost the same size as the previous droplet, and this result clearly shows that with adding an assist voltage, the required duty cycle and pulsed voltage is reduced, which can eliminate the possibility of producing unstable jetting process.

### 3.3.2 EHD printing process under AC voltage

In the EHD printing with DC voltage, once one droplet was printed on the insulating substrate such as microscope slide, the charges on this droplet will remain on the substrate for a while due to the slow charge decay rate especially for conductivity ink. At this time, this remained charges will change the electric field distribution and interrupts the printing process and the following droplets. This residue charges will make the EHD printing process control more difficult especially for the high-resolution printing. Here, a square AC voltage will be applied to the system, which has the ability to improve the system control and also control the droplet printing frequency while producing small size droplet. When applied the AC square voltage, the charge polarity of the printed droplet will be neutralized on the substrate, so the

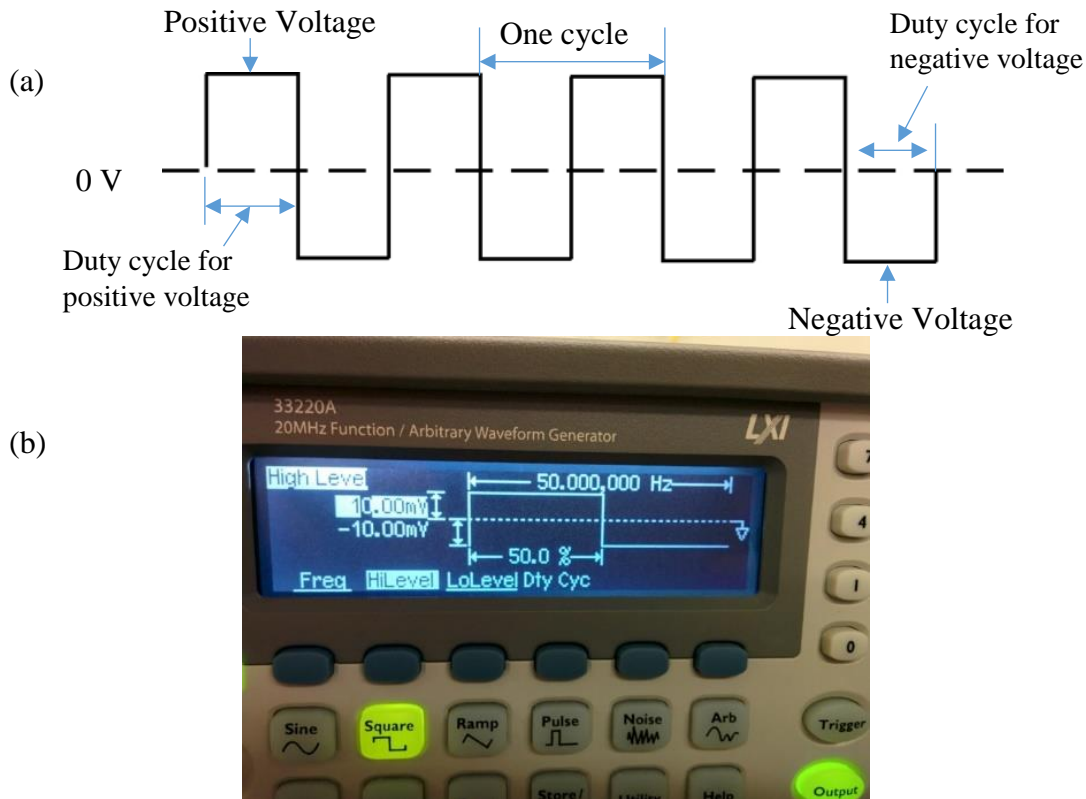


Figure 3.12 (a) Square AC voltage signal pattern (b) generated square AC voltage in function generator.

effect of the charge to the printing system will be minimized. With the controlled frequency and portion of each positive and negative voltage, the droplet printing frequency will also be directly controlled. The desired AC voltage wave pattern (Figure 3.12) was first generated in the computer with Waveform Builder software. The generated voltage wave pattern is sent to function generator and stored in the function generator. Once the function generator is on, it will send the pulsed voltage signal to the voltage amplifier, and it will amplify the voltage to the desired level, and then sent to the printing system. In this square AC voltage printing process, AC voltage frequency, duty cycle and AC voltage amplitude are the three main parameters that will affect the printing process. The AC voltage frequency is used to control the printing frequency, the voltage amplitude and duty cycle are used to produce a droplet. For the voltage

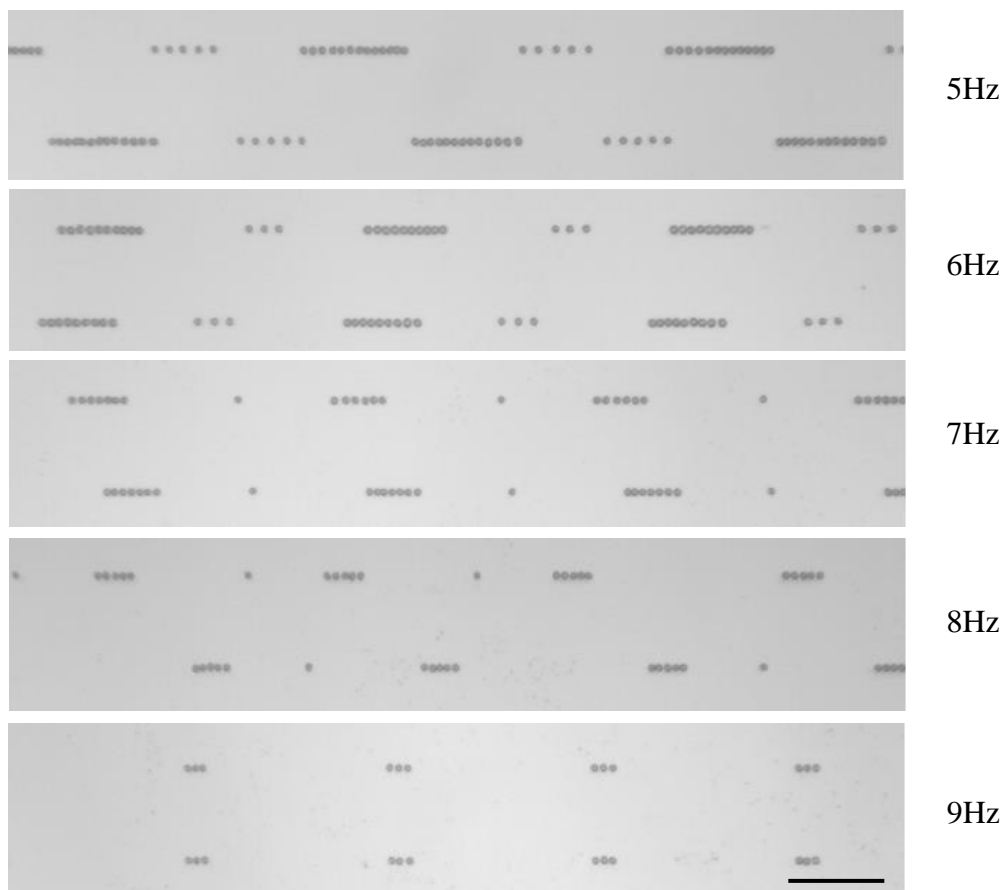


Figure 3.13 Printing result under different AC voltage frequency  
(Scale bar: 50  $\mu\text{m}$ )

amplitude, it has to be selected carefully to provide enough electric field to allow the ink form a meniscus and eject a droplet, and the duty cycle and frequency will determine the number of droplets that will be ejected from meniscus in each cycle. Similar to DC voltage, the larger voltage will produce more droplets when keeping other parameters as constant. So this study will focus on the duty cycle and frequency. Different from the DC pulse voltage, the electrical polarity will change in a cycle, which means the droplet may be ejected at both negative and positive duration in a cycle.

To find the affection of the frequency on the printing behavior, a constant duty cycle will be selected as 50%, which means in one cycle, the duration of the positive voltage and negative

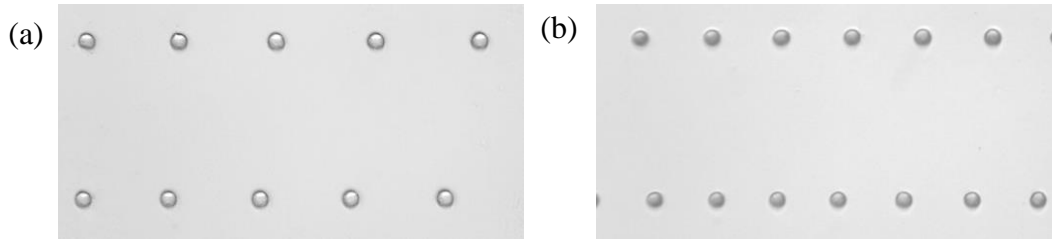


Figure 3.14 Printed droplet under continuous DC voltage of (a) 900V and (b) - 900V.

voltage is the same. The voltages for both positive and negative are selected as 600V and -600V. Figure 3.13 is the printing results when increasing the AC voltage frequency from 5Hz to 9Hz. The printing speed is 1mm/s, and with measuring the spacing between droplets, the printing frequency is still as same as selected frequency. However, it is clearly shown that in one cycle the number of the printed droplet during one polarity of the voltage is different from the other polarity of the voltage. When increasing the frequency to 9Hz, no droplet is generated in one polarity in one cycle. This may be explained that the quantity of generated mobile ions or the gathering speed of the mobile ions are different under positive and negative voltage, and both positive and negative voltage will inhibit each other that will reduce the droplet generation.

In order to produce one droplet in each polarity duration, duty cycle has to be changed accordingly to allow both negative and positive voltage have the ability to produce one droplet. Before finding the value for duty cycle, we have to find out which voltage will generate more droplets when all the printing parameters are the same. Two experiments have been performed and the results are shown in Figure 3.14. All of the printing conditions are the same for those two experiments except the voltages. From the results, when applying a positive voltage, the printed droplet frequency is less than apply a negative voltage to the system, which means applying negative voltage will easier to generate a droplet. Based on the experiment, we will reduce the duration time for negative voltage and increase the duration time for positive voltage. Based on

the previous result, we can assume that the group that contains more droplets in the Figure 3.13 are printed under negative voltage, so we will decrease the negative voltage duration to 40% of the cycle. The applied voltages are still 600V for positive voltage and -600V for negative voltage, and the AC frequency is selected as 6Hz. Figure 3.15 (a) shows that when using a 40% negative voltage duty cycle, the number of the droplet printed during negative voltage is still little more than the number of the droplet printed in positive voltage, so negative voltage duration has to be decreased. Once the negative duration reduces to 30% in one cycle, finally one droplet is produced in both negative and positive voltage, which illustrates that with this parameter setting, negative and positive reach to a good balance, so only one droplet is ejected in each duration. This result also shows that with carefully selected duty cycle and frequency for AC voltage, it has the capability to control the EHD printing behavior with respect to the droplet printing speed, which enables high-resolution printing on an insulating substrate.

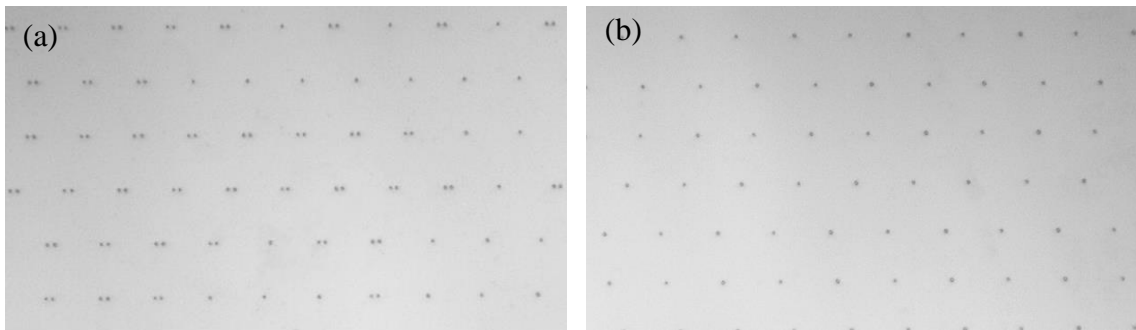


Figure 3.15 Printed droplet under different duty cycle (a) 60% positive voltage and 40% negative voltage (b) 70% positive voltage and 30% negative voltage.

### 3.4 EHD 3D PRINTING

The advantage of using phase-change ink is that the micro-scale droplet will rapidly change its liquid phase to solid phase once it printed onto the substrate before contact with the following droplet. With this unique property, this kind of ink has the capability to be used to build 3D structures layer by layer. In this study, a DC voltage is selected for this printing system

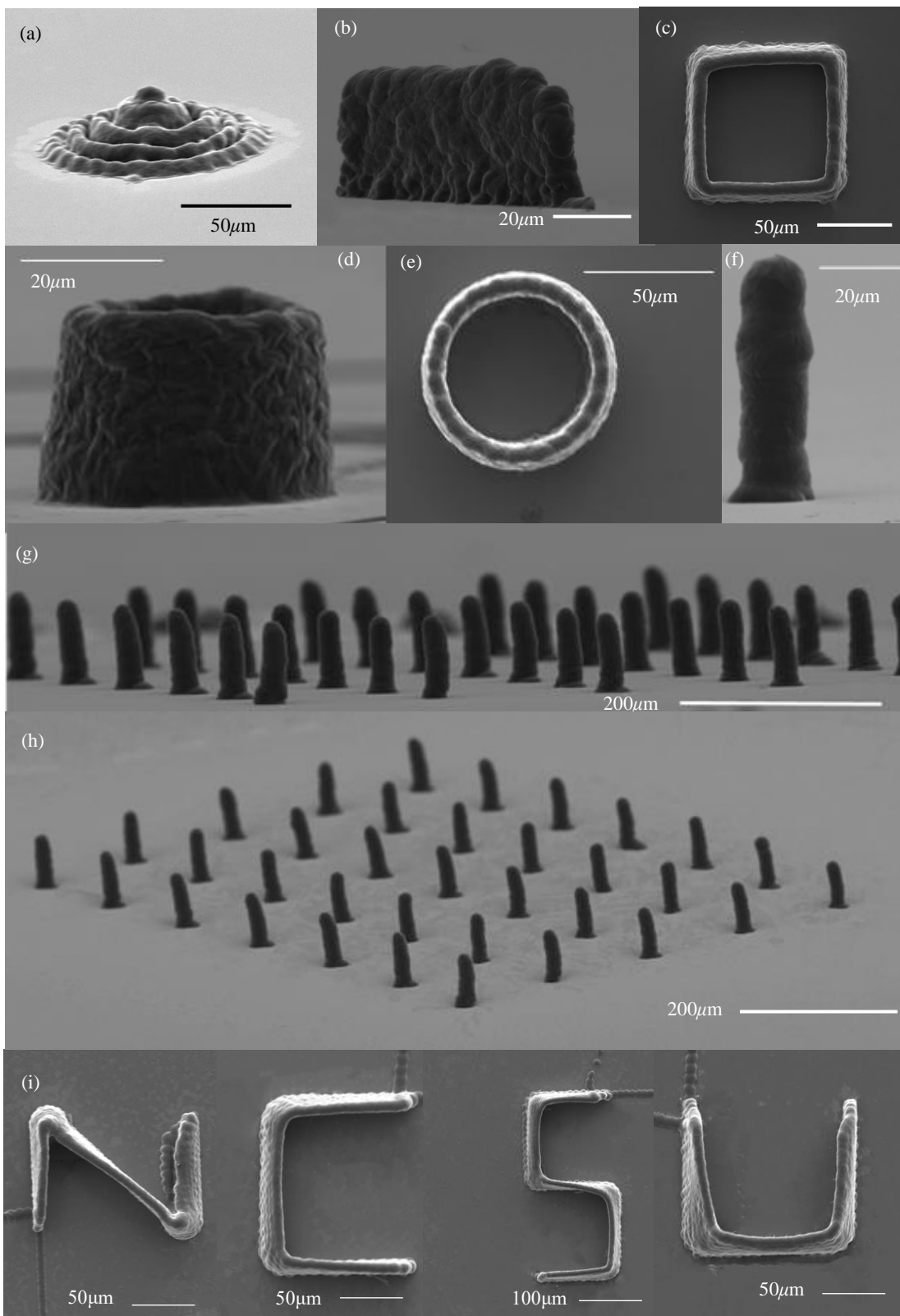


Figure 3.16 Micro-structures printed from EHD printing process (a) pyramid (b) Single layer wall (c) Rectangle tube (d,e) circular tube with thin walls. (f) Close view of a single pillar (g,h) Micro-pillar array matrix (i) 3D letter of NCSU.

and based on the characterization process; the optimal parameters are selected for the 3D structures printing. The standoff distance is set to 150 microns, and the applied voltage is set to 950V. When using a lowing voltage, large dimension of the droplet will be printed. During the printing process, the resolution of the structure has reduced due to the overlap between printed droplets, which cannot enable high-resolution printing. If the applied voltage is too high, the detached droplet will have a much higher in-flight speed, which will increase the impact energy to the substrate or the printed droplet, and this will increase the chance to damage the printed features and make it difficult to build the 3D structure. Moreover, higher voltage will bring smaller droplet and higher droplet deposition speed, and this will bring more challenges for controlling of overlap between droplets. So a proper voltage value has to be selected. When selecting a voltage of 950V, the single droplet has a dimension of about 10 microns along with a proper jetting speed, which has a good controllability. The stage moving speed will be selected according to the different structures. For example, when printing of pillar, the stage moving speed will be zero until finish printing one pillar, but when printing the circular tube, the printing path will be repeating a circle pattern with an absolute value of 0.1mm/s to ensure a good overlap between each two droplet and two layers, so this feature can be fabricated with very smooth edges. Before printing the 3D structures, the test processes have to be performed to ensure the printing quality (surface finishing, the overlap between each layer, and printing resolution) of the structures with using the optimal parameters. Once finished the test procedure, the system is ready to print 3D structures. Figure 3.16 has shown some micro-structures, which are printed by using this drop-on-demand printing method. The structures have to print layer by layer following the program sequence and repeat printing sequences 3D structures could archive with good surface finishing. Figure 3.16 (a) shows a pyramid with the largest diameter of 100 $\mu$ m, and (b)

shows a thin wall, which printed by moving the nozzle back and forth without secondary axis movement. (c) to (e) are 3D rectangle and circular tubes with a maximum height of about  $50\mu\text{m}$  and a wall thickness of  $6\mu\text{m}$ . All of those structures have a printing resolution of one or two magnitudes better than the resolution of traditional 3D printing. Figure 3.16 (f) and (h) show some 3D pillars, which have a height of around  $100\mu\text{m}$ , and diameter of  $15\mu\text{m}$ , and this gives a respect of ratio of 6.6. Those 3D pillars are directly printing by ejected single droplet when fixing the nozzle and the next droplet will fall to the location right on the top of the previous droplet. Figure 3.16 (i) has shown the printing ability to print letters. Those letters are also print layer by layer with a good finishing and smooth corners.

Currently, those 3D structures' height is limited by the configuration of the printing system. The electrode is placed under the substrate, which made this system not independent from the substrate. The overall electric field intensity will be distorted when the structure is building up, and when the structure is close to the nozzle, the printing process will become uncontrollable. Moreover, the printed structure height cannot go over the standoff distance between the apex of the cone and substrate, because the ground electrode is placed under the substrate. However, this limitation could be solved by introducing a new printing head design that integrated ground electrode into the printing head which will make that printing system independent from the substrate.

### **3.5 CHAPTER SUMMARY**

This chapter, we have introduced a phase-changed ink (wax) for the high-resolution EHD printing. The phase-change ink will change the phase from liquid to solid once it's ejected from the nozzle and deposited to the substrate, which enables high-resolution 3D structure printing with EHD technology. A series of characterization processes have been performed for this high-

resolution EHD printing process. In the continuous DC voltage printing, only one main parameter (applied voltage) will affect the printing process, droplet size and printing frequency, which makes difficult to control the printing speed and droplet size at the same time. However, when introducing a pulse DC voltage into the printing system, three factors (voltage, duty cycle, and pulse frequency) will affect the overall printing process. We have characterized the effect of all three factors on the printing behavior, and the result shows that the DC pulsed voltage indeed can control the droplet deposition speed and size. An AC pulsed voltage printing has also been studied. Three factors, voltage, pulse duty cycle, and pulse frequency have been characterized, which provide another printing condition that can print high-resolution droplet with controllable droplet deposition speed. We have also demonstrated the capability of using phase-change ink to print 3D structure by using EHD printing approach. With a properly selected voltage, this printing method gives high resolution and high aspect of ratio 3D structures with sub-10  $\mu\text{m}$  resolution.

## **CHAPTER 4 MODELING OF EHD 3D PRINTING PROCESS**

In this chapter, a complete finite element analysis (FEA) model has been created to study the high-resolution electrohydrodynamic (EHD) printing process using a phase-changed ink (wax). The overall EHD printing process has four stages (droplet formation, droplet in-flight, droplet impact and spreading, and droplet settlement on the substrate), which will be modeled separately. The first model will simulate and study the droplet formation and size at the apex of the Taylor cone, the charges in the generated droplet and the electric field intensity/distribution between the nozzle and the substrate. The second model will be calculated the droplet in-flight velocity by considering the total force experienced by the droplet, including electrostatic force and drag force. The impact speed will be obtained from the second model and then used in the simulation for the models of the third and fourth stage. The last two stages will be simulated together using Fluent, and the final result of the simulation will show the droplet footprint size on the substrate.

### **4.1 MODELING FOR DROPLET FORMATION**

Modeling of the EHD printing processes is essential for understanding the mechanism of the EHD printing, improve process control, and predicting the printing process. A fitted model can provide a prediction for the droplet dimension under different system configurations or process conditions for the future printing, and a good model can also give a guide for setting the optimal printing parameters to obtain the desired droplet size. Due to the highly complex and coupled physics of the EHD printing processes, obtaining an accurate analytical solution to describe the printing behavior was extremely difficult. So far, no groups have developed a complete model to simulation the entire EHD printing process with given material properties and printing conditions. In this study, two separate simple models were brought out to replace this

complex coupled fluidic and electrical EHD printing model. The two models were used to describe those four different printing stages during the EHD printing. The first model was used to model the first two stages, which is the droplet formation and in-flight to substrate under an electrical field. In this model, only two competitive force would be analyzed, which were surface tension force and electrostatic force, and this model was simulated using Ansys Mechanical APDL. The second model was used to simulate the droplet impact and settlement once it printed onto the substrate. In this model simulation, droplet spreading and solidification will be taken into account, and this model was simulated using Ansys Fluent.

In order to compare the model result and experimental result, the footprint and size of the printed droplet were scanned and imaged by using Atomic Force Microscope (AFM). Due to the phase-change property of this printing ink, the dimensions and volume can be easily measured once the droplet was printed on the substrate, and this property can also provide valuable quantitative information for process modeling. For each different printing conditions, diameter, height, and volume of droplets after solidification will be measured and recorded by the AFM.

For the modeling the droplet formation, we have to establish an appropriate printing model first. In the drop-on-demand EHD printing, due to the interaction of the electrostatic force and surface tension, a cone shape as known as Taylor cone will form at the apex of the nozzle, and the droplet will eject from the apex of the Taylor cone. So, in order to simplify this process, we only analysis the pending state of the droplet at the apex of the meniscus (Taylor cone), and we assumed that the pending droplet has a hemisphere shape. At this state, the droplet with a fixed diameter has the largest surface tension, and it is about to detach from the meniscus when the electrostatic force is large enough to overcome the surface tension force. Based on this pending state, we also assumed that the meniscus that formed at the end of the nozzle tip had a

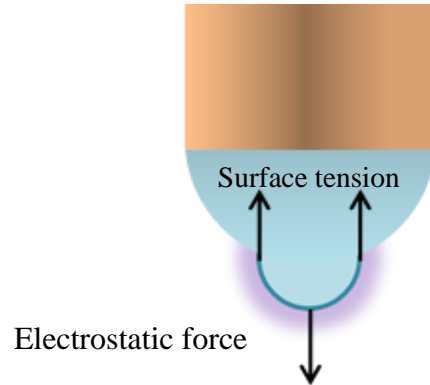


Figure 4.1 Schematic configuration for FEA modeling of the electrostatic force and surface tension on the droplet.

hemispherical shape. Due to the wetting of the melting wax, the diameter of the meniscus was as same as the size of the outer diameter of the nozzle tip. The scheme of the developed model is shown in the Figure 4.1. In the EHD printing system, both nozzle and ink will be connected to a high voltage and affect the overall electric field strength and distribution, so a printing nozzle will also be considered in the simulation. The nozzle in the model will be presented by the outline of its original shape, and inner structure of the nozzle will not be built in this model because the inner structure of the nozzle will not affect the electric field distribution and intensity. Also, no materials will be simulated inside of the nozzle, because we only studied the pending state of the droplet, and at this state, no ink flow will occur in the simulation. The simulation focused on the space between the nozzle and the ground electrode, and the substances between the nozzle and ground electrode are the air and the substrate. The substrate is a microscope slide, which is made of silica with a relative permittivity of 7.78. The relative permittivity of the air will be set to 1 in this simulation for the easy computing.

The model built in the Ansys APDL is shown in the Figure 4.2. The black lines in the middle of the (a) indicate the outer shape of the nozzle and the horizontal line indicated the top surface of the substrate. In the (b) and (a), curve lines are the meniscus and pending state droplet. The Area 1 in the (a) represents the air, and the Area 2 represents the substrate. Once finished

mesh process, the high voltage will be applied to the contour of the nozzle, meniscus, and

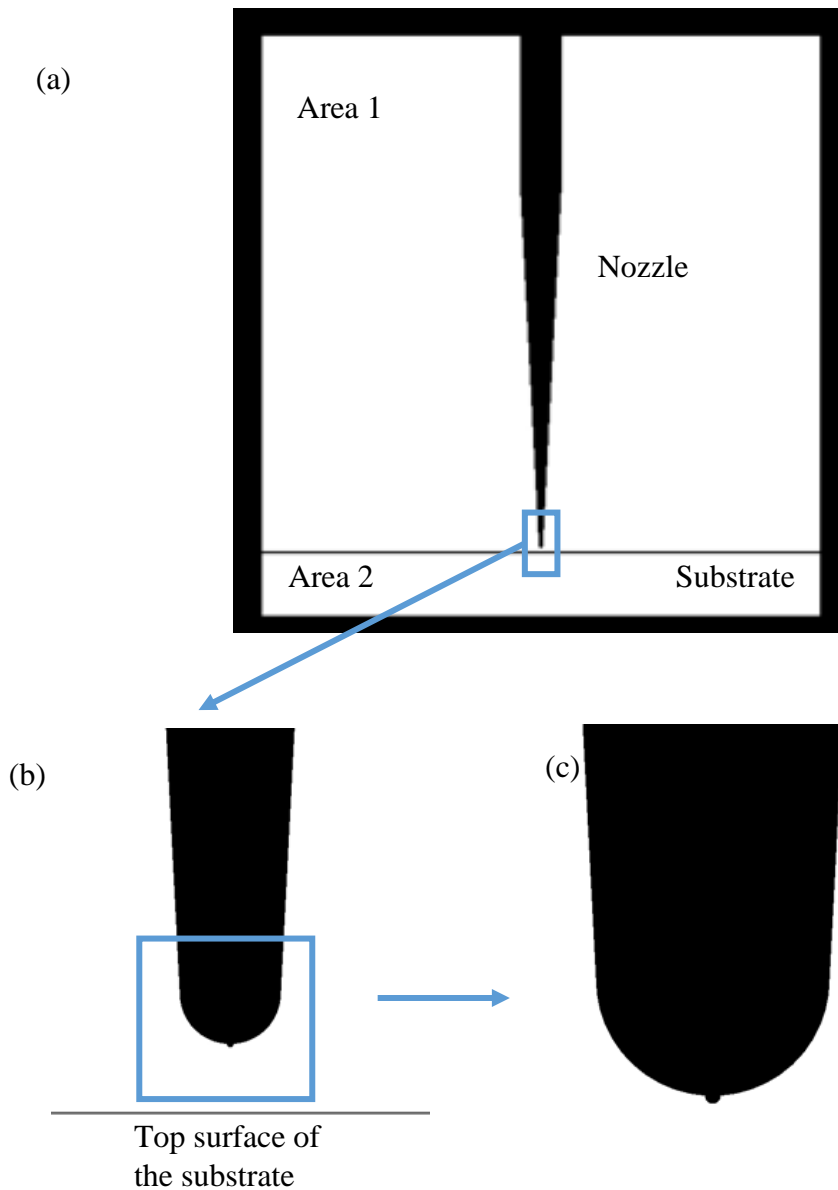


Figure 4.2 (a) The created model for the simulation (b) and (c) The zoomed in picture around the nozzle tip.

droplet. In our e-jet system setup, the ground electrode is placed under the substrate, so in this modeling, the zero potential will be applied to the bottom of the slide. Figure 4.3 is the picture of after applying all voltage load to the nozzle, meniscus, droplet and bottom surface of the substrate. Those lines with red triangle marked in the Figure 4.3 represent the applied voltage

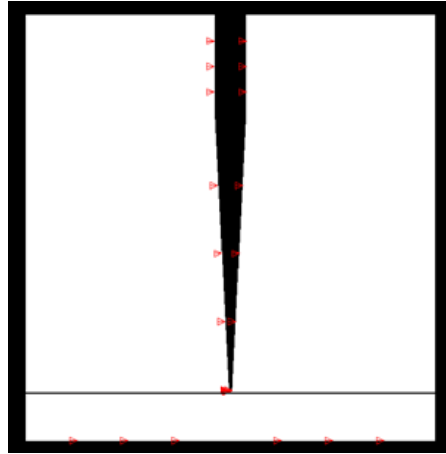


Figure 4.3 The model after applying voltage load to the nozzle and bottom surface of the substrate.

load. This simulation is trying to find the electric field intensity, charges on the droplet and electrostatic force at the pending state of the droplet about to detach from the Taylor cone. So the output of the simulation result will be the electric field intensity, charges and electrostatic force around the droplet. The total electrostatic force around the droplet can be calculated by adding up all the electrostatic force on each nodal that around the droplet. By using extract nodal command, all the nodal on the droplet can be extracted from the model, and the charges and electric field strength on each nodal can be obtained from ANSYS. After having those numbers, the total force act on the droplet can be obtained. Figure 4.4 shows the simulation result of electric field strength around the droplet with a given condition (nozzle diameter, applied voltage, droplet diameter). The previous study [111] had already studied the relationship between electrostatic force and voltage, droplet size, and tip diameter, and based on the previous study, an empirical equation with a power law fitting could be used to express the electrostatic force. The equation is a function of voltage  $V$ , droplet diameter  $D_d$ , and nozzle tip diameter  $D_N$ , and it is expressed as  $F_e = cV^{k1} D_d^{k2} D_N^{k3}$ . Since the electrostatic force can be directly calculated from the simulation, we could calculate the index value for  $c$ ,  $k1$ ,  $k2$  and  $k3$  using control variables methods. By changing one parameter at a time and fix other parameters, a series of simulations are performed, and by

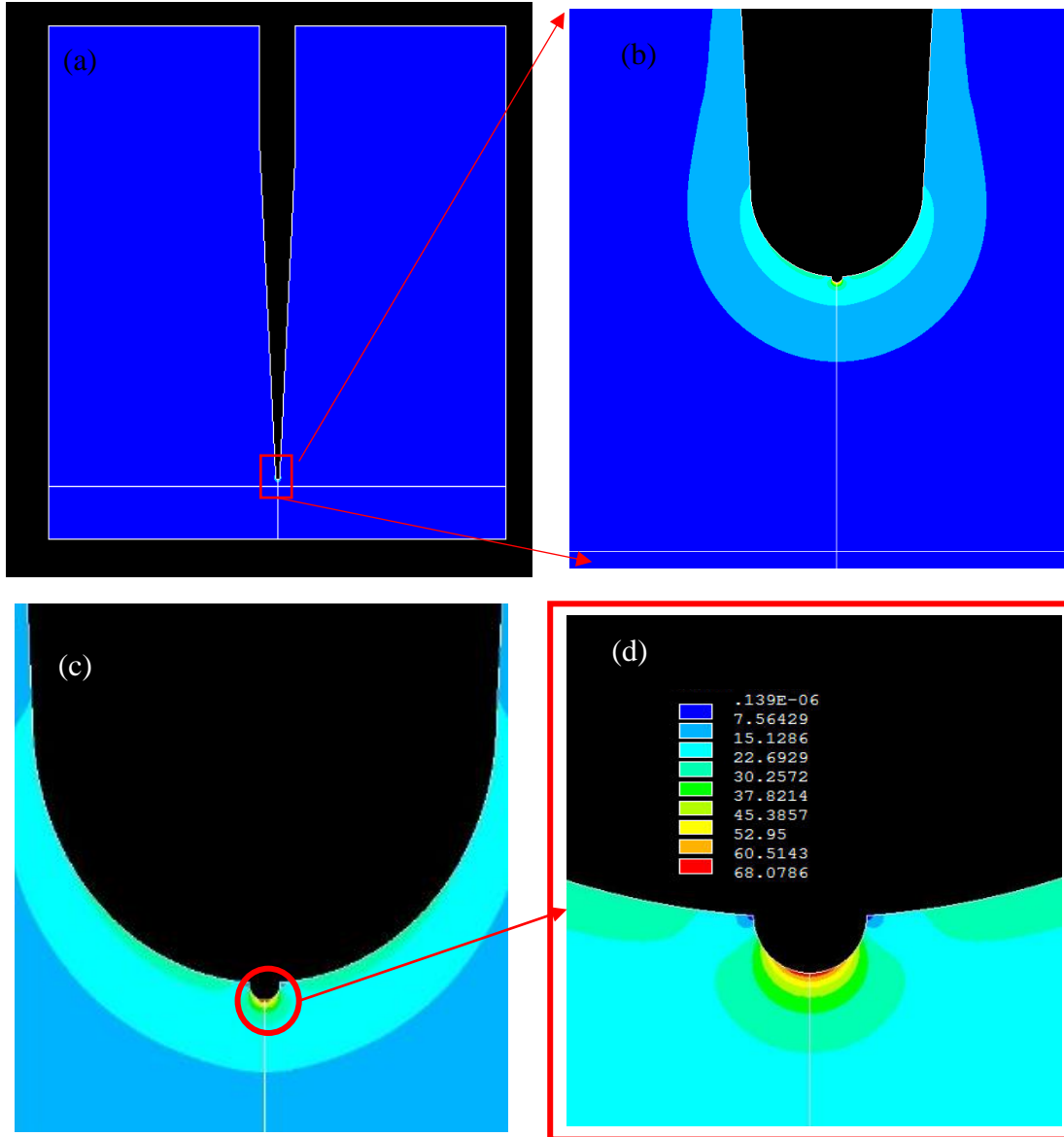


Figure 4.4 (a) The picture of the model after solved. (b) and (c) The electric field distribution round the meniscus. (d) Electric field intensity around the nozzle tip during droplet ejection.

comparing the simulated results, the index for changed variables can be calculated directly. This equation has provided the relationship between electrostatic force and printing conditions. Based on the calculation and simulation results, different nozzle sizes will result in a different coefficient  $c$  in the equation. For the nozzle with a diameter of  $50 \mu\text{m}$  used in our study, the final equation is  $F_e = 3.46e-6 V^{2.0} D_d^{1.702} D_N^{-1.078}$ .

In EHD printing, two competing force (electrostatic Coulombic force and surface tension force) would affect the printing processes, which shows in the Figure 4.1. The electrostatic force will provide a force to drag the droplet out from the meniscus, but the surface tension will try to hold the droplet at the meniscus. When the electrostatic force is larger enough to overcome the surface tension force, a droplet would be ejected from the apex of the meniscus. In EHD printing, the surface tension force is expressed as  $F_s = \sigma \pi D_d$ , where  $\sigma$  is the surface tension coefficient of the melting wax (mN/m). At the droplet pending state, the droplet has reached the maximum diameter, and at this time the electrostatic force is equal to the surface tension force. When connecting two equations together  $F_s = \sigma \pi D_d = F_e = c V^{k1} D_d^{k2} D_N^{k3}$ , the droplet diameter  $D_d$  could be express by other parameters, which give us an equation of  $D_d = \left( \frac{c V^{k1} D_N^{k3}}{\pi \sigma} \right)^{\frac{1}{1-k2}}$ . This equation provides a method to calculate the pending droplet diameter, and the solution of the droplet diameter could be calculated graphically as in Figure 4.5 (a). The area of the electrostatic force of a given voltage that is above the surface tension force line indicates that the electrostatic force is larger than the surface tension force, which will produce a droplet with a certain diameter from the nozzle tip. Using this method, the pending droplet diameter could be calculated by using the intersect point of the surface tension force line and electrostatic force curve line under certain nozzle tip diameter with a given voltage.

Due to the phase-change printing material used in EHD printing, the volume of the printed droplet on the substrate could be directly measured by using AFM, and the droplet in-flight diameter of the experiment could also be calculated. During the droplet in-flight, we assume the droplet has a sphere shape, and once the volume of the printed droplet is measured, the experiment dimension of the droplet in-flight can be calculated easily. Then this experiment

data will be used to compare with modeling droplet diameter result to validate the FEA model. The experiment result of droplet diameter in-flight and the FEA modeling predicted droplet diameter is plotted in Figure 4.5 (b). Based on the comparison result, the FEA results have a good match with the measured droplet dimension, and the maximum error is less than 10%. The prediction error between the experiment results and FEA modeling result may be caused by the measurement error of the nozzle diameter or the different surface tension of the printing ink for different tip due to the temperature variation.

#### 4.2 MODELING FOR DROPLET IN-FLIGHT VELOCITY

Droplet impact velocity is important for studying of the droplet impact and settlement on the substrate. The critical variables that need to be solved are the droplet impact velocity on the substrate because impact velocity will determine the droplet spreading on the substrate. In this study, we have developed an analytical model to calculate the impact velocity of the droplet with using the results from FEA modeling. The schematic of the droplet in-flight model is shown in

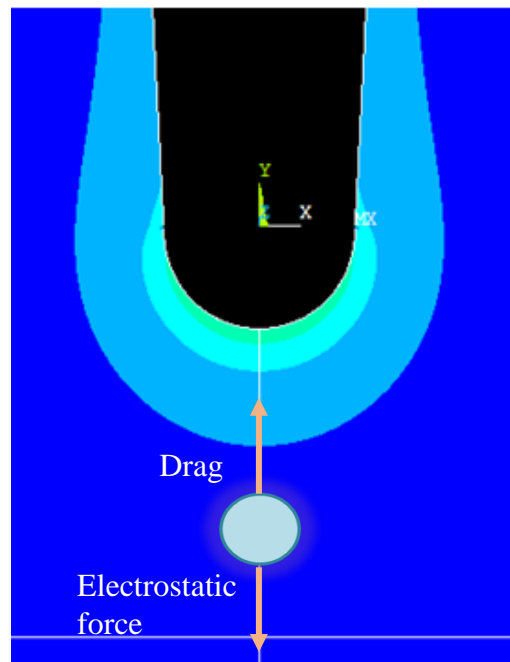


Figure 4.5 FEA model of droplet in-flight between tip and substrate.

Figure 4.5. In this model, three forces act on the in-flight droplet: the electrostatic force will accelerate the droplet in-flight velocity; on the contrary, the gravity and the viscous drag force will decelerate the droplet in-flight velocity. From the simulating result above, either the electrostatic

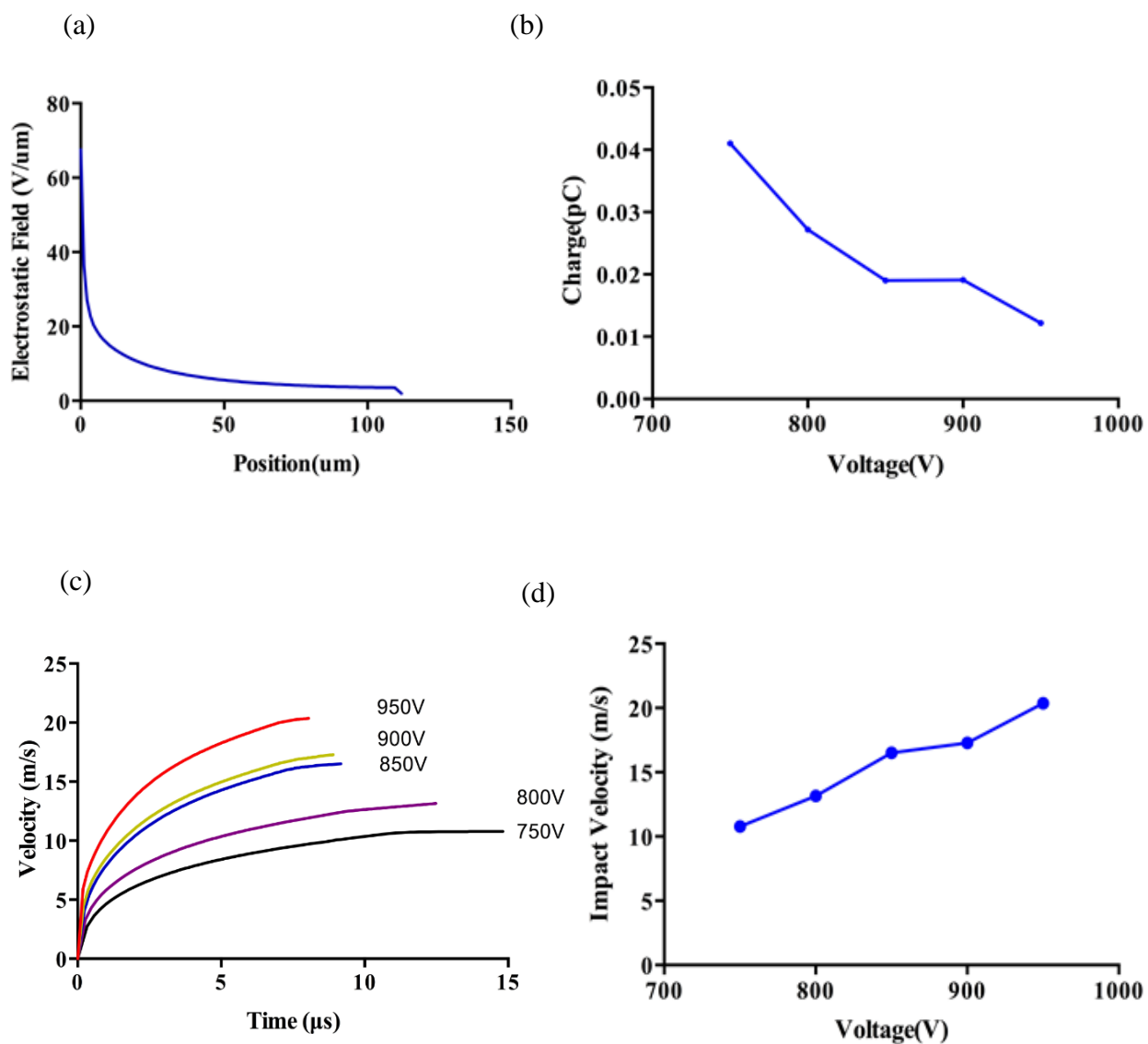


Figure 4.6 (a) Electric field distribution along center axis. (b) The amount of charge of droplet under different voltages. (c) Droplet velocity under different voltage and different flight time (d) Droplet impact velocity with different printing voltages.

force or drag force is more than six orders of magnitude larger than the gravity of the in-flight droplet, thus in this simulation, the gravity can be neglected. The expression of electrostatic force is  $F_{es}=Eq$ , and the expression for drag force is  $F_d = 1/2\rho v^2 AC_d$ , where  $\rho$  is air density,  $v$  is the droplet velocity,  $A$  is droplet cross-section area which can be easily calculated from the droplet diameter from above result, and  $C_d$  is drag coefficient. The electrostatic field intensity along the vertical ( $y$ ) direction in the Figure 4.6 could be directly obtained from FEA modeling, and the FEA modeling result is shown in the Figure 4.6. The electrostatic field intensity relies on the voltage difference between the substrate and tip, and large electrostatic field intensity will exist close to the nozzle tip, and the smallest electrostatic field strength will be on the top surface of the substrate. The charge of the droplet is obtained from the FEA modeling by accumulating the charge on nodals, which is uniformly distributed around ejection hemisphere droplet surface. Figure 4.6 (b) shows the charges on the droplet under different printing voltage. At any in-flight position, electrostatic force and drag force will always affect the droplet in-flight velocity, and the sum of those two forces at every position can be calculated from FEA simulation, and the droplet acceleration or deceleration rate can be obtained. So, the droplet in-flight velocity at any position and anytime along the vertical direction can be calculated by using the integration of electrostatic force and viscous drag force along the vertical direction. Figure 4.6 (c) shows the droplet in-flight velocity under different printing voltage at different flying time. From this figure, droplet has a large acceleration rate at the first several micro-seconds, which is due to the large electrostatic force around the printing tip and slow in-flight velocity that brings a small drag force. After several micro-seconds, the acceleration rate is reducing to a low level, which is due to the small electrostatic force on the droplet and large in-flight velocity that leads to a large drag force. When the electrostatic force is equal to the drag force, the droplet will have a zero

acceleration rate and keep a constant in-flight speed at this time. If the droplet does not impact to the ground at that time, then the droplet will begin to deceleration, because the drag force will be larger than the electrostatic force. When the droplet reached on the substrate, this in-flight speed is the droplet impact velocity. Figure 4.6 (d) shows the droplet impact velocity under different printing voltages.

### **4.3 MODELING FOR DROPLET SETTLEMENT ON SUBSTRATE**

It is very important to study the droplet impact and its settlement once it printed onto the substrate, but theoretically, it is also extremely difficult to study this impact and settlement model. We could predict the final droplet shape and final footprint on the substrate only if we can build a model to understand and simulate those processes. If the model we created has a good match with our experiment results, we could use this model to simulate the entire printing processes and predict droplet final footprint and shape with giving some certain printing parameters and ink properties. This simulation can also help us for the 3D structure fabrication to find some optimal printing conditions and process control with using phase-change printing ink.

The ejected droplet will only travel several micro-second until it impacts on the substrate, and the impact velocity could be obtained from the previous model. We use Ansys fluent to build a model, which will integrate the previous impact velocity into it, to study the droplet interaction with the substrate thermally (solidification), and mechanically (spreading by impact). The simulation of after impact will be divided into four typical stages: droplet in-flight before impact, initial droplet impact, droplet spreading, and droplet solidification, as shown in Figure 4.7. In the first stage of the model that is shown in Figure 4.7 (a), the droplet has reached its maximum impact speed and ready to impact with the substrate. In the second and third stage that is shown in Figure 4.7 (b) and (c), once droplet has impacted on the substrate, it will spread very quickly

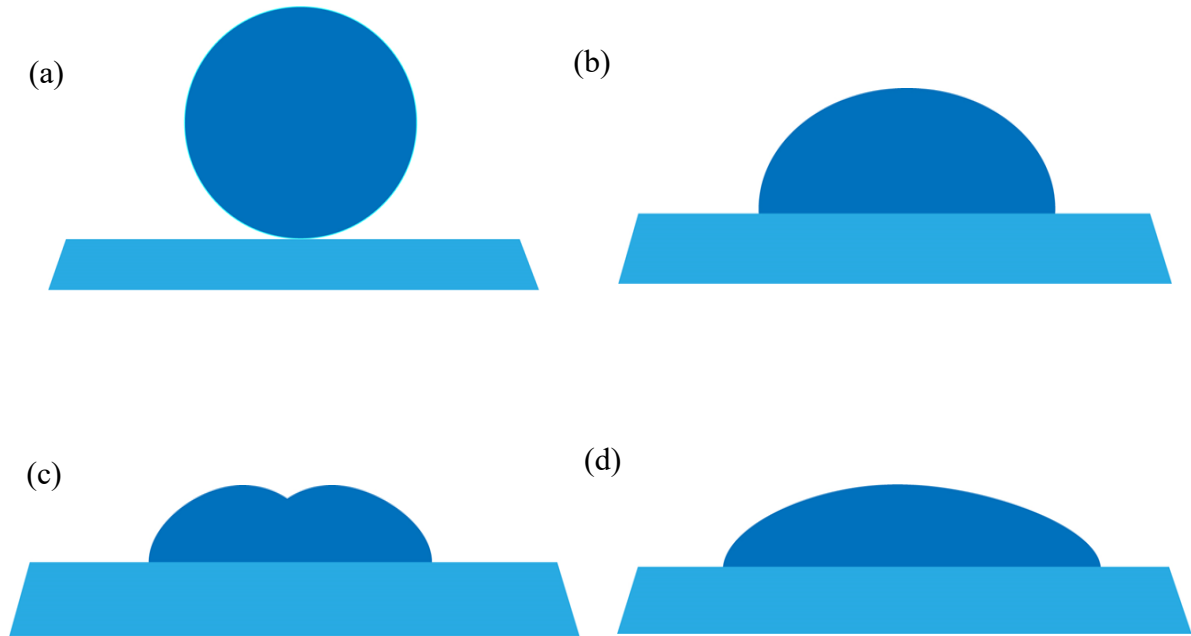


Figure 4.7 Modeling of the four stages (a) Initial statue of droplet impact (b) Droplet impact on substrate. c) Droplet spreading on substrate surface. d) Droplet settlement and solidification.

until droplet gets completely solidified, which is the last stage that is shown in the Figure 4.7 (d). The final droplet shape will be determined by two factors, spreading time and solidification time. If the solidification time is larger than the droplet spreading time, the droplet will completely finishing its spreading stage and solidified; if the solidification time is smaller than the droplet spreading time, the droplet will get solidified before it finishing spreading and that will lead to a different droplet final shape and footprint. So, in this simulation, the most critical parameter is the droplet solidification time and simulation time. The simulation time should be longer than the droplet solidification time in order to guarantee the correctness of this simulation. Precisely calculating droplet solidification time after it printed onto the substrate has to consider many factors such as ambient temperature, ink thermal properties, substrate thermal properties, etc. and this is very complicated, but in this simulation, we use a simple equation to proximately

calculate solidification time. The equation we use here is:

$$\tau_s \approx \frac{2a^2k}{3\alpha k_t} \left( \ln \left( \frac{T_0 - T_a}{T_f - T_a} \right) + \left( 1 + \frac{k_t}{2k} \right) \frac{L}{c(T_f - T_a)} \right),$$

where  $a$  is the droplet radius,  $k$  is the thermal conductivity,  $\alpha$  is the thermal diffusivity,  $T_a$  is substrate temperature,  $T_0$  is the melting droplet temperature,  $T_a$  is substrate temperature,  $T_f$  is fusion temperature,  $c$  is the melts specific heat and  $L$  is the latent heat of fusion[148]. The final estimated droplet solidification time is about 12  $\mu$ s. Based on the estimated solidification time and to ensure the droplet will get completely solidified and stabilized, we have set the total simulation time at least two times larger than the estimated solidification time. Based on the liquid ink properties (immiscible fluid, and non-compressible), the volume of fluid (VOF) theory will be used in this simulation. During the simulation, each droplet is ejected from the nozzle under different printing condition, which resulted in a different impact velocity in the droplet settlement simulation. In this simulation, all droplet impact velocities are obtained from the previous model simulation as shown in the figure 4.6. The obtained simulation results from Fluent will be collected, and import to the visual software named Tecplot 360, and this software will generate animation once the total time during is selected.

#### 4.4 MODELING RESULTS OF EHD PRINTING

The droplet settlement simulation results under different printing conditions can be directly exported from the Tacplot 360, which is shown in blue line in the figure 4.8. It clearly shows that once the droplet impacts to the substrate, it will spread very quickly, and after 2.5 $\mu$ s, the droplet spreading process is ended, which means the droplet will form its final shape on the substrate before it gets solidified. In order to verify the simulation result, some drop-on-demand printing tests have been performed with the same printing condition in the simulation process.

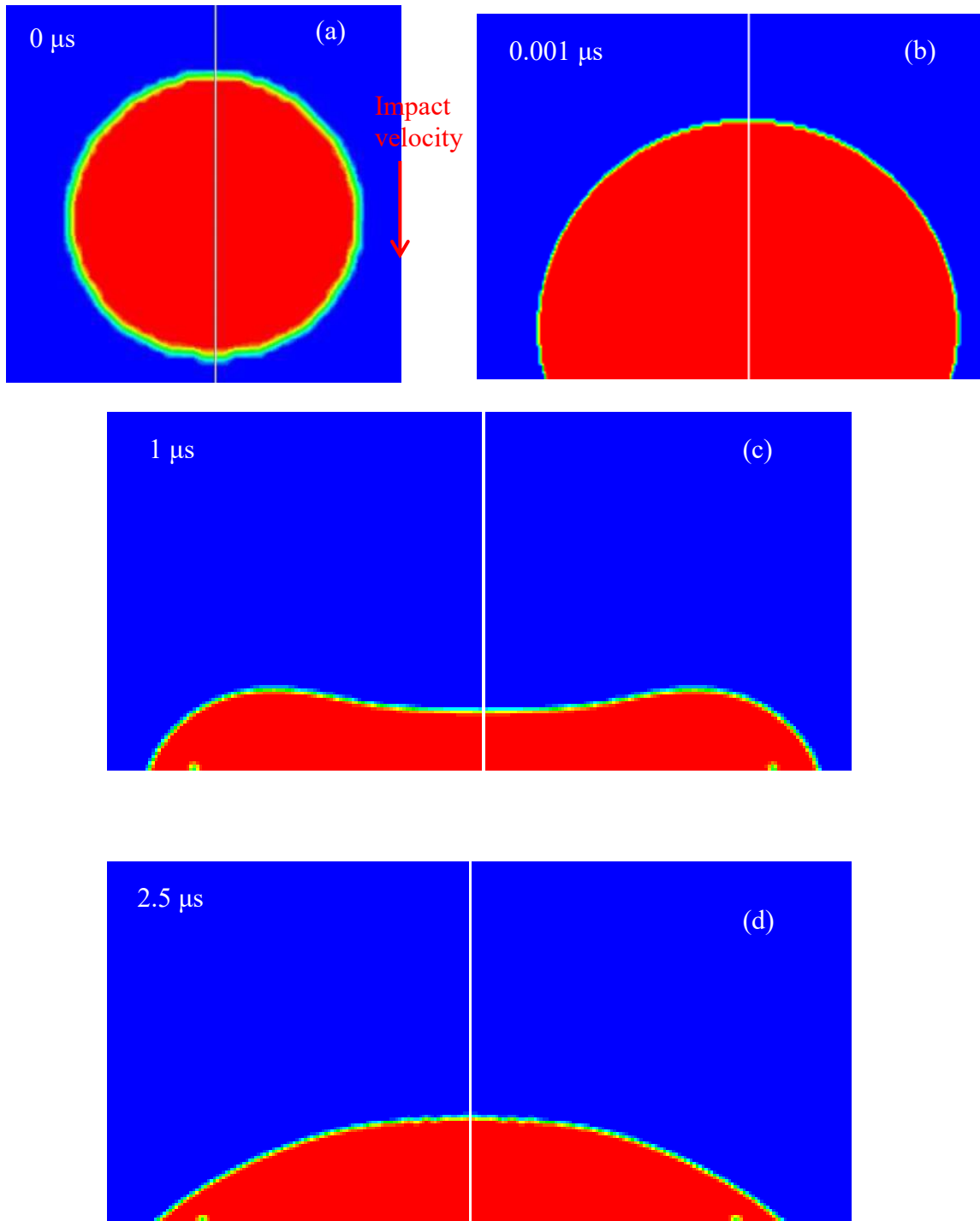


Figure 4.8 (a) In-flight droplet before impact the substrate. (b) Initial impact of the droplet on substrate. (c) Droplet spreading on substrate surface. (d) Droplet settlement and solidification.

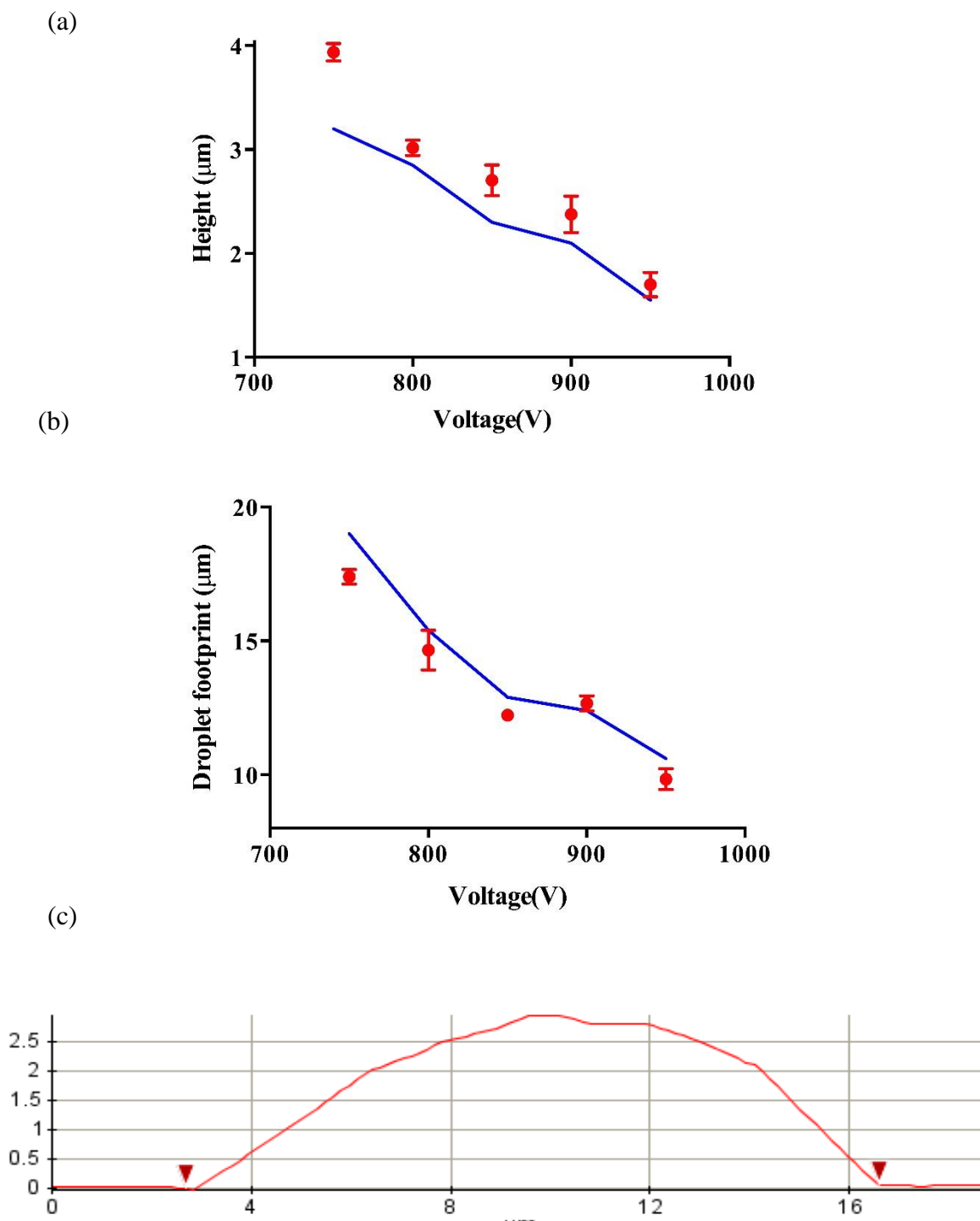


Figure 4.9 Comparison between droplets height (a) and diameter (b) from FEA (lines) and experimentally measured results (data points) at different process conditions. (c) Experimentally measured droplet cross section on substrate. (Unit of x and y coordinates is  $\mu\text{m}$ , and measurement is shown as red line).

There are five tests for each different voltages, and the final printed droplet height and footprint are measured directly from Atomic force microscopy (AFM), and the results showed in Figure 4.9. The difference between the experiment results and simulation results are less than 10%, and those variances may cause by measuring errors, turbulences during the printing process and assumptions that made in the previous simulations. Overall, the simulation results have a good match with the experiment results, which indicated that the model we have developed could effectively describe the droplet solidification and stabilization, and this complete model has the ability to estimate the droplet settlement when applying different printing parameters.

#### **4. 5 CHAPTER SUMMARY**

In this work, we have study and model the EHD printing process using a phase-change material (i.e., wax) for micro-scale additive manufacturing, which can print sub-10 $\mu\text{m}$  3D microstructures. We have successfully built simulation models for modeling droplet formation, in-flight under the electric field, impact on the substrate and final settlement in the printing process by FEA to predict droplet in-flight size and droplet footprint under different process conditions. To model the droplet formation, we focused on the two competitive force, surface tension force and electrostatic force that acted on the apex of the meniscus. By balancing those two forces at droplet pending state from the Taylor cone, the droplet in-flight diameter can be derived. Droplet impact velocity can be calculated numerically by counting the effect from the electrostatic field when the droplet travels to the substrate. Then this velocity is used to model the droplet spreading and settlement on the substrate. To validate the FEA result, we have measured the volume and droplet footprint by AFM under different printing conditions, and compare them with the model prediction, which has a good match between them.

## **CHAPTER 5 RING ELECTRODE DESIGN FOR EHD PRINTING**

In the previous chapter, the total height of the EHD 3D printed structures are limited due to the placement of the ground electrode and high voltage electrode. In the traditional EHD system setup, the substrate is placed between the ground electrode and high voltage. As a result of this setup, the printed features will affect the electric field distribution and intensity because of the dielectric constant difference between the printing material and air. As the 3D structure is building up, this affection is becoming more and more significant that will limit the fabrication height of the 3D structure. In addition, the height of the 3D structure is also limited by the distance between the substrate and the nozzle. Increasing this distance during the printing will result in larger voltage to maintain the printing process. In order to solve this problem and make the e-jet printing independent from the substrate, a new printing head design has to be created, which a ring electrode is introduced as a ground electrode, and a constant electric field intensity can be maintained during the printing.

### **5. 1 EHD 3D PRINTING SYSTEM WITH RING ELECTRODE**

#### **5.1.1 EHD Printing System**

The EHD printing system consists of four subsystems: a precision three-axis motion system, a pneumatic dispensing system, a heating system and voltage supply. Figure 1 shows the schematic setup of the printing system. The precision three-axis system has three linear motion stages with an accuracy and precision of 100nm, and three motion stages were used to control the movement of the substrate and the print head. The pneumatic system that can provide a maximum of 90psi pressure is used to provide pressure for the molten material to flow from the printing head. The applied pressure was controlled by a pressure regulator, and it is set to 4psi in this study. The heating system includes a heating rope, thermocouple, and PDI controller will

provide heat to melt the printing material with a resolution of  $0.5^{\circ}\text{F}$ . The ring electrode is fixed to the Z-axis stage with highly insulated tape, and a high voltage supply was connected to the printing head to provide a high voltage between the nozzle and the integrated ring electrode.

### 5.1.2 Printing Material

A phase-change ink Polycaprolactone (PCL) pellets were purchased from Sigma-Aldrich (Milwaukee, WI) with average Mn of 45000 g/mol and melting point about 56 to  $64^{\circ}\text{C}$ . PCL is a biodegradable and biocompatible polymer material, which has been approved by the Food and Drug Association (FDA) and this material has been widely used for tissue engineering to build scaffold structures. PCL is also a good material to be used in the micro-structure fabrication in EHD 3D printing because it has a relatively low melting point and it can solidify very quickly once printed on the substrate in order to form high-resolution 3D structures.

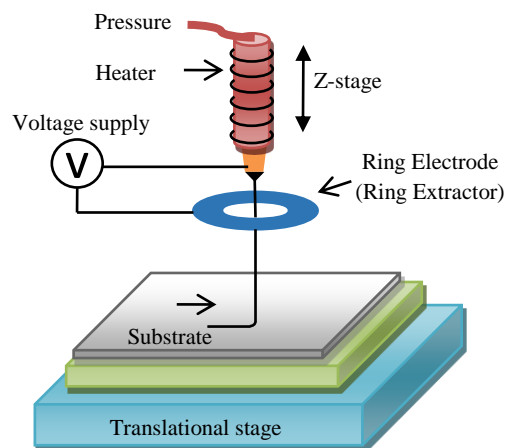


Figure 5.1 Schematic of EHD printing system with a ring extractor.

## 5. 2 RING ELECTRODE DESIGN

The purpose of the integrated ring extractor is to provide a ground electrode within the printing head system, so the ground electrode does not need to locate under the substrate. So the new printing system is a substrate independent system and standoff limitation can be eliminated,

which the affection of the printed structure to the electric field will also be reduced. In order to make this system substrate independent, the ground electrode should be separate from the substrate and integrated it with the printing head. Figure 5.2 demonstrates the ring extractor design with two important design parameters: The diameter of the ring ( $D_R$ ), and the distance between the nozzle and the top surface of the ring extractor ( $L$ ). A good extractor should have a

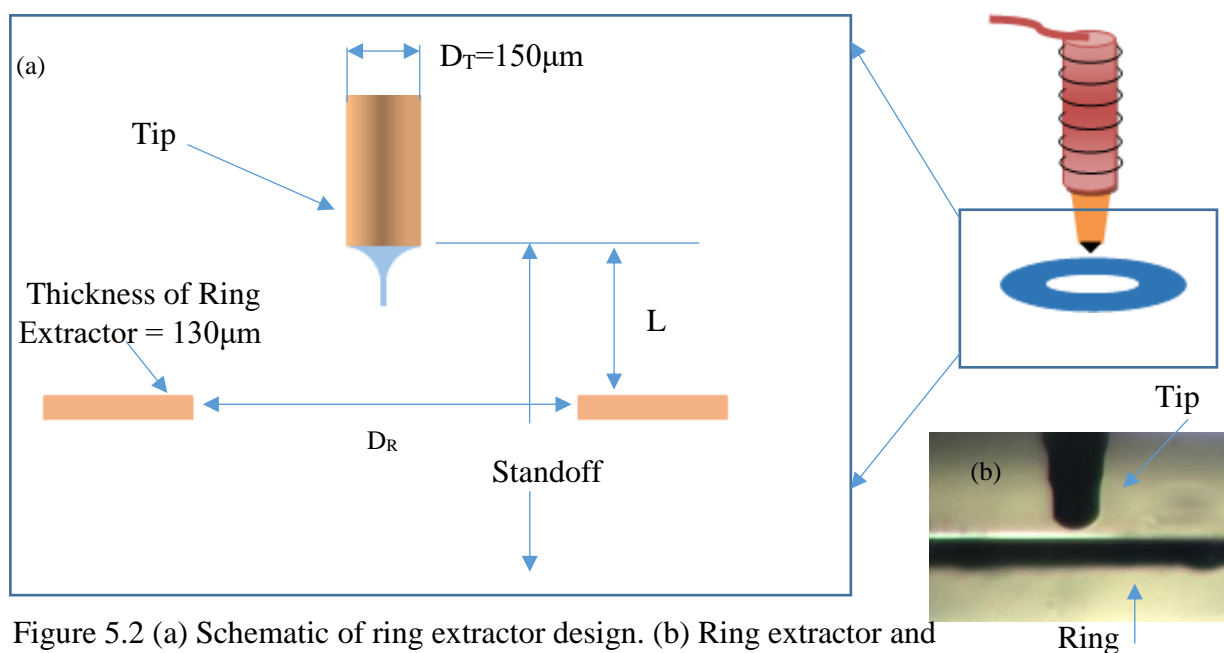


Figure 5.2 (a) Schematic of ring extractor design. (b) Ring extractor and tip picture that taken from experiment camera.

good conductivity and a very thin thickness. Thin thickness will bring less undesired electric field that caused by the inner face of the extractor during the printing, and also, the small thickness could provide us a better observation and easy process control. Based on those requirements, a very thin microscope cover glass slide (Figure 5.3) that purchase from Fisher Science is chosen as the extractor, which has a thickness of 130 to  $160\mu\text{m}$ . Due to the material of the extractor, a thin layer of a mixture of gold and platinum is coated to the top surface of the extractor for conduction purpose. The inner hole of the extractor is fabricated by laser micromachining, which has the best resolution of a few millimeters. Small inner diameter could

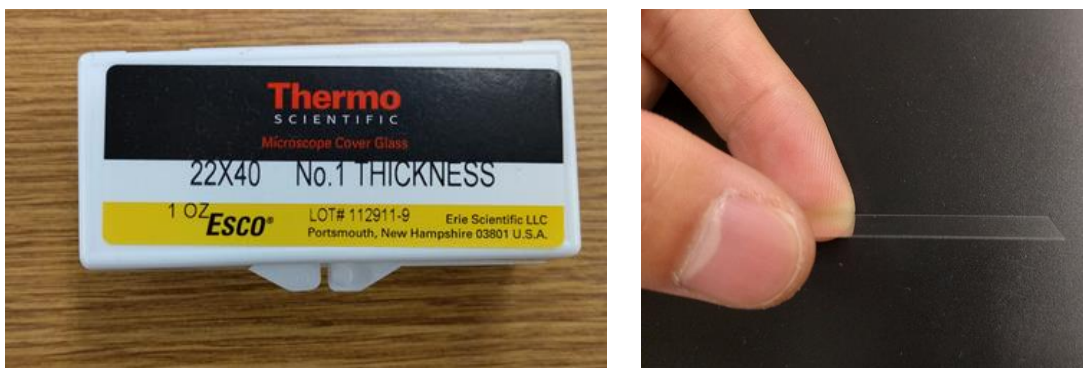


Figure 5.3 (a) Microscope cover glass (b) Vertical view of the cover glass

provide a high electric field intensity; on the contrary, it will bring more disturbances and also very difficult to control the alignment of the nozzle with the center of the hole. When the nozzle does not place in the center of the extractor, electric field intensity in one side of the extractor will larger than the other side, which the total electrostatic force is not zero on the horizontal axis. Within this distorted electric field, the printed jet or droplet will fly to the higher electric field intensity edge and leads to uncontrollable printing. In this case, a tradeoff has to be made to balance the electric field intensity and easy of system control. The nozzle has an outer diameter (DT) of  $150\mu\text{m}$ , and due to the wetting of the printing material, the real printing cone shape diameter is determined by the outer diameter of the nozzle, which is  $250\mu\text{m}$ . A parameter  $L$  is selected as the distance between the nozzle and the top surface of the extractor. When increasing the  $L$ , the electric field intensity will decrease, which means an appropriate value has to be designed carefully for a satisfactory printing condition. Among the parameters in the traditional planar EHD printing, standoff height is critical to the printing system, because different standoff height value will affect the electric field intensity and robustness of the system. But for this integrated ring extractor system, standoff height will have less influence on the printing process, because with a properly extractor design, the primary source of the electric field intensity will come from the ring extractor itself, and the influence of the standoff height on the electric field

intensity can be ignored. Based on archiving similar electric field intensity as that from the traditional planar electrode system, we have found the final extractor design parameters, the diameter of the inner hole of the extractor is set to 4mm, and the distance between nozzle and top surface of the extractor is set to 300 $\mu$ m.

### **5. 3 FEA MODELING FOR RING ELECTRODE DESIGN**

The Finite Element Analysis (FEA) of the EHD printing with extractor is important during the designing of the extractor. It can provide a guidelines for finding the best design parameters based on the electric field intensity between nozzle tip and extractor. In our previous research, a knowing working condition was found for the traditional planar electrode configuration, which a fine stable jet filament could be ejected from nozzle. In this printing setup, the distance between nozzle and ground electrode is 150 $\mu$ m, the printing voltage was set as 825V [11], and a simulation of the electric field intensity was performed based on those parameters. The simulation result will provide a standard for the ring electrode design. The purpose of the ring electrode design is to find the best design values, which could provide the same electric field intensity as it in the planar configuration, thus it could have better promise to work successfully in the printing experiments.

In the FEA simulation, we have studied a state that pending filament just ejected from the nozzle under different parameter configurations. The modeling of the dynamic EHD printing process requires the combination of fluid dynamic and electric field that is usually very complex and difficult to achieve, thus we have applied a simplified model that shows in the Figure 5.4 to study the distribution of the electric field strength and the onset condition of the printing processes. In this simplified model, we did not put too much fluid dynamic in the modeling, because the time period set in this model is too short, that the liquid printing ink could be treated

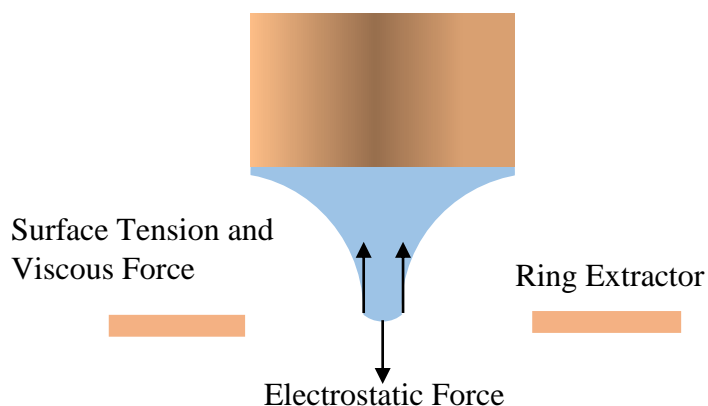


Figure 5.4 Schematic configuration for FEA modeling of the electrostatic force on droplets.

as a static object. Figure 5.4 shows the schematic configuration for the FEA modeling of the electrostatic force, surface tension force and viscous force on the filament. In the simulation, the molten PCL is treated as a dielectric material we assumed that the generated meniscus have geometry as shown in figure 5.5. The high voltage was applied to the nozzle tip and printing ink, and the ground was connected with the top surface of the ring extractor. For the planar EHD printing system, the ground was connected with the bottom surface of the substrate as a ground electrode. After applying a high voltage to the nozzle, three forces (surface tension force, viscous force and electrostatic force) were competing with each other. The sum of the surface tension force was on the Y-axis, and the direction is pointing to up. With a good ailment between nozzle and center of the hole of the ring extractor, the sum of electrostatic force was on the y-axis direct to down. When the filament ejected from nozzle, the sum of the viscous force was also on the y-axis, and direct to up, so when continuing increasing the voltage to a certain level, the electrostatic force would be equal to the sum of the viscous force and surface tension force, and this state is the pending state that the simulation is for. When the electrostatic force is larger than the total force of surface tension force and viscous force, a fine filament will be ejected from the

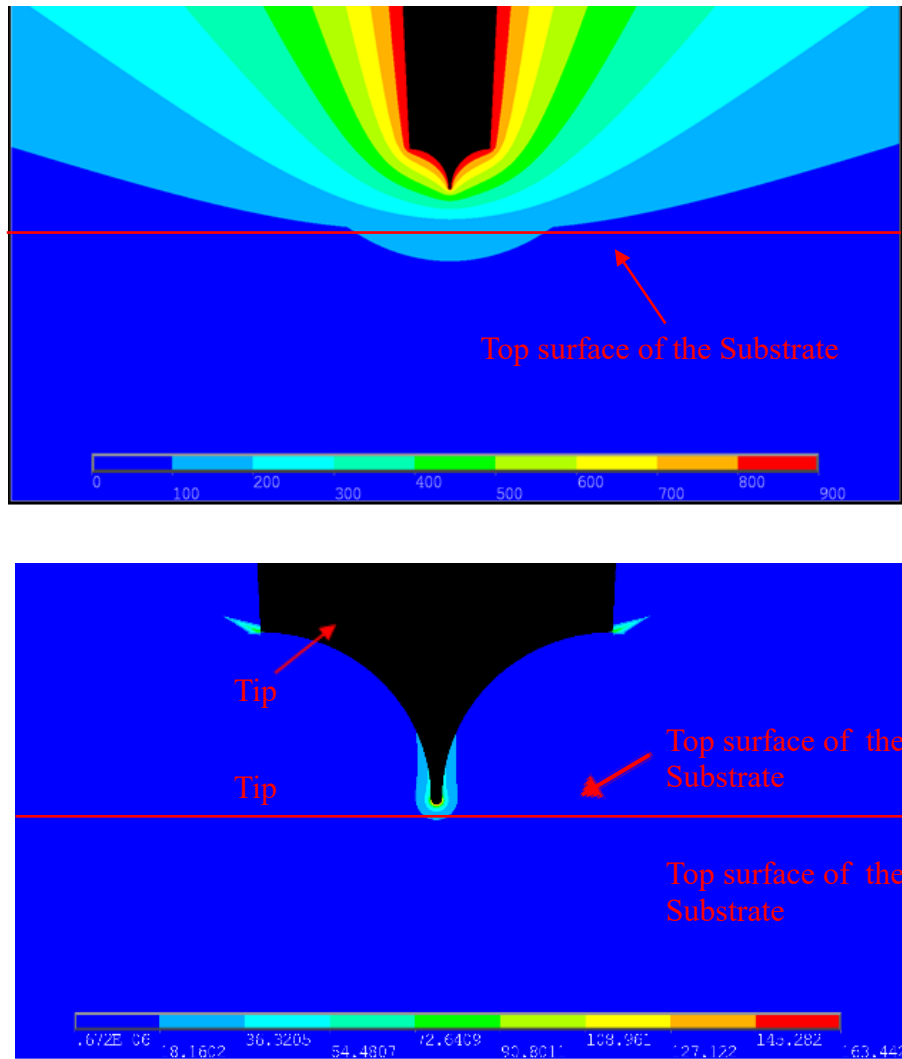


Figure 5.5 (a) Electric field potential distribution (b) electric field strength around the printing tip of non-extractor at 825v with a standoff of 150  $\mu\text{m}$  (unit of the scale bar is  $\text{V}/\mu\text{m}$ ).

top. Due to the very high viscosity of the molten PCL ink, it was very difficult for the ink to accumulate enough charges to overcome the surface tension force and viscous force at the top of the meniscus to form a droplet. As mentioned above, for the traditional planar system, find filament could eject when the printing voltage is 825V with a standoff of 150 $\mu\text{m}$ [11]. Under this condition, the electric field potential distribution and intensity is 163.4 $\text{V}/\mu\text{m}$  as shown in the figure 5.5. This value was used as a reference for the ring extractor design. In the ring extractor

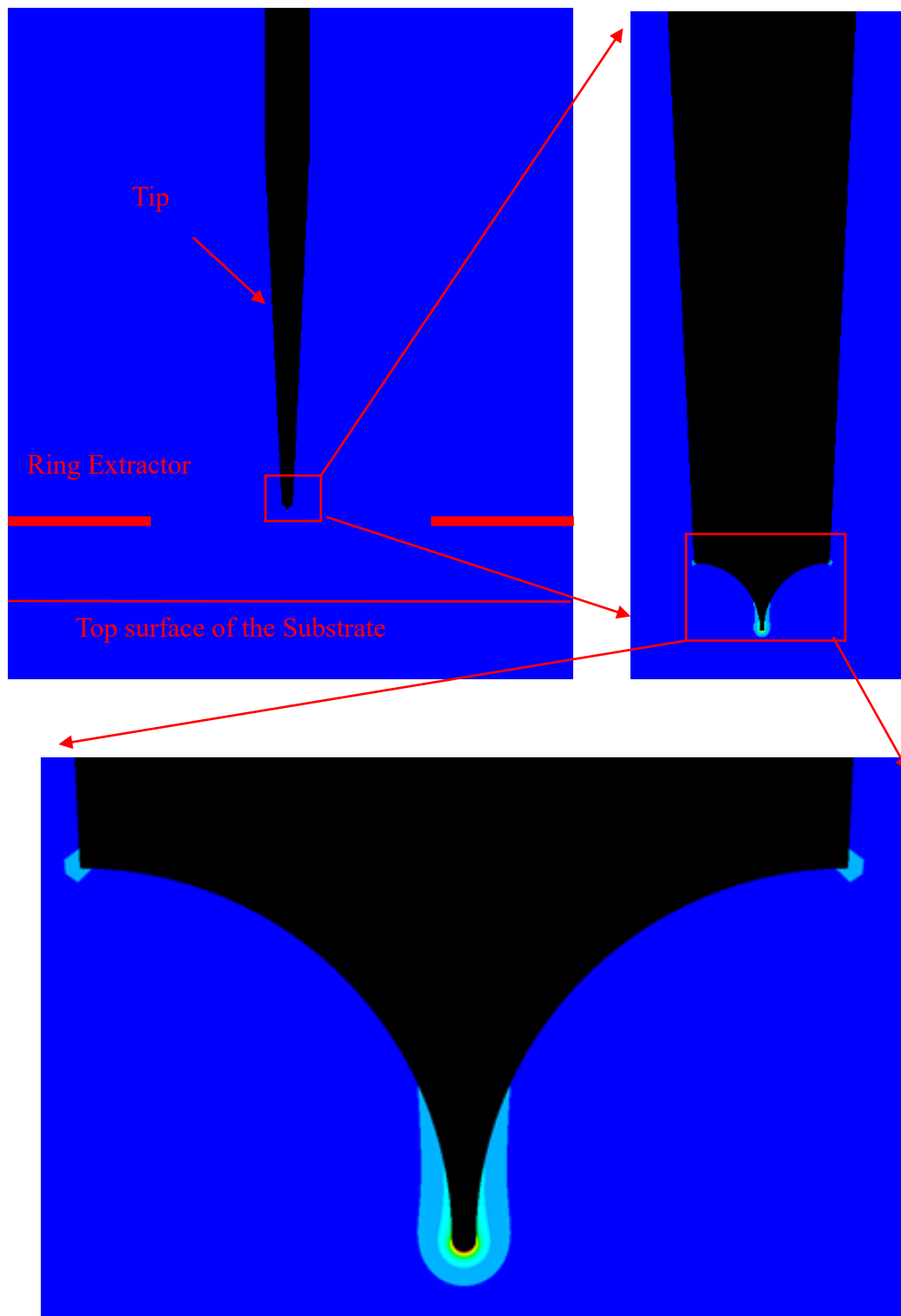


Figure 5.6 (a) (b) FEA model of the cross-section of the nozzle, ring extractor, ejected material and substrate. (c) Electric field strength around the printing tip at 1600V (unit of the scale bar is  $V/\mu\text{m}$ ).

setup, we expected to find the design parameters (e.g., the diameter of ring extractor, z-gap between the printing nozzle and the ring extractor, and voltage) that could achieve about the same electric field intensity to initiate the printing process. Due to the fact that the electric field is proportional to the square of the applied voltage, so a constant voltage of 1600V was applied to the system during the entire experiment, and the design would focus on the other parameters to meet the printing requirement.

During the designing of the extractor, we have to change one factor at a time and fixed other parameters to evaluate the effect of each independent variables. Figure 5.6 shows the FEA simulation model and the result of the electric field intensity for one design. Based on this model we have created in the previous section, the FEA results of the relationship between each design variable and electric field intensity have shown in the figure 5.7. For the simulation of the standoff affection ( figure 5.7 (a)), two constant values of  $300\mu\text{m}$  for the nozzle to ring distance and 4mm for ring extractor diameter were selected, and the result clearly shows that the substrate only significantly affects the overall electric field intensity when the standoff distance is less than 3mm. When the standoff distant is larger than 3mm, increases this distance has less and less effect on the electric field, which illustrates that the electric field intensity mainly comes from nozzle and ring extractor, so the ring extractor domains electric field strength. When the standoff distance is 5mm, the value of electric field intensity is  $162\text{V}/\mu\text{m}$ , which is similar to the field strength from the traditional planar configuration, thus indicated a feasible condition for a good EHD printing. As noticed in the ring extractor system, even the substrate isn't connected to the ground of the power supply, it still has a zero potential electrically, which will still affect the electric field intensity when the nozzle is close to the substrate, and thus the electric field intensity has an extensive increase when standoff value is less than 2.5mm. The FEA result of

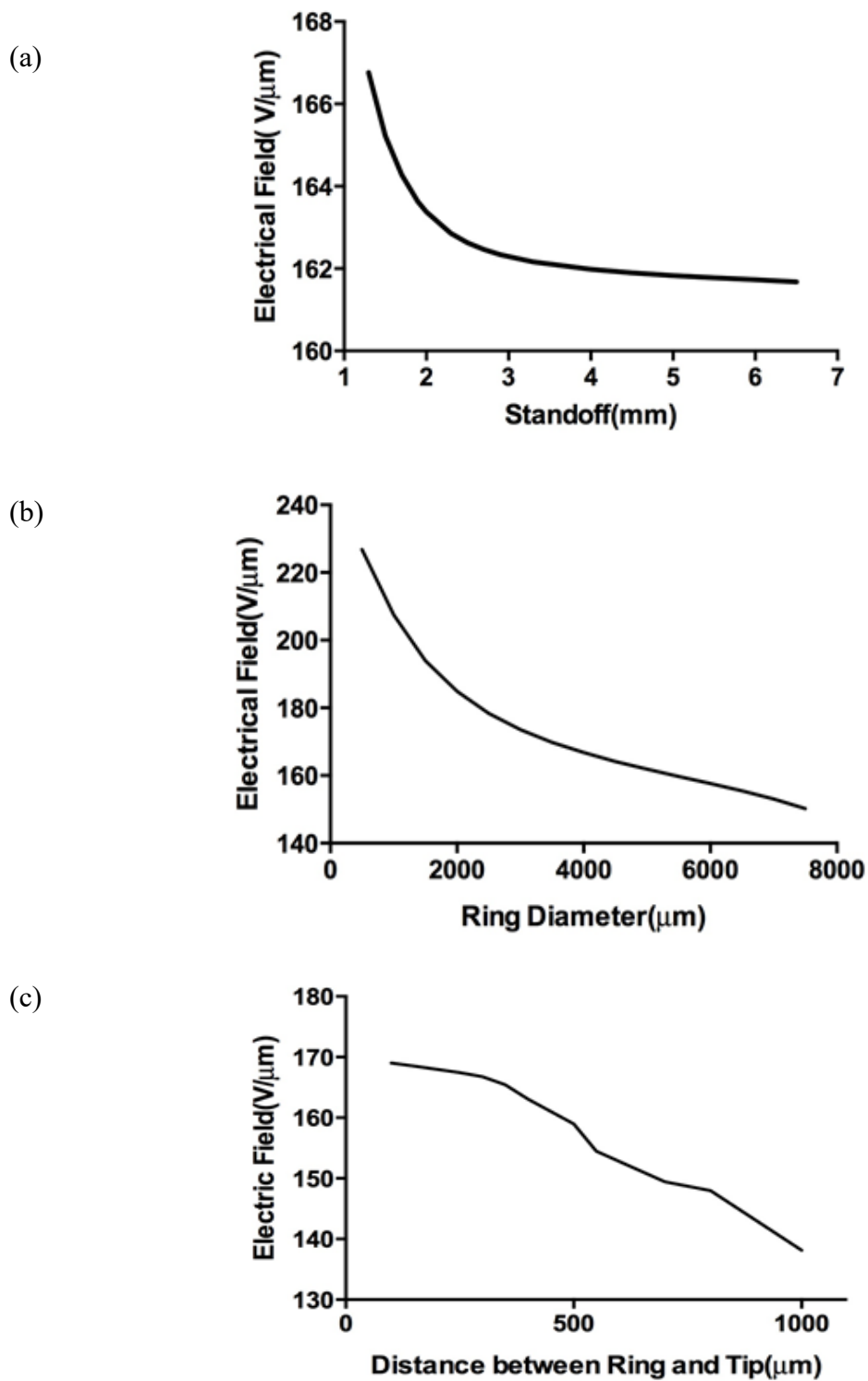


Figure 5.7 The relationships between the electric field strength and (a) standoff height, (b) ring diameter, and (c) tip to ring extractor z-distance.

standoff effect has indicated the advantage of using ring extractor for providing substrate independent printing. When applying proper values of the design of ring extractor, theoretically, we can increase the nozzle to substrate distance to a very large value that almost has zero effect from the substrate and also maintains EHD printing from the nozzle, as the electric field is mainly from the integrated ring electrode.

The inner ring diameter has a significant affection on the intensity of the electric field. When keeping a constant value of 1.3mm for standoff height and 300 $\mu\text{m}$  for the extractor to nozzle distance, the resulting electric field intensity with respect to the extractor diameter is shown in figure 5.7 (b). Increase the inner diameter of the ring electrode will increase the distance between the nozzle and the ring electrode thus lead to decrease the electric field intensity. Similar to the standoff height effect, when gradually increasing the ring diameter, the changing of the intensity is gradually decreasing, which is due to the effect of the second ground electrode of the substrate, and the substrate ground domain the electric field when the diameter of the ring is large enough. Figure 5.7 (c) shows the relationship between the z-distance (distance between the nozzle and the ring electrode) and electric field intensity. In this simulation, the constant value for ring extractor diameter and standoff height is 4mm and 1.3mm. When increasing the nozzle to ring distance, the electric field intensity will decrease rapidly, and when the distance value is 1000 $\mu\text{m}$ , the electric field intensity value is 138V/ $\mu\text{m}$  that is close to the electric field intensity without ring electrode. When remove the ring extractor and keep other parameters at the same value, the FEA result shows that the electric field strength at nozzle tip is 134V/ $\mu\text{m}$ , which illustrated that at this distance the ring electrode only has slight effect on the contribution of the overall electric field intensity at the printing head and under this condition, no filament would be ejected from the nozzle. The reason of the FEA modeling is to find the proper

extractor design parameters that could provide the similar range of electrostatic field strength as the configuration with a ground electrode under the substrate that could successfully start EHD printing. For instance, when set the voltage to 1600V, a standoff height of 1.3mm, and nozzle to ring distance of 300  $\mu\text{m}$ , the simulation result that shows in Figure 5.6 (c) indicate an electrostatic field strength of 166.761V/ $\mu\text{m}$ , which is close to the electric field strength in the non-extractor configuration. So a fine and stable jet could be expected from this system setup. When removing the ring extractor from the system under this condition, the electric field intensity will reduce about 20% to a value of 134V/ $\mu\text{m}$ , and this will lead to reducing electrostatic force about 20% accordingly, and no fine stable jet should be observed, which means in this circumstance, not enough electrostatic force could overcome the surface tension force and viscous force to start and maintain the EHD printing process.

## **5.4 CHARACTERIZATION OF RING ELECTRODE DESIGN**

### **5.4.1 Verification of Ring Extractor Design**

We have in-field tested the printing behaviors at different ring extractor designs and compared the results with the result of the traditional planar electrode setup in the verification stage. From the simulation above, when set the standoff height to 4mm, the voltage to 1600v, and remove the ring extractor from the printing system, the electric field intensity is much less than it is required value, so no jet or droplet could be expected to see during the experiments. The results of this configuration are shown in the figure 5.8 (a1) to (a3), which validated the simulation result above that even after 20 seconds, no jet or droplet will be formed at the apex of the nozzle. A large drop was gradually accumulated at the nozzle tip due to the back pressure of the syringe, and this phenomenon indicated that at this condition, the electric field strength is not enough to provide enough electrostatic force to overcome the surface tension force and viscous

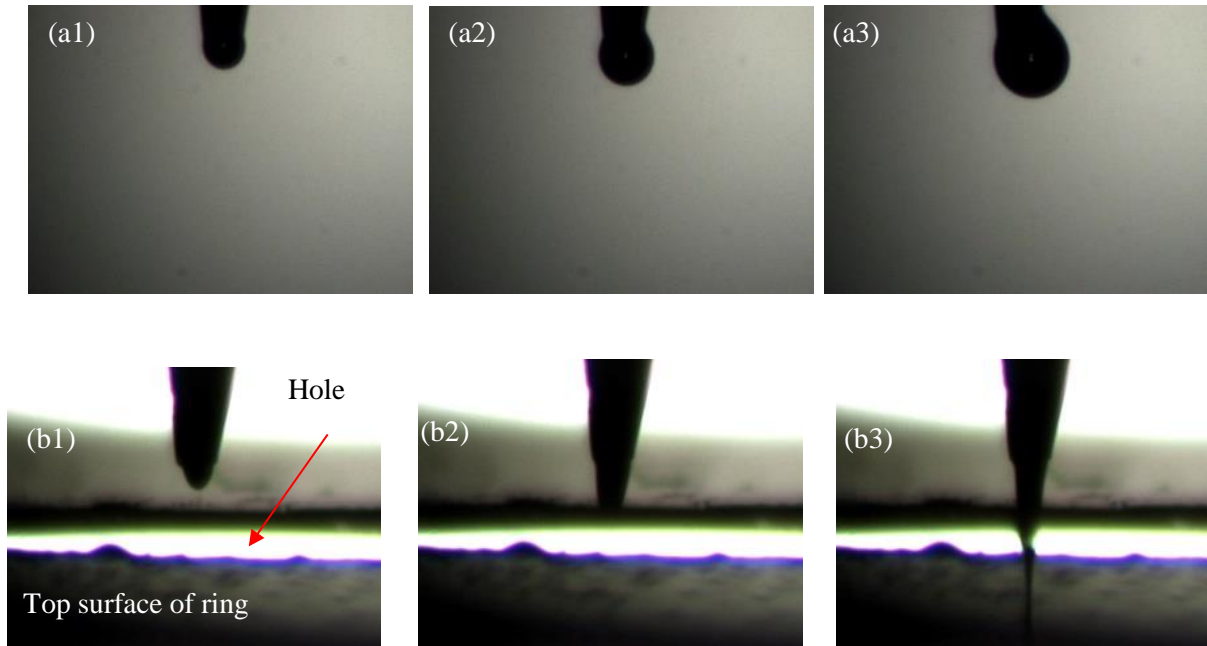


Figure 5.8 The printing behavior at the nozzle tip (a) without ring-extractor at 1s, 7s, and 20s, and (b) with ring-extractor at 1s, 3.5s, and 9s.

force to form the Taylor cone and start the EHD printing.

When replaced back the extractor and based on the simulation, a fine jet or droplet should be examined. Results in the Figure 5.8 (b1) to (b3) have confirmed the expectation, which a fine jet is observed after 9s. The fine jet is formed from the apex of the Taylor cone and go through the hole of the ring electrode before it reached to the substrate, which indicates the enough electric field intensity and the electrostatic force on the nozzle tip under this printing conditions. With a proper alignment between the nozzle tip and center of the hole, a fine stable jet could be continuously ejected from the nozzle. Compared with the printing behavior without the ring extractor, it clearly showed that the required electric field or electrostatic force comes from the ring electrode at this large nozzle to substrate distance, which proved that the dominant ground electrode changed from the substrate to the top surface of the ring extractor. When further increase the standoff height (nozzle to substrate distance) to 10mm, the EHD printing can still be

started and maintained very similar to the previous result. This result has also strongly verified that the effectiveness of the ring electrode for substrate-independent EHD printing. So we could expect when increasing the standoff distance to any large distance, the EHD printing process will be started and maintained. When decreasing the standoff distance from 4mm to 2.5mm, the printing behaviors at the nozzle tip were almost the same as that in Figure 5.8 that indicated the ring extractor is still the dominant ground electrode. This result match with the FEA models that when the nozzle-substrate distance was larger than 2.5mm, the complete electric field is less or almost no affected by the substrate and the mostly come from the ring electrode. When the standoff height is further reduced to 1.5mm, the time between starting from a Taylor cone and eject fine and stable jet from nozzle tip is reduced to 7 seconds. So at this moment, a larger electric field intensity has been acted on the meniscus to accelerate the ink flow and starting of the printing process. Because the overall electric field combines electric field between the nozzle and ring extractor and the electric field between nozzle the substrate, and the electric field between the nozzle and ring extractor does not change in this case, so the changed electric field is the field that between nozzle and substrate. Thus, under this printing condition, the substrate has some contribution to the overall electric field intensity, which also has a good match with the FEA results that with small standoff height, the substrate begins to contribute to the overall electric field strength and affect the printing behavior.

Other design parameters such as ring diameter (2mm, 3mm, 4mm, and 5mm), different tip to ring distance (200 $\mu$ m, 400 $\mu$ m, and 500 $\mu$ m) have also be tested in the experiments. When using a small ring diameter (2mm), the starting time is much less than 9 second for applying a voltage of 1600V, which indicated that the electric field intensity is increased. On the contrary, using a larger ring diameter will lead to a longer starting time, and it is also much difficult for the

system to maintain the stable jet that may be due to the reducing the electric field intensity. We have also tested the needed voltage to start the same printing process with an electric field of  $163.4 \text{ V}/\mu\text{m}$ , and the experiment is  $1500\text{V}$  when using a ring diameter of  $3\text{mm}$ , which is very close to the simulation result of  $1507\text{V}$ . When using the larger ring to nozzle distance, the starting time is also increased and on the other hand, with a small ring to nozzle distance, the starting time is reduced. All of those experiments result have a good match with the FEA model results, and this also proved that this model could be used for the ring electrode design.

#### 5.4.2 Characterization of EHD Printing with Ring Extractor

In EHD printing with the ring electrode, a required high voltage is applied between the printing nozzle and the ring extractor. If this voltage reaches a certain level, the generated electric field could provide enough electrostatic force act on the nozzle and deform the meniscus at the nozzle end into a Taylor cone. When increasing the voltage to a higher level, which the generated electrostatic force will overcome the sum of the surface tension and viscous force, eventually a jet or a droplet will be ejected from the apex of the Taylor cone and reach to the substrate.

For the study of characterization process, we have to change one parameter at each time and keep other parameters as constants. In the EHD printing, voltage is one of the most important parameters, so the first parameter that we are trying to find the relationship with printed filament is the voltage. So for other parameters, we have to use the same value for the entire test (substrate moving speed:  $16\text{mm/s}$ , standoff height:  $1.3\text{mm}$ , nozzle to ring distance:  $300\mu\text{m}$ , extractor diameter:  $4\text{mm}$ ). When gradually increased the voltage, the Taylor cone shape was gradually forming at the tip of the nozzle tip, but there is no filament ejection from the cone

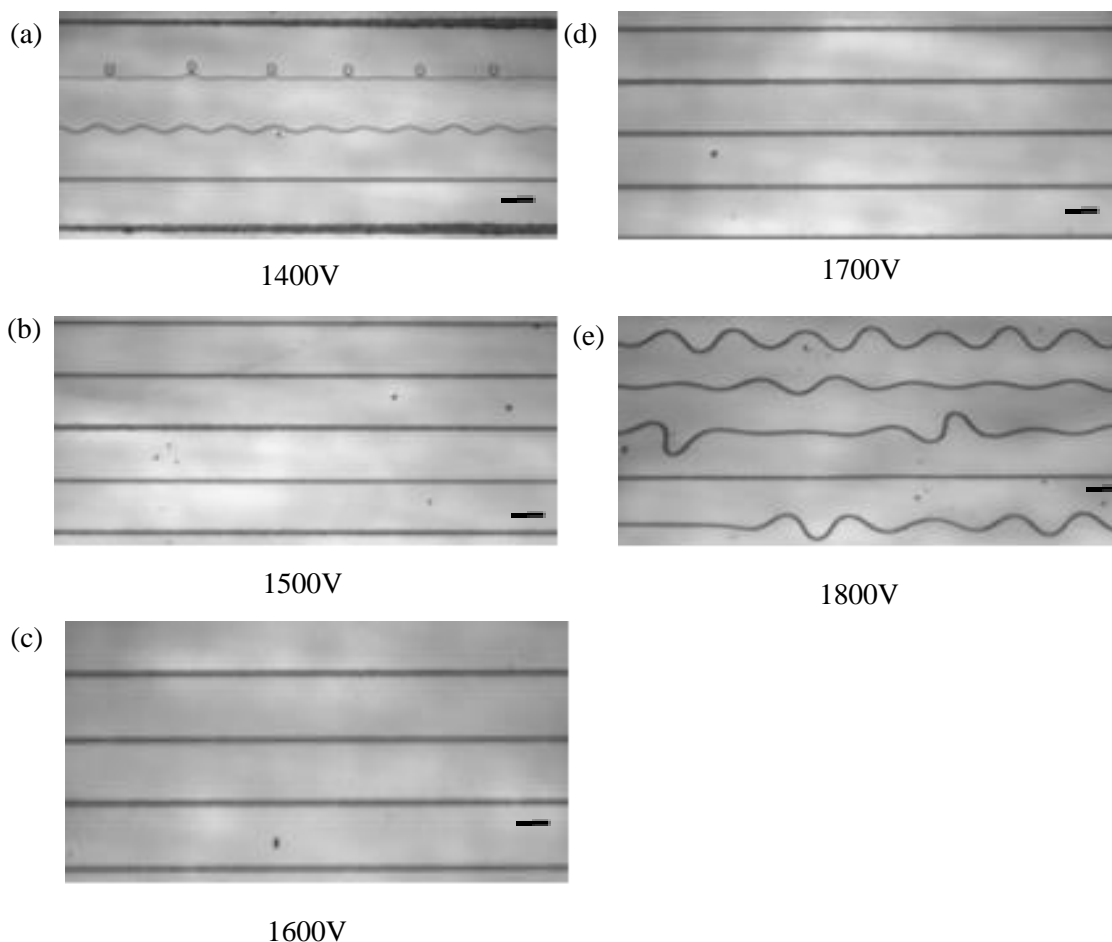


Figure 5.9 Printed filaments at different voltage from 1400v to 1800v (scale bar: 100  $\mu\text{m}$ ).

when the voltage is below 1000v, which because the electrostatic force is not large enough to overcome the entire force of surface tension and viscous force. When continuing increasing the voltage but less than 1400v, the filament started to be ejected from the cone, but the orienting process is not stable and continuous. At this condition, the electrostatic force is not large enough to overcome the other two forces to continuous drag ink out from the nozzle. So at the tip of the nozzle, the ink will collect around the nozzle, and once the total gravity of the bulk ink and electrostatic force could overcome the surface tension and viscous force, the ink will be eject to the substrate. However, once the bulk ink is gone, it will start a new cycle of accumulating ink, so the printed filament is discrete. After increasing the voltage to 1500V, a continuous straight

filament is ejected from the meniscus, which indicates a stable printing process (Figure 5.9). At this time, the tip of the Taylor cone has enough charges to provide enough electrostatic force to allow for stable jetting, and this voltage value is the minimum voltage for this system.

Continuing increasing the voltage to less than 1800V, continuous and stable straight filament could also be printed with almost same quality. When the voltage exceeds 1800V, printing processes become unstable again, and the winding filaments were printed onto the substrate, which indicated that the working voltage for this system is between 1500V and 1800V. The printing behavior for a voltage of 1800v could be explained as the large voltage will lead to a large electrostatic force that will increase the nozzle plotting speed, thus a mismatch between the ejection speed of the filament and the moving speed of the stage will result in the winging filament on the substrate.

In the EHD printing, different printing voltage will generate different nozzle plotting speed; if the plotting speed does not match with the stage moving speed, a straight line could not be obtained because the high viscosity of the printed semi-solidified PCL filaments makes it difficult to reflow on the substrate. Thus the winding filament was observed to absorb the overprinted length due to the speed mismatch. So only the plotting speed matched with the stage moving speed, the straight line may be obtained, and only under this condition, a straight cone-jet will be observed. The printed filaments under the different voltages are given in Figure 5.9. For stable jet printing, the filament diameter is about 10 to 15  $\mu\text{m}$ .

As mentioned above, different from droplet printing, in continuous filament printing, the printing speed (moving speed of the substrate) is very important to obtain stable printing. As observed from the previous experiment result, it is very critical to match the nozzle plotting speed from the nozzle and the moving speed of the substrate or the state. If the plotting speed

does not match the printing speed, the Taylor cone shape and printed filament will be adversely affected. In this study, we have also investigated the effect of the printing speed on the printing process and fabricated filaments, while the ejection speed was kept constant by using the fixed voltage of 1600v. Figure 5.10 shows the results of printed filaments under different printing speeds. When the printing speed is much smaller than 10mm/s, due to the high plotting speed, no straight filament is printed on the substrate. In order to absorb the printed material, lots of spinning filaments are observed during the printing, and the printed filament is in an irregular pattern, at this condition, the plotting speed is much faster than the stage moving speed. After increased the printing speed to a relatively high speed (10mm/s to 14mm/s), the winding

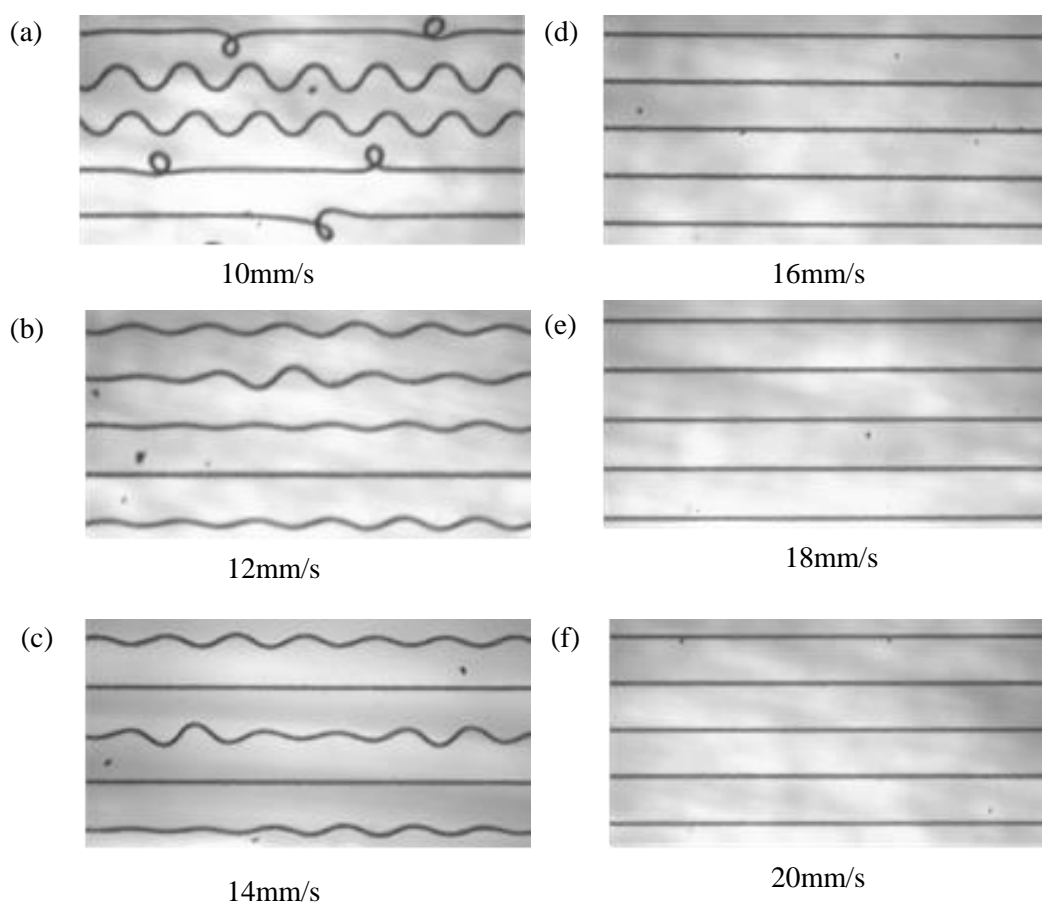


Figure 5.10 Printed filaments under different printing speed from 10mm/s to 20mm/s (Scale bar: 100  $\mu\text{m}$ )

filaments were printed, which indicated that the ejection speed is still faster than plotting speed, but the printing speed is much closer to the nozzle plotting speed. After gradually increased printing speed to 16mm/s and above, a fine straight filament was finally printed on the substrate. When the printing speed is larger than 20mm/s, due to the large mismatch between the plotting speed and printing speed, a discrete filament will be observed, because plotting speed is much smaller than the printing speed, and the electrostatic force cannot increase the flow rate to match this speed.

## **5.5 EHD 3D PRINTING WITH RING ELECTRODE**

We have successfully fabricated high aspect-of-ratio 3D structures using the EHD filament printing method with integrated ring extractor at a high standoff height. By following the programmed sequence, the 3D structures were printed layer by later. PCL filaments solidify very quickly after printed on the substrate that enables layered manufacturing of 3D structures. Compared with EHD 3D printing without the ring extractor from our previous work [12], the 3D structures printed in this work have much larger height and a much faster printing speed. The structure height in the traditional EHD printing configuration is usually between 50um to 100um due to the limitation of the nozzle-substrate distance. When the printed structure is close to the nozzle, the electric field around nozzle is distorted and causes the unstable printing condition, which makes it very difficult to control the printing speed and droplet ejection. When integrating the ring extractor into the print head, the electric field between the nozzle and the grounded ring electrode have less distortion, which can significantly reduce the negative effects from the printed 3D structures. Figure 5.11 demonstrated that 3D structures with the height of about 500 um could be printed directly with a good surface roughness, even without using any supporting materials. Although the ring extractor greatly improves the printing speed and the height of the

printed structure, the standoff height still needs to be selected carefully. With too large distance between the nozzle and the substrate, the disturbances from the printing process may degrade the precision in the placement of the filaments on the substrate, which make it difficult to control the printing process precisely.

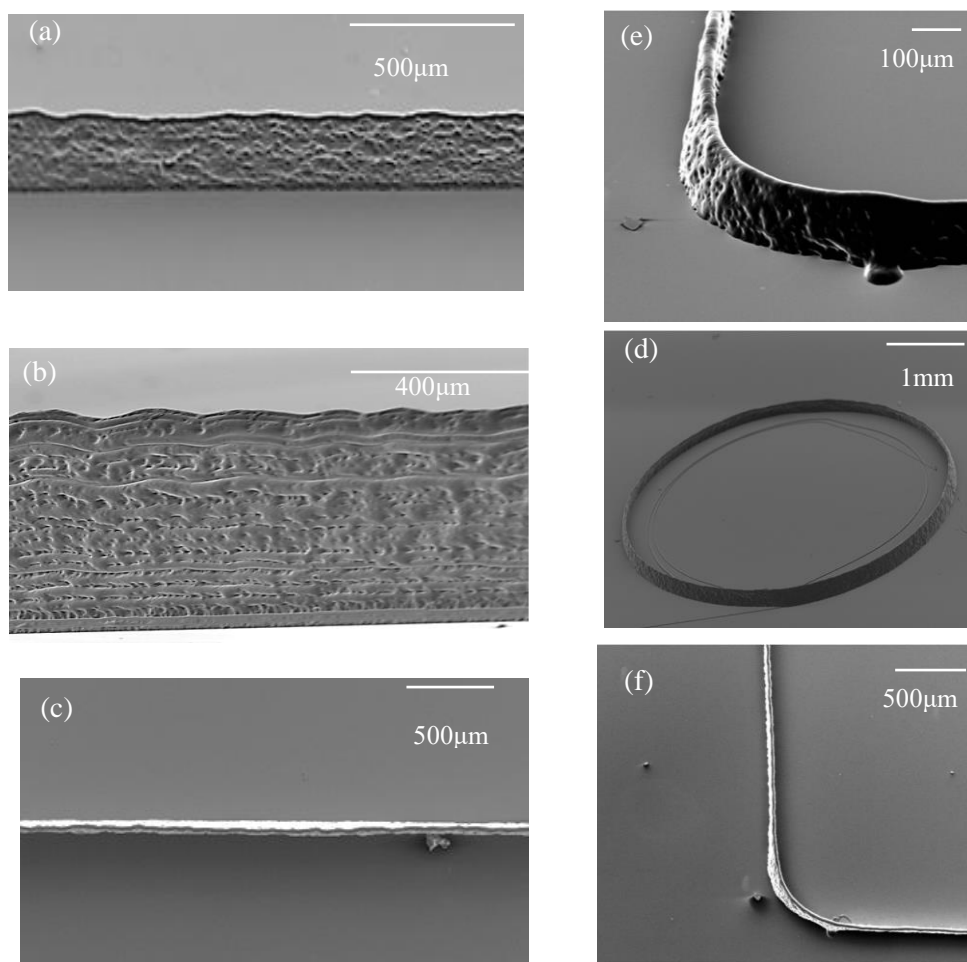


Figure 5.11 EHD filament printing of 3D microstructures. (a) Thin wall structure with a tilt angle of 45 degree. (b) Thin wall structure with a tilt angle of 80 degree. (c) Thin wall structure from top view. (d) Ring structure. (e) Square corner. (f) Top view of a square corner.

## 5. 6 CHAPTER SUMMARY

In this chapter, we presented the design, modeling, and testing of the ring extractor for EHD 3D printing, which integrates the ground electrode into the printing nozzle as a self-

working print head and overcomes the standoff height limitation in the traditional EHD printing process. Combining the supportive material with the structural material, similar to commercial fused deposition modeling process, high-resolution 3D printing could be potentially achieved using the EHD printing process. We applied an FEA method to model the electric field strength to guide the ring extractor design, so as to achieve the similar electric field strength with the printing system using the substrate as the ground electrode. The ring electrode design was verified experimentally. The results from experiments match well with results from the FEA modeling. We characterized the printing processes using the integrated ring extractor and successfully applied the designed ring extractor to print polycaprolactone (PCL) 3D structures. This printing system with integrated ring extractor gives high-resolution and high aspect of ratio 3D structures with about 10  $\mu\text{m}$  structural resolution.

## CHAPTER 6 EHD PRINTING OF ELECTRONICS WITH ADVANCED MATERIALS

Flexible and stretchable conductors are the key component for the next-generation electronics, which has gained much attention from many industries. However, current fabrication of flexible and stretchable electronics are limited in the resolution, electrical conductivity, and cost. The metallic materials are still the primary material for many industrials or applications such as aerospace, automotive and electrical devices thus high-resolution metal fabrication technology is vital for those industrials or applications. For the current metal printing technologies, high manufacturing cost or limited fabrication resolution are the main drawbacks to prevent them to be used in producing next-generation electronics. For other fabrication technologies, a mask is usually needed to produce the product, which makes the process more complicated and increase workload. In the first part of this chapter, an EHD printing process was developed for direct printing of molten metal, which allows fabricating high-resolution 3D structures and next-generation electronics. The printing process was first characterized and then optimized. With the optimal printing parameters, high-resolution 3D structures and flexible and stretchable electronics were successful printed and tested.

Besides the molten metal, metallic nanowires have shown excellent potential for the fabrication of flexible and stretchable electronics, due to its high electric conductivity, highly stretchable, and good optical transmittance. Longer nanowires can provide a higher electric conductivity according to the percolation theory and also better stretchability, which are desirable for fabrication of flexible and stretchable conductors. Longer nanowires are also good for fabrication of transparent devices due to the good balance between the electric conductivity and optical transmittance. Printing technology provides a large-scale, cost-effective fabrication for electronic devices. Most of the existing methods for metal nanowires fabrication are based on

solution coating or deposition. However, most of those methods have limitations on the resolution and electric conductivity. Moreover, mostly a mask has to be used during the process. Inkjet printing has already demonstrated to be used for electronic device fabrication. However, it is very difficult to maintain the structural integrity of the nanowires due to the nozzle clogging. To reduce the nozzle clogging, based on the “rule of thumb,” the particles size in the ink is suggested not to exceed 1/100 time of the nozzle size, which has limited its printing resolution. In this chapter, we have developed an EHD printing process, which can provide high-resolution printing for silver nanowire ink. With this technology, AgNW patterns are printed onto a variety of substrates, and the printed samples are characterized under the bending and stretching test.

## 6.1 HIGH-RESOLUTION DIRECT EHD METAL PRINTING OF ELECTRONICS

### 6.1.1 Printing System and Printing Material

The EHD printing system that shows in Figure 6.1 includes four different subsystems: a three-axis (XYZ) precision moving stage, a high voltage power supply, a thermal control system, and a pneumatic dispersion system. The precision moving state have accuracy and repeatability of about 100nm. The voltage supply can provide a maximum voltage of 10KV. The thermal

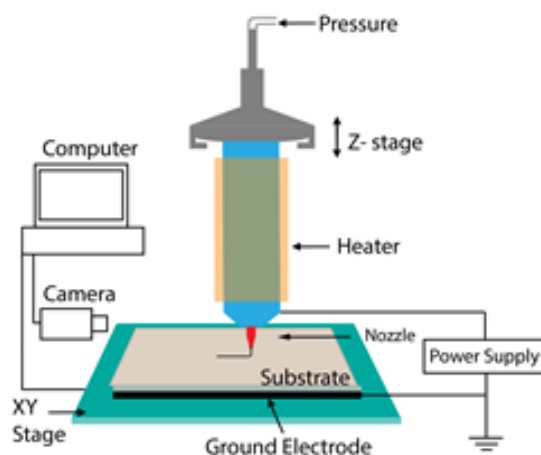


Figure 6.1 Schematic of EHD printing system

control system includes a heating rope, a thermocouple, and a proportional-integral-derivative (PID) controller, which can provide a maximum heating temperature to 900 °F with a resolution of 1 °F. The pneumatic dispersion system can provide the required back pressure (0.1 psi in metal printing) by a precision pressure regulator to help the ink flow to the nozzle. The printing nozzle used in the experiment was purchased from Subrex, which has an inner diameter of 160 $\mu$ m and the outer diameter of 250 $\mu$ m. The nozzle will fix to the syringe by a precision hub (purchase from Subrex), and connected with a thermocouple and the positive voltage, and the ground electrode will be placed under the substrate. The heating rope was wrapped around the nozzle and syringe to ensure a good heating condition at both nozzle and syringe, and the heating temperature was set to 347 °F for Field's metal and Wood's metal and 572 °F for solder to achieve a good ink flowability. A high-resolution camera was used to observe the printing process and take pictures.

Field's metal (32.5% bismuth, 51% indium, 16.5% tin), Wood's metal (50% bismuth, 26.7% lead, 13.3% tin, and 10% cadmium), and solder (48% tin, 32% bismuth, 20% lead) have been selected and used in the experiment. The melting point for those three metals are about 62 °C, 70 °C, and 160 °C. Because the Field's metal is a lead-free material, which is nontoxic to human, most of the patterns will be printed using this material unless otherwise stated. The material was first loaded into syringe and heated to the desired temperature. The printing process will begin five minutes after the temperature indicator reaches to the setting point to ensure the material is completely melted. All the printed filaments or and patterns will be inspected under an optical microscope and Scanning Electron Microscope (SEM).

### 6.1.2 EHD Metal Printing Process and Characterization

To demonstrate the advantages of using EHD technology to directly print molten metal, a pneumatic extrusion-based printing was first performed, and the results from those experiments would be used to compare with results getting from EHD printing. The nozzle has the same size as it used in EHD printing was also used for the pneumatic extrusion-based printing.

In this extrusion-based printing, applied pressure will be increased very slowly to help us to observe the changing of the printing behavior. When gradually increasing the pressure, the ink starts to collect around the nozzle and wait to be ejected from the nozzle. However, due to the large surface tension of this molten metal, a droplet will be formed around the nozzle before it

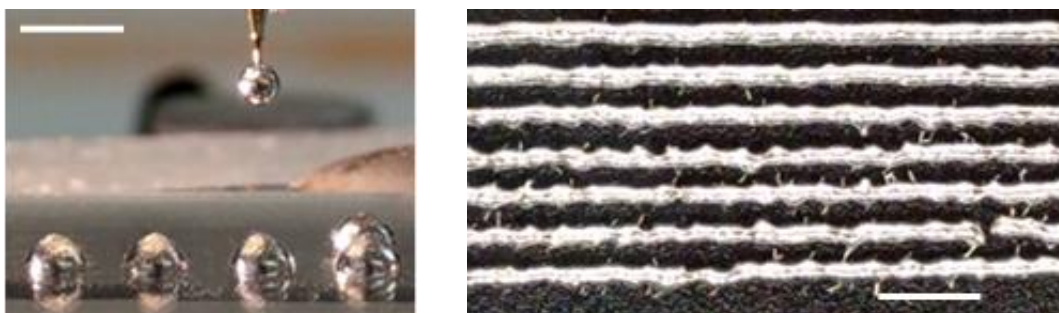


Figure 6.2 (a) large droplet of molten metal ink extruded under a pressure of 5 psi at the nozzle tip. (b) Optical image of the pneumatically extruded metal filaments at printing speed of 20, 25, 30, 35, 40, 45, 50mm/s respectively from top to bottom with a constant pressure of 10 psi. Scale bar: 5mm

detaches from the nozzle. The size of the droplet continues to grow when the pressure is gradually increased and detaches from the nozzle to form a bulk drop. Figure 6.2 (a) shows the large droplet formed around the nozzle and the final bulk drop on the substrate. It clearly shows that the size of the printed droplet is in the millimeter scale, which is much larger than the nozzle size. Continuing increasing the pressure, the printing frequency will increase too. However, the size of the droplet did not change much and still in millimeter scale. After further increasing the pressure to a certain level, which is 10psi in the experiment, stream jet will form during the

printing with a much higher jetting speed when compared with our previous printing result. To achieve a uniform printed line and avoid distortion (breaking line, wave line, etc.), the moving speed of the motion stage has to be selected carefully to match with the printing speed. The first two lines from the top of Figure 6.2 (b) shows the printed line with a match moving speed of the stage. The extruded lines have diameters of few millimeters that is more than twenty times larger than the nozzle size. Bottom lines of the Figure 6.2 (b) shows the printed lines on a high moving speed stages. Breaking lines or rough edge lines are observed from the results, although the line diameter is reduced to submillimeter. The printed lines with that quality cannot be used for fabrication of 2D or 3D feature or other applications, which indicated that the extrusion-based molten metal printing technology cannot provide high resolution printing without scarifying feature's quality. To achieve both high quality and high resolution printing of molten metal, EHD printing technology is applied to this study. In the EHD printing, as applying the high voltage between the nozzle and ground electrode, an electrostatic force will form around the ink to form a Taylor-cone. From the EHD printing mechanism [149], the flow rate of the ink during

the EHD printing can be express by,  $Q \approx \frac{\pi d_N^4}{128\mu L} (\Delta P + \frac{1}{2} \varepsilon_0 E^2 - \frac{4\gamma}{d_N})$ , where Q is the flow rate,

$\Delta P$  is the pressure drop,  $\mu$  is the viscosity of the ink,  $d_N$  and  $L$  are the diameter and length of the nozzle,  $\varepsilon_0$  is the permittivity of free space,  $\gamma$  is the surface tension of the air-ink interface, and  $E$  is the magnitude of the electric field. The electric stress  $E$  can be approximately expressed by

$E = 4V_0 / [d_N \ln(8H / d_N)]$ , where  $H$  is the standoff height. When the sum of the pressure force

and electrostatic force overcome the surface tension,  $\Delta P + \frac{1}{2} \varepsilon_0 E^2 - \frac{4\gamma}{d_N} > 0$ , which indicates ink

will flow out from nozzle and a jet or a droplet will be generated and ejected from nozzle, which usually has a much smaller size than the nozzle size. The required initiation voltage can be

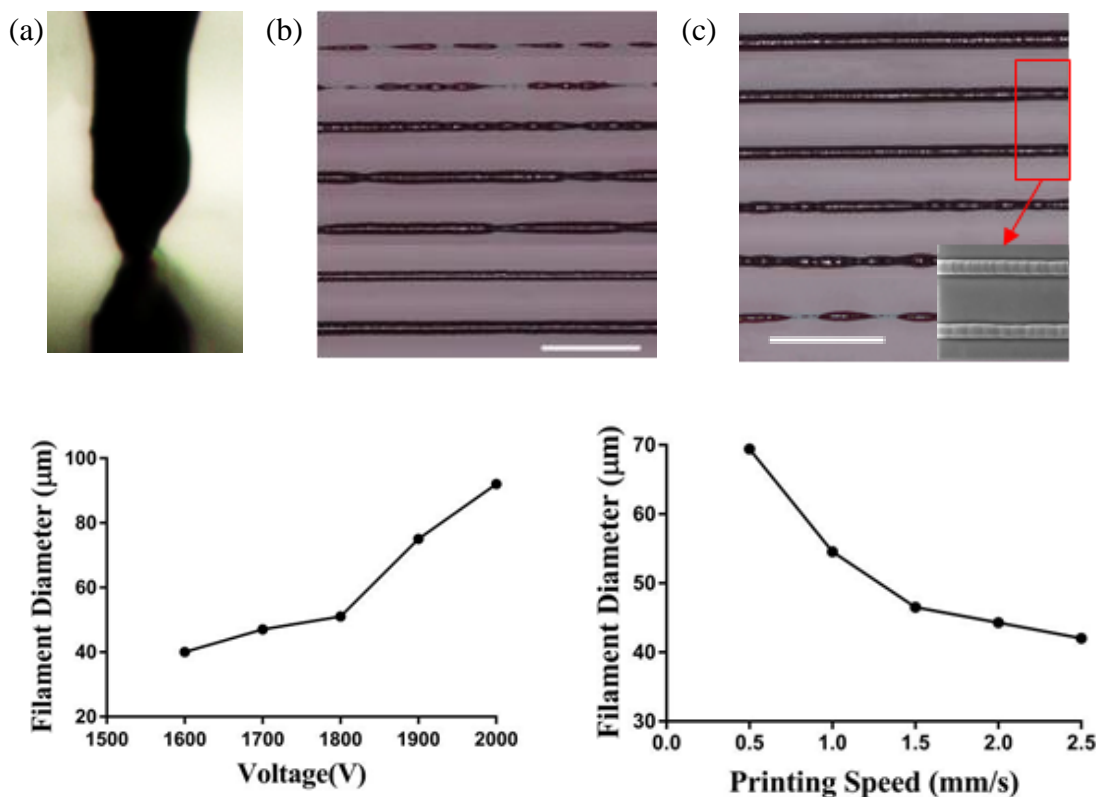


Figure 6.3 (a) EHD printing behavior around the nozzle (b) EHD printed metallic filaments on glass at different voltage of 500, 1500, 1600, 1700, 1800, 1900, 2000V respectively from top to bottom. (c) Printed metallic filaments on glass substrate at printing speeds of 0.5, 1, 1.5, 2, 3, 4 mm/s respectively from top to bottom (d) Line width of the EHD printed filaments as a function of the printing voltage at constant printing speed of 0.5 mm/s. (e) Line width of the EHD printed filaments as a function of the printing speed at a constant voltage of 1900V. Scale bar: 500  $\mu\text{m}$ .

calculated, which is about 600V. In this work, due to the larger surface tension of the molten metal ink, the ejected ink will form a continuous jet instead of separate droplets. The Figure 6.3 (a) shows the EHD printing behavior at the nozzle. It clearly shows that, in the EHD printing, a cone is formed at the end of the nozzle and the ink ejected from the apex of the cone onto the substrate. Contrary to the feature size around the nozzle in extrusion-based printing, the produced feature size in EHD printing is much smaller than the nozzle size, which demonstrated that EHD printing can overcome the nozzle size limitation and provide high-resolution printing. Applied voltage, the stage moving speed, and standoff distance are the most important printing

parameters in EHD molten metal printing and all of them have strong effects on the printing quality and resolution. However, the mainly effect of changing standoff distance is changing the electric field strength that is similar to the effect of changing voltage, so in our work, a constant standoff distance was used. To find the best printing parameters for this printing system, a series test were performed with different voltage and different printing speed. When the voltage is larger enough that can overcome the surface tension and viscous force of the ink, a filament will be ejected from the nozzle onto the substrate. Figure 6.3 (b) shows the printed filament with a constant printing speed on a glass substrate under different voltages (500V, 1500V, 1600V, 1700V, 1800V, 1900V, and 2000V, respectively, from top to bottom.) When the applied voltage is in a relatively low value (500 – 1500V), the generated electrostatic force doesn't strong enough and lead to a very low ink flow rate. Since the constant printing speed is higher than the ink flow rate, some discontinuous metal lines was printed on the substrate. When increase the voltage to 1600V, continuous metal lines can be observed on the substrate. However, the printed lines have rough edges due to the insufficient of ink flow rate. Further increase the voltage, both the edge quality and continuity are improving, but still lack of uniformity. The uniform filaments with a smooth edge can be printed when increased the voltage to 1900V, which indicated that the ink flow rate is matching with the stage moving speed, thus high quality lines could be obtained. Continuing increasing the voltage, uniform lines can be also printed on the substrate, but the diameter of the lines are larger than the diameter of the lines that printed with a applied voltage of 1900V that can be explained as higher voltage will increase the ink flow rate, which exceeds the stage moving speed, thus the printed ink tends to accumulate around the nozzle and that will lead to a larger diameter size.

As mentioned, the stage moving speed also known as printing speed is another important parameter for this EHD molten metal printing, because a good match between printing speed and ink flow rate is important for producing high-quality features. Figure 6.3 (c) shows the printed result under different printing speed (0.5, 1, 1.5, 2, 3, 4,  $\text{mm}\cdot\text{s}^{-1}$ ) with a constant applied voltage of 1900V, and the measured result of the diameter of printed line is shown in Figure 6.3 (e). From the result, when increasing the printing speed, the diameter of the line is decreasing, and when the printing speed is too high, no continuous lines will be found on the substrate. The reason is when using a constant applied voltage, the ink flow rate will also be a constant value. When the printing speed is slower than the flow rate, larger size filament will be produced due to the ink accumulation or collection around the nozzle. When the printing speed is perfect match with ink flow rate, high-quality lines with high-resolution will be printed on the substrate. However, when this printing speed is too high, the uniformity of the printed filaments was degraded. Based on the observation, the best high-resolution and quality filament can be obtained when the printing speed is set to  $1.5 \text{ mm}\cdot\text{s}^{-1}$ , and the line width is about  $45 \mu\text{m}$ , which is much smaller than the size that using extrusion based printing method.

Besides printing Field's metal on a glass substrate, EHD printing is also capable of printing a variant of other molten metal inks onto different substrates. To demonstrate the printing flexibility of EHD technology, we have selected three different material, which includes Field's metal, Wood's metal, and solder; and four different substrates that include glass, PDMS (polydimethylsiloxane) film, PET (polyethylene terephthalate) film, and photo paper. The properties of those three metals have already mentioned in the previous section. Due to the different material properties and substrate properties, the printing temperature, printing speed, printing voltage, and standoff distance will be different, which can be explained that different ink

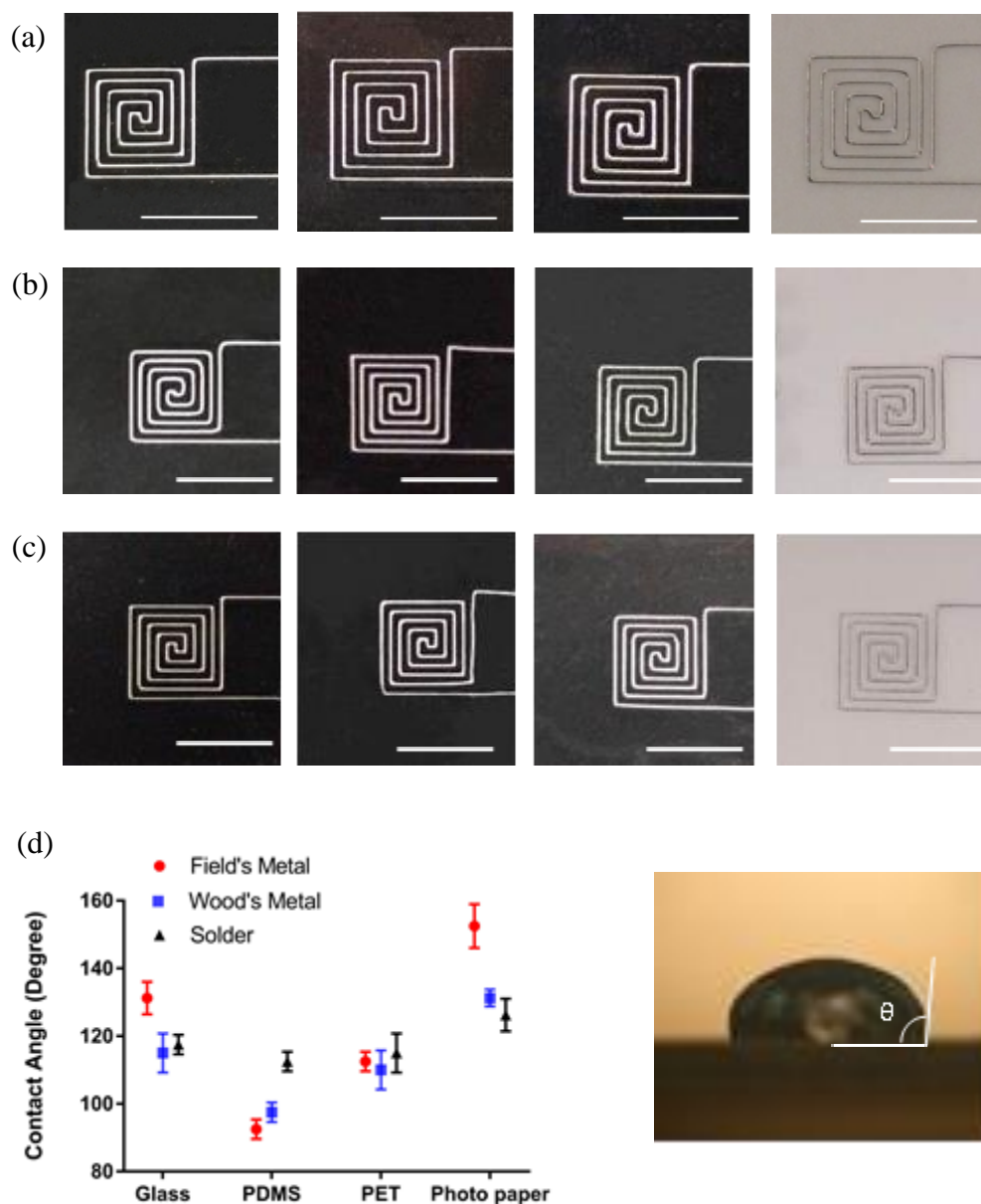


Figure 6.4 (a) to (c) EHD printed patterns from Field's metal, Wood's metal and solder on different substrates (from left to right: microscope glass slide, PDMS, PET, photo paper) (d) Contact angle for different materials on different substrates. (e) Contact angle between Field's metal and PDMS substrate. Scale bar: 5mm

materials and substrates could affect the generated overall electrostatic field strength around the nozzle. However, the effect of the printing speed and applied voltage on the printing system is similar to our previous study, so only smaller changes needed for printing different materials onto different substrates. Figure 6.4 (a) to (c) shows the patterns of printing three materials onto

four substrates. Obviously, the substrate properties, especially the wettability of the molten metal inks on different substrates, will affect the adhesion and printing performance of each ink on the substrates. To have a better understanding of the wettability of different inks on different substrates, we have studied the surface interaction between inks and substrates by measuring the contact angle between the metal inks and the four different substrates. An image of the slow extruded droplet on the substrate is taken by a high-resolution camera, and the contact angle between three metal inks and four substrates were measured by evaluating the drop image on these substrates, as shown in Figure 6.4 (d) and (e). Among these four substrates, PDMS has the smallest contact angles with all three metal inks, which indicates the good wettability and adhesion between PDMS and three molten metal inks. The contact angles between photo paper and three metal inks were greatest, indicating poor wettability, which we have to take more cares on printing speed during the printing to prevent breaking line. The results of the contact angles reflected the adhesion of the metal inks on each substrate. The metallic inks had stronger adhesion to the PDMS substrate and had weaker adhesion to photo paper. The metallic filaments cannot be separated from the PDMS substrate without breaking the filament but can be peeled off relatively easily from the photo paper.

### 6.1.3 Direct Molten Metal Printing of 2D and 3D Features

To demonstrate the EHD printing capability on 2D and 3D, a series of different 2D and 3D features have been designed and printed successfully. Based on the characterization process, an optimal printing parameter set is selected for the upcoming experiments. All the features are designed in CAD software and then converted into g-code program files, and those files will be sent to the printing system control software. For 2D patterns, changing the value of the printing parameters are not required, but for 3D structures printing, the value of printing parameters need

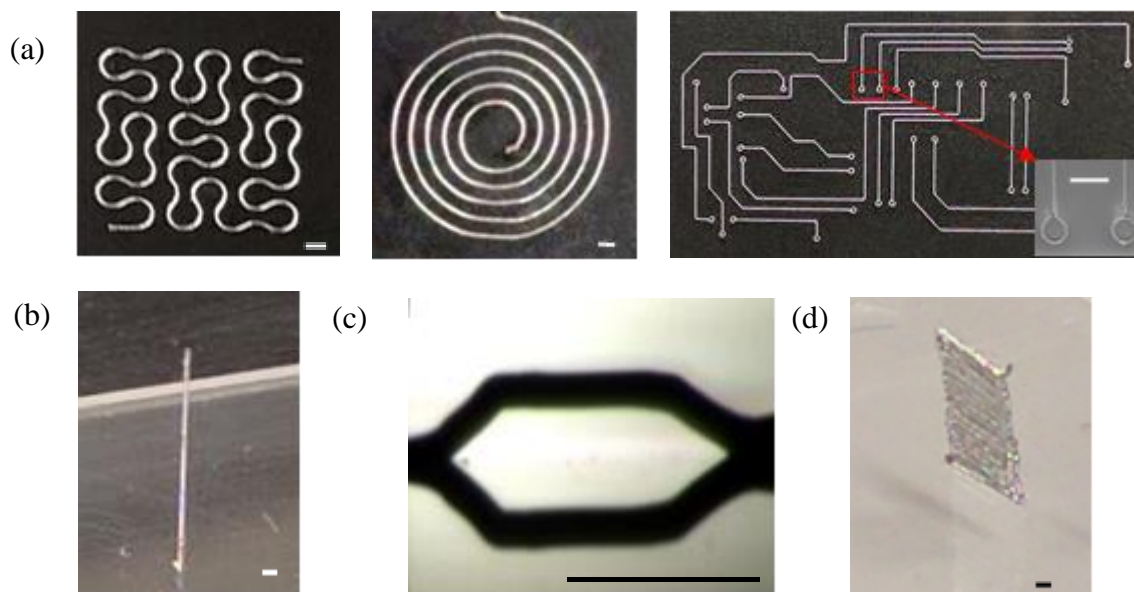


Figure 6.5 (a) EHD printed high-resolution 2D patterns (b) Vertical metal wire (c) Metal bridge structure. (d) Thin wall. Scale bar: 500 $\mu$ m

to be changed during the printing, which is because when printing high structures, z-axis has to be lifted during the printing, which will reduce the overall electric field strength. So continuing increasing the voltage has to be a necessary procedure for 3D printing. Moreover, the setting temperature for 3D printing has also very important, because if the temperature is too high, the ejected ink will not get solidified quickly and will also re-melt the printed structures that will damage the structures. With carefully selecting all printing parameters, high-resolution 2D and 3D features have been printed, which shows in Figure 6.5. The direct printed 2D patterns have very smooth line edge and uniform line width, which is around 50  $\mu$ m. The resistance of the printed patterns and cross-section of the printed filament are measured using multimeter and microscope, and the resistivity of the pattern can be calculated, which is about 0.6  $\mu\Omega\cdot$ m. This value indicates that the printed patterns have a good conductivity and this printing technology has good potential to be used in the direct fabrication of conductors or electronics. Figure 6.5 (b) shows the high aspect of ratio metal pillar that direct printed on the vertical direction that

demonstrates the EHD direct vertical printing capability and has potential to be used for fabrication of other free-standing structures. The printed pillar has a diameter of about 90  $\mu\text{m}$  with a height of about 10mm that gives an aspect-ratio as high as 100. Figure 6.5 (c) shows a bridging structure that also direct printed using EHD approach. Direct fabricating of bridging structures will provide an easy way for wire bonding, and high quality interconnects in chipboard manufacturing and electronics manufacturing when compared with traditional manufacturing technologies. Besides direct printing on vertical direction, we have also demonstrated to produce high-resolution 3D structure layer by layer. Figure 6.5 (d) shows a printed thin wall by carefully selecting the overlap and repeating the printing sequences layer and layer. The printed structure has a wall thickness of about 100  $\mu\text{m}$  and a height of about 3mm. Compared with the best feature resolution (X/Y resolution of 0.012–0.016 inch or 305– 406  $\mu\text{m}$ ) from the start-of-art 3D metal printing machines, such as Stratasys Direct, Inc., this EHD metal printing technology offer much better printing resolution capabilities.

#### 6.1.4 Direct Fabrication of Flexible and Stretchable Conductors

Since we have already demonstrated the capability of printing high-resolution 2D and 3D structures, EHD printing of molten metal has the potential for producing electronics. In this section, we will focus on fabrication of flexible and stretchable conductors using Field's metal. As a soft alloy with a low melting point, the printed microscale patterns from Field's metal are capable of being used as high-conductivity conductive paths with excellent flexibility and stretchability. Several different patterns have designed and printed for the flexibility and stretchability test. The substrate used for the two tests is PDMS. A PDMS film is prepared using Sylgard 184 (Dow Corning) with a ratio of 10:1 between the base and the curing agent. The PDMS is thermally cured under 65 °C for 10 hours to form cross-linked solid PMDS film with a

thickness of about 1mm on the glass slide. Once the pattern is printed on the PDMS substrate, a peel-off process has to be performed to separate the PDMS film from glass surface. To avoid the damaging to the samples during the peel-off process, the PDMS film has to keep flat during the whole process. Once the PDMS film with printed patterns on it has been separated from glass, liquid metal and thin wires are used to connect the pattern with other devices, such as LED light, battery, multimeter, and etc. Another layer of PDMS film with a thickness of 0.5mm is coated to secure the pattern inside the PDMS, and the samples will be ready to use for different tests.

For the flexibility test, a Christmas tree pattern is designed and printed onto the PDMS. Figure 6.6 (a) shows the EHD printed conductor with Christmas tree pattern that connects a battery to light a LED, and Figure 6.6 (b) shows that the LED keep lighting when the pattern is under bending state. To further evaluate the conductivity of the printed conductors under different bending conditions, bending tests with different bending diameter ranging from 19mm to 5mm has been performed. The pattern is placed and fixed on a fixture, which can provide a bending diameter from infinity to 3mm. The pattern is connected with an LCR meter, and the resistance under different bending diameter can be directly displayed on the LCR meter. Figure 6.6 (c) shows the result of the resistance of the pattern under different bending diameter. When

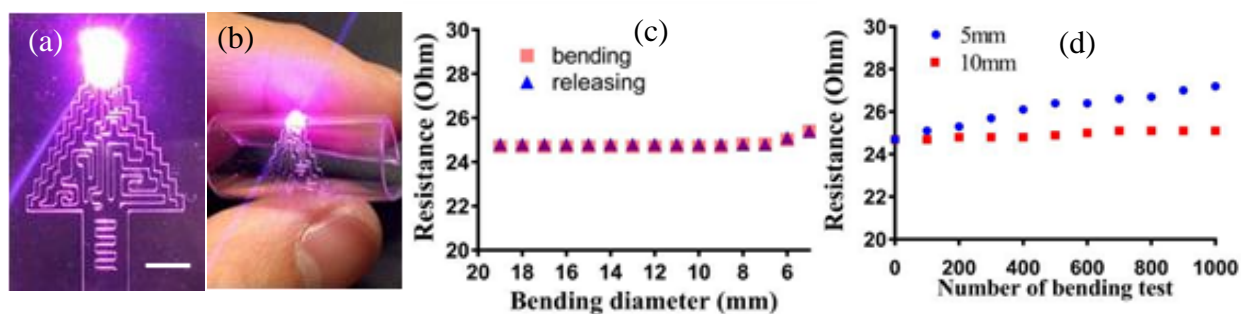


Figure 6.6 (a) EHD printed conductor on PDMS with a Christmas tree pattern that connected a battery to light a LED (Sale bar: 500 $\mu$ m). (b) The conductor remained conductive at the bending state. (c) Resistance of the Christmas tree conductor as a function of bending diameter. (d) Resistance of the Christmas tree conductor as a function of the number of bending tests at the bending diameter of 10mm and 5mm.

the bending diameter equals or larger than 7mm, the resistance of the conductive trace almost keeps at a constant level. When the bending diameter is reduced to 5mm, the resistance increased from 24.7 to 25.4  $\Omega$ , which is only about 2.8% increasing in resistance. The reason for the resistance increasing may be due to the shape deformation and elongation of the printed lines when bending. During the bending, the strain will reduce the cross-section area and elongate the overall conductive path length. Moreover, fatigue tests (i.e., repetitive bending test) are performed to evaluate the durability of the printed metallic conductor. Two fatigue tests with different bending diameters of 5mm and 10mm have been conducted to study the electrical behavior under 1000 times of bending. For the bending diameter of 10mm, the resistance of the conductor barely unchanged after 1000 bending cycles. Even for a rigorous bending test with the bending diameter of 5mm, the conductor remained conductive with its resistance gradually changed from 24.8  $\Omega$  to 27.2  $\Omega$ , when performing the bending cycle for 1000 times. The test result is shown in Figure 6.6 (d). The change of the resistance came from the geometry change of the conductor when strongly bent. The strain on the conductor reduced the cross-section area and increased the length of the conductor. As a result, the resistance of the conductor increased. With a bending diameter of 10mm, only small strain incurred and the conductive metallic path is only in the elastic deformation so that the conductor can recover to the original shape and the resistance returns to the original value when the strain is released. However, large strain such as during the bending process with a bending diameter of 5mm can plastically deform the conductor, which results in the increased resistance even after the bending cycles, as observed in Figure 6.6 (d). The results from these bending tests indicated the good flexibility of the printed metallic conductors.

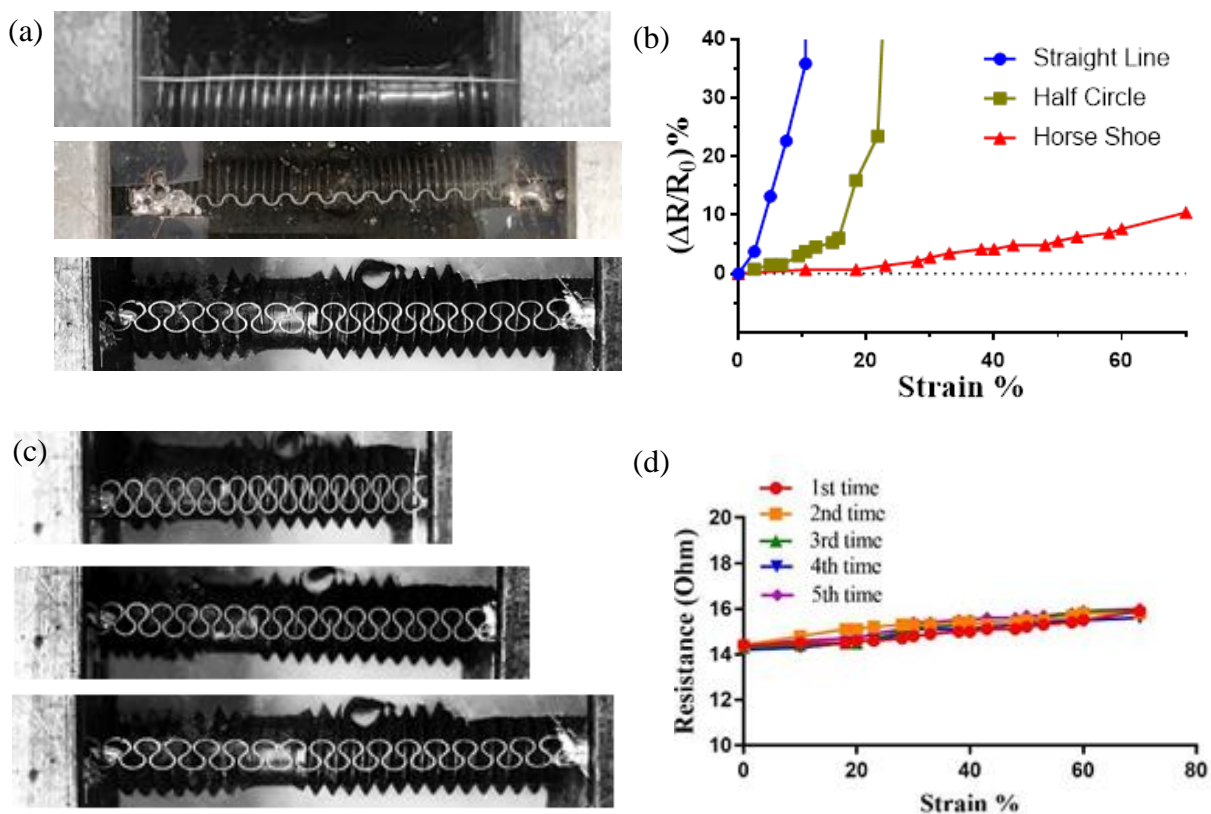


Figure 6.7 (a) Optical image of printed different designed conductor pattern (from top to bottom: a straight-line, Half-circle, and horseshoe.) (b) Resistance changes as a function of tensile strain (0-70%) for three different designed pattern. (c) Optical image of a metallic conductor with horseshoe pattern under tensile strains of 0%, 25%, 50%. (d) Resistance as a function of tensile strain (0-70%) for the metallic conductor from the first to fifth stretching cycles.

Stretchability is the other important property for flexible and stretchable electronics. The previous study by Gonzalez's group [150] showed that the sample with a horseshoe pattern provided better stretching performance when compared with other pattern designs, such as straight line and half circle patterns. To study the stretchability of the EHD printed conductor, we have also used three different in-plane patterns for the stretchability test. The three different patterns include straight line, half circle, and horseshoe pattern. The designed pattern is printed on the PDMS film, and another layer of PDMS is coated to encapsulate the printed feature after proper wiring the conductor with other testing equipment. The final sample is clamped on a stretch table, from which the strain was applied continuously, as shown in the Figure 6.7 (a).

The resistance of the sample at different strain levels is measured by a multimeter, and for each design, the test is repeated for 5 times. As observed in Figure 6.7 (b), the straight metallic conductor has a low stretching performance with the maximum tensile strain of about 10% before failure and which is impossible to improve due to its material property. For half cycle pattern, it allows stretching to about 20% before failure. The reason for the improving of the stretchability is that the shape of the half cycle pattern will have a change during the stretching, which can absorb some of the strain in the stretching, and that will improve its stretchability. From Figure 6.7 (b), the conductor with a chain of multiple horseshoes pattern demonstrated an even better stretchability, because this design allows the pattern to have pattern shape change to maximum absorbing the strain that acts on the conductive path, so the strain on the conductive path reduced. Even when a very large tensile strain of 70% was applied to the sample, the conductor remained conductive with only small change in its resistance, from  $14.2\Omega$  to  $16.0\Omega$  which is about only 12% changes. This slightly increased resistance also came from the deformation in the conductor that changed the length and the cross-section area of the conductor. Upon release of the strain, the resistance was almost fully recovered and decreased back to  $14.2\Omega$  when the PDMS was fully released. Moreover, repeated stretching/releasing cycle test in the strain range of 0–70% are performed, and similar response in the resistance was observed. Figure 6.7 (d) shows the resistance from the first to the fifth stretching cycles. A stable and repeatable resistance was achieved throughout multiple stretching/releasing cycles, which demonstrated a good repeatability on stretching and releasing process for this EHD printed conductor.

As a low melting point metal alloy, the Field's metal has a low melting temperature of  $60\text{ }^{\circ}\text{C}$ . This low temperature is harmless to most of the polymeric substrate used in flexible and stretchable electronics, so the printed metallic lines can be heated to liquid phase without damage

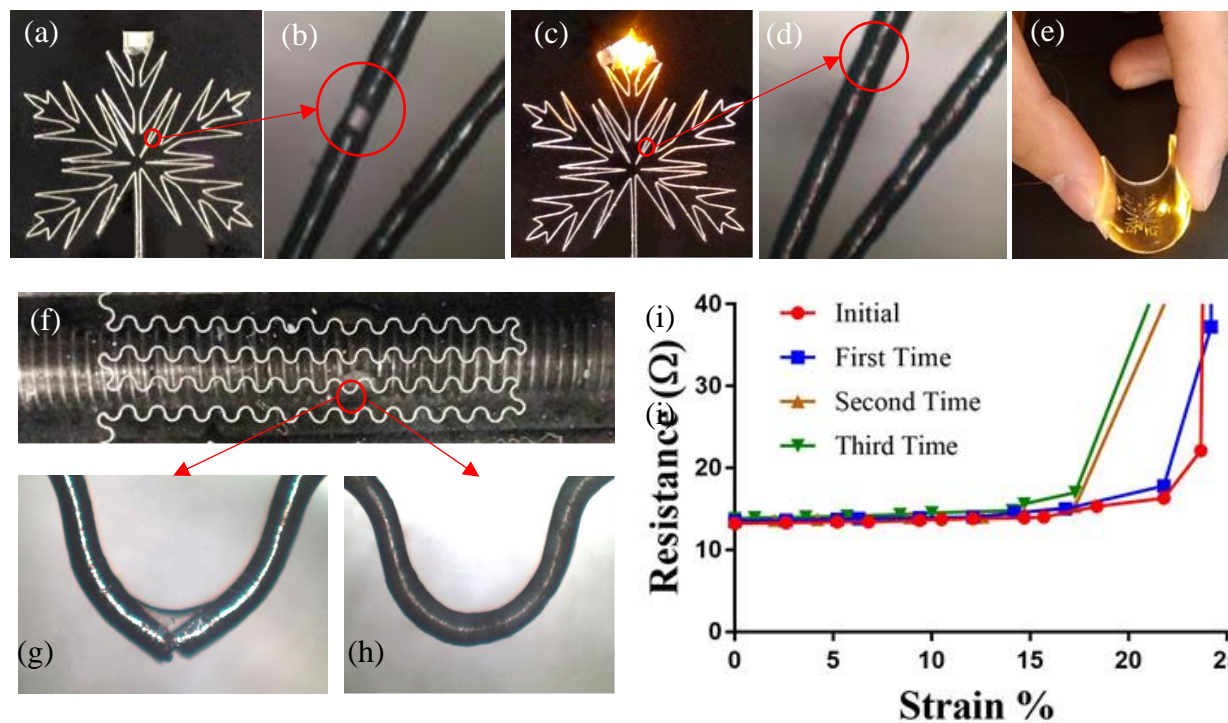


Figure 6.8 (a) and (b) Printed feature before and after healing process (c) Optical image of break point in the printed feature before and after healing. (e) Bended feature after healing process (f) Horseshoe pattern on stretching test table (g) and (h) optical image of break point in half circle pattern before and after healing (i) Resistance as function of tensile strain in the initial to third time of healing process.

to the substrate. Here, we have studied the self-healing capability of the printed metallic conductor, which can recover from the failure by a simple heat treatment of the sample above its eutectic temperature of the metal ink. Once the printed conductor was encapsulated in the PDMS film, heat treatment melted the metal and reconnected the metallic pattern to fix the failure of the conductor. In this study, we have designed a maple leaf pattern for the test. Only straight lines have been used in the pattern since the straight line can be easily broken when compared with other two patterns that we have discussed in the stretching test. Figure 6.8 (a) shows a printed maple leaf pattern as the conductive paths to power a LED. To test the self-healing ability of the sample, we intentionally applied a large tensile strain to the PDMS substrate to allow the maple leaf pattern to break the connection. One of the breakpoints was shown and highlighted in Figure

6.8 (b). With such failure in the conductive path, clearly the LED was off. Then the PDMS film was placed on a hotplate and heated at a temperature of 75°C for two minutes to ensure the printed pattern is in the liquid phase. To help the molten metal ink flow during the PDMS, a slight finger pressure was applied to the broken point and to allow the liquid ink across the gap. This material also conductive under the liquid phase, so after such healing procedure, the circuit recovered from the failure, and the LED was lighted again without letting the sample to cool down to room temperature. The broken gap in the conductor was connected together, and the failure was healed, as shown in Figure 6.8 (c). The healed sample remained conductive and worked well when it was bent as shown in Figure 6.8 (e).

A number of stretching and healing tests were performed to evaluate the effect of the healing on the stretching capability of the printed metallic conductor. The PDMS substrate with printed conductor was fixed on a stretching table after wiring with a multimeter and stretched to failure. Once the sample is broken, it will be released from stretching table and place on the hotplate for heat-treatment. These tests were repeated multiple times to study the stretching behavior after each healing operation. The conductor with the horseshoe pattern (Figure 6.7 (d)) had an excellent stretchability and was difficult to break, even at the maximum strain that can be provided by the stretching table used in this study. In order to perform both stretching and healing tests, we selected a pattern that provided less stretchability than the horseshoes pattern, so that we can break the conductor easily with relatively small strain; but also has stretchability better than straight line, which can provide better observation of the result.

Previous work by Gonzalez's group showed that the half-circle pattern withstood less strain than the horseshoe pattern, which is the ideal pattern for this study. In Figure 6.8 (f), a series of half-circle patterns were printed on the PDMS film and then covered by the other layer

of PDMS. The resistance of the pattern under different strain level is recorded until a failure occurred. For the half-cycle pattern conductor, the conductor was broken after applying a tensile strain of about 22%. The released sample was observed by a microscope to find the failure point in the circuit. Then the healing process was performed to heal the failure point in the circuit, and the stretching test was repeated. Figure 6.1.4.3 (g) and (h) shows the location of one connection failure point in the conductor before and after the healing process. Clearly, the connection of the conductor was recovered, and a uniform diameter of the conductive path was observed after healing. To study the healing cycle effect on the electrical property of the conductor, a fatigue test has been conducted. Figure 6.8 (i) shows the test results of the resistance of the conductor at different stretching cycles after healing from the failure that was produced by the previous stretching cycle. When performing the stretching-failure-healing process multiple times, the resulting resistance responses of the printed conductor under the applied strain were very similar, which demonstrated a good repeatability of this printed conductors. Moreover, within the strain range of 0-15%, a stable resistance was achieved even though the sample had undergone multiple stretching-failure-healing processes, which demonstrated excellent self-healing capability of the printed metallic conductor.

With high-resolution direct molten metal patterning capability from EHD printing, a high-resolution and high-density touch sensor array was directly fabricated with the schematic structure shown in Figure 6.9 (a). For this projected capacitive touch sensor design, a capacitor was inherently formed by the row trace and column trace at each intersection of the grid. The designed touch sensor consists of 20 row traces and 20 column traces, which provide a 400 intersect points. The sensing mechanism is based on disturbing the fringing electric field by a finger or touching tip. When the fringing electric field of the sensor is disturbed by a finger or

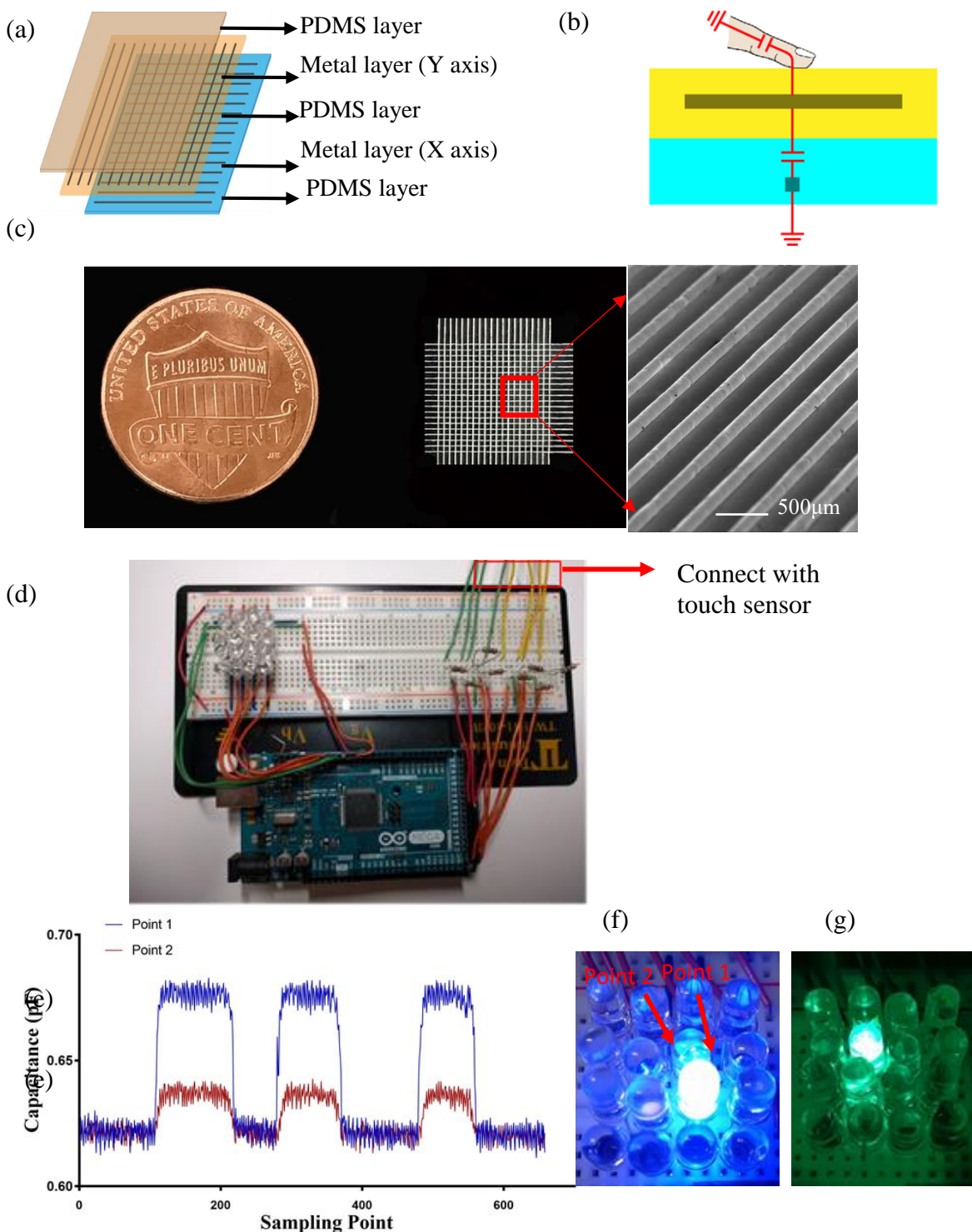


Figure 6.9 (a) schematic of printed touch sensor. (b) Working principle of touch sensor matrix. (c) Optical images and SEM image of a 20x20 touch sensor array and compared with a one cent coin. (d) A microcontroller board (ARDUINO MEGA 2560) was used to map the signal from 4x4 touch sensors array to a 4x4 LED matrix. (e) The change of the capacitance when touch point under different sampling point. (f) and (g) Activated LED on point 1 and point 2.

other grounded conducting medium (i.e., touching tip), there will be a capacitance change at each intersect point, and this capacitance change can be measured and analyzed to indicate the touch point, as shown in Figure 6.9 (b). With the high-resolution EHD printing, the 20 x 20 matrix or 400 touch sensors were printed onto a 10x10 mm area. The spacing between two neighboring traces of the conductors was 500 microns. The optical image of the printed touch sensor array with an SEM image detailing the printed metallic filaments was shown in Figure 6.9 (c). High-resolution metal filaments with uniform linewidth and smooth edges were observed in the SEM image from one layer of the conductive traces. The precisely printed high-quality filaments helped to minimize the variation in the capacitance from each sensing element. The change in capacitance from each sensor node was used to detect touch at each intersection. To test the performance of the touch sensors while reducing the complexity in electronic connections, we randomly selected a 4x4 sensor nodes and connected them to a control board (ARDUINO MEGA 2560) as shown in the Figure 6.9.(d). A 4x4 LED matrix is also connected to the chip board, which purchase from ARDUINO to represent the 4x4 sensor nodes. If one of the nodes is touched by the finger or touch pen, the corresponding LED light will ON, otherwise it will keep off. The control board has the ability to detect the changes of the capacitance and can generate a signal based on the capacitance change by the program. This signal is used to control the On/Off of the LED in the corresponding 4x4 LED matrix. Due to the high density of the touch sensor array, when touching one sensor (i.e., one intersection of the grid), the capacitance of the nearby sensors around the target sensor was changed too, but with smaller amplitudes. In order to distinguish the touched node with surrounding nodes, a threshold value has to be selected. As shown in Figure 6.9 (e), when touch sensor 1 was touched by a touch pen tip with a tip diameter of 0.7mm, the capacitance of the touch sensor 1 was changed by 0.06 pF from 0.62pF to 0.68pF.

The capacitance of the touch sensor around sensor 1 also changed by a smaller amount of 0.02 pF (from 0.62pF to 0.64pF). With carefully selecting the proper threshold value of the capacitance change (0.04 pF in this experiment), touch signal from each individual sensor was detected. In Figure 6.9 (f,g), the signal from the touch sensors was successfully detected and used to turn on the LED lights that were controlled by the corresponding touch sensor.

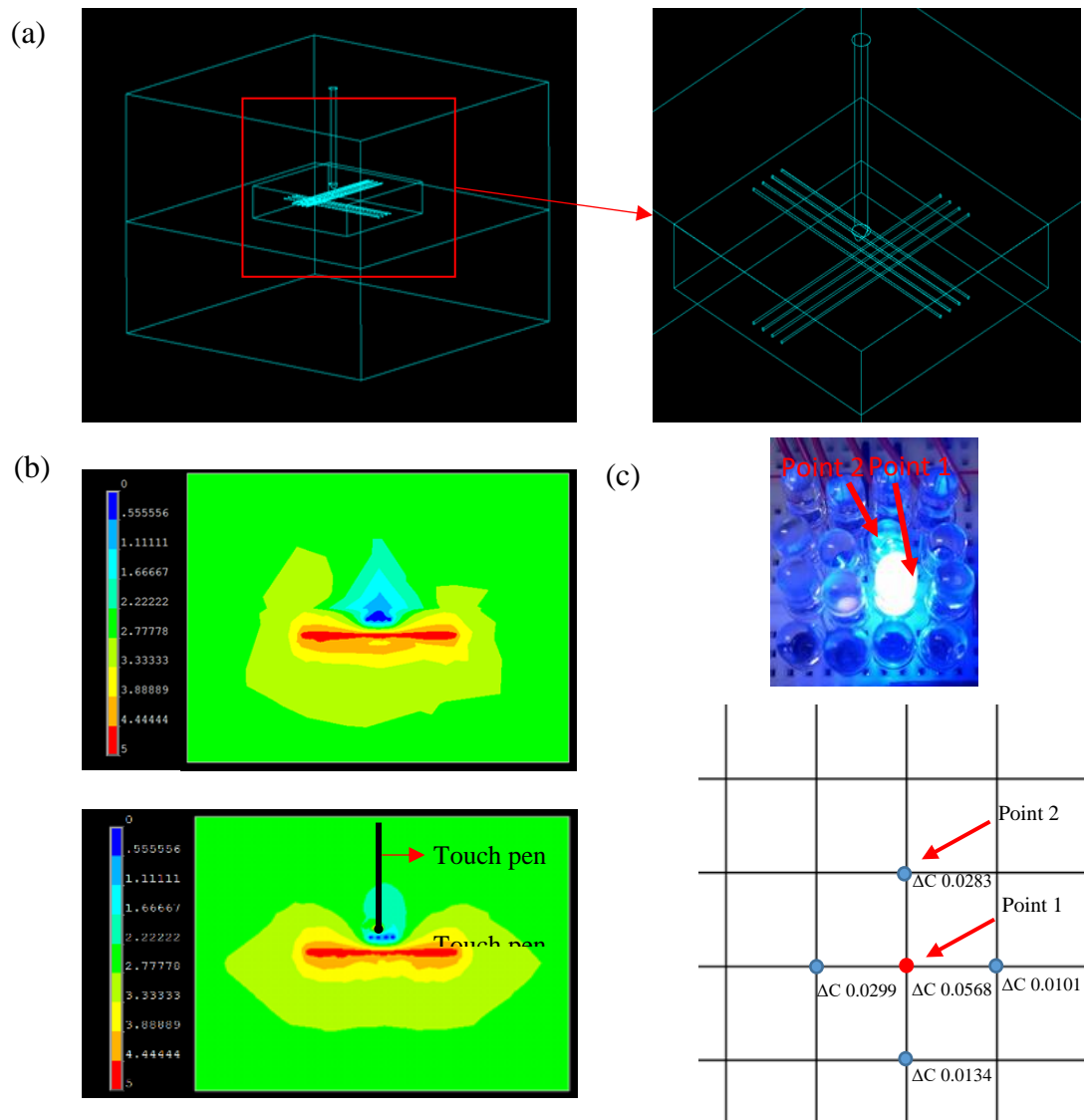


Figure. 6.10 (a) FEA model for touch sensor design. (b) Cross section of electric potential of touch sensor with and without a touch pen (c) Simulation result of the changing capacitance ( $\Delta C$ ) of points when the touch pen touches red point (point 1) (unit: pF).

To verify the printed capacitance touch sensor, two FEA models are created for this touch sensor array with two layers of metal filament grid embedded in PDMS. One model does not contain a touch pen, and the other one has a touch pen that just touches the top surface of the PDMS layer without any pressure. The created model is shown in the Figure 6.10 (a). In order to simplify the calculation time, only four metal filaments in each layer are included in this simplified model, which form a 4 x 4 matrix or a 16 touch sensor points. The gap between X-axis metal traces and Y-axis metal traces is 1mm, and the thickness of two PDMS layers above and below the metal trace is set to 1.25mm. The voltage between X-axis and Y-axis is set to 5V, which is the same value that used in the test. The FEA simulation results of the electric potential of the touch sensor with and without touch pen are shown in the Figure 6.10 (d). It is clearly showing that there is a changing of electric potential distribution and electrical field strength at the same place when the touch pen touches the touch sensor from the top, which is due to the changing dielectric constant around the touch sensor. Figure 6.10 (e) shows the capacitance change of the touch sensor nodes around the touched point using touch tip. From the FEA results, the touched point has a capacitance change more than two times than other points around it, which makes this touch signal detectable and differentiable using the measuring device. Moreover, the simulation result on the touched sensor node and surrounding nodes have similar values with test results, which demonstrated the good performance of this printed touch sensor.

## **6.2 EHD PRINTING OF SILVER NANOWIRES FOR ELECTRONICS**

### **6.2.1 EHD Printing of AgNWs**

The printing system used for EHD AgNWs printing is as same as we have used for molten metal printing except for the heating system since the ink will be in the liquid phase at ambient condition. There is no commercial AgNW ink for the EHD printing, so the ink used in

this study is prepared and synthesized in the lab. The AgNW ink is obtained from mixing Poly (ethylene oxide) (PEO) solution with AgNW solution. The PEO powder ( $M_v$ : 1,000,000) is purchased from Sigma-Aldrich. The PEO powder is first mixed with DI water to form a PEO solution. The AgNW solution is obtained by mixing AgNW, and DI water and the solution has an AgNW concentration of 150mg/ml. The average length of the AgNW is about 25 $\mu$ m. In the final ink, the concentration of the AgNW is selected as 15mg/ml since higher AgNW concentration will cause AgNW clustering in the ink that will clog the nozzle, and lower AgNW concentration will reduce the conductivity. Obviously, the rheology of the ink has a large effect to the printing process, which three different weight ratios (3%, 4%, and 5%) of PEO concentrations have been tested. With a higher PEO concentration, the ink exhibited higher viscosity, which is difficult to allow ink flow out from the nozzle. Higher PEO concentration could also cause nozzle clogging, which will disturb the printing process. Lower PEO concentration will reduce the printing resolution due to the improved ink flowability. For the final ink, PEO with a concentration of 4% wt is selected.

To demonstrate the high-resolution printing capability, a pneumatic printing is brought to compare with EHD printing. Figure 6.11 (a) shows the pneumatic printing behavior around the nozzle with an applied pressure of 4psi. It obviously shows that due to the surface tension and viscosity of the ink, the formed droplet has a much larger size than the nozzle size, which cannot provide a high-resolution printing. In contrast to the pneumatic printing, the size of the EHD printed feature has a much smaller diameter than the nozzle size, as shown in the Figure 6.11 (b). The dashed line indicates the external profile of the nozzle. With the printing capability, different high-resolution AgNW features can be fabricated. Figure 6.11 (c) shows some of the printed

high-resolution patterns, and Figure 6.11 (d) shows the repeated patterns printed in large scale to demonstrate large-scale, high-resolution printing capability of this EHD printing of AgNWs.

Several parameters, such as applied voltage, applied pressure, standoff distance, printing speed, and nozzle, will affect the overall printing process. Due to the high viscosity of the ink, constant pressure of 0.4psi is applied to the system to assist the ink flow out from the nozzle. To eliminate the chance of getting clogged, a nozzle with an inner diameter of 250 $\mu$ m and outer

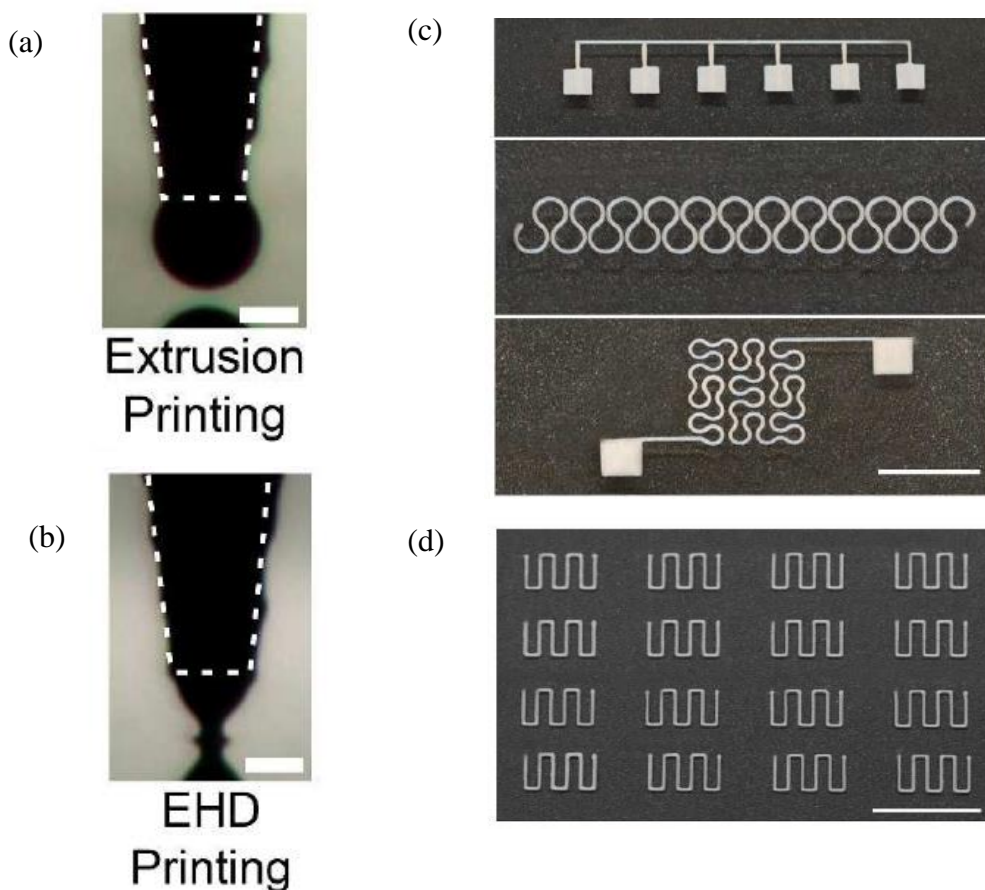


Figure 6.11 (a) and (b) Printing behavior for extrusion printing and EHD printing. Scale bar: 150 $\mu$ m. (c) Three different high-resolution AgNW patterns. (d) Large-scale AgNW pattern printed by EHD method. Scale bar: 5mm.

diameter of 150 $\mu$ m has been selected for printing AgNW ink. Applying a voltage to the system will result in an electrical field, which played a critical role in achieving the high printing resolution. As shown in the Figure 6.12(a), without applying a voltage, the ink just flows out and

accumulate around the nozzle tip to form a large drop. In this study, we have selected a voltage of 1500V for this system that is enough to deform the meniscus into a Taylor Cone and produce a fine jet. Besides applied voltage, both printing speed and standoff distance will affect the printing resolution and stability of the printing process. When fixing a printing voltage and pressure, the ink flow rate will be kept. Due to the high viscosity of this ink, relatively higher printing speed will result in a better resolution. When selecting a larger standoff distance, the

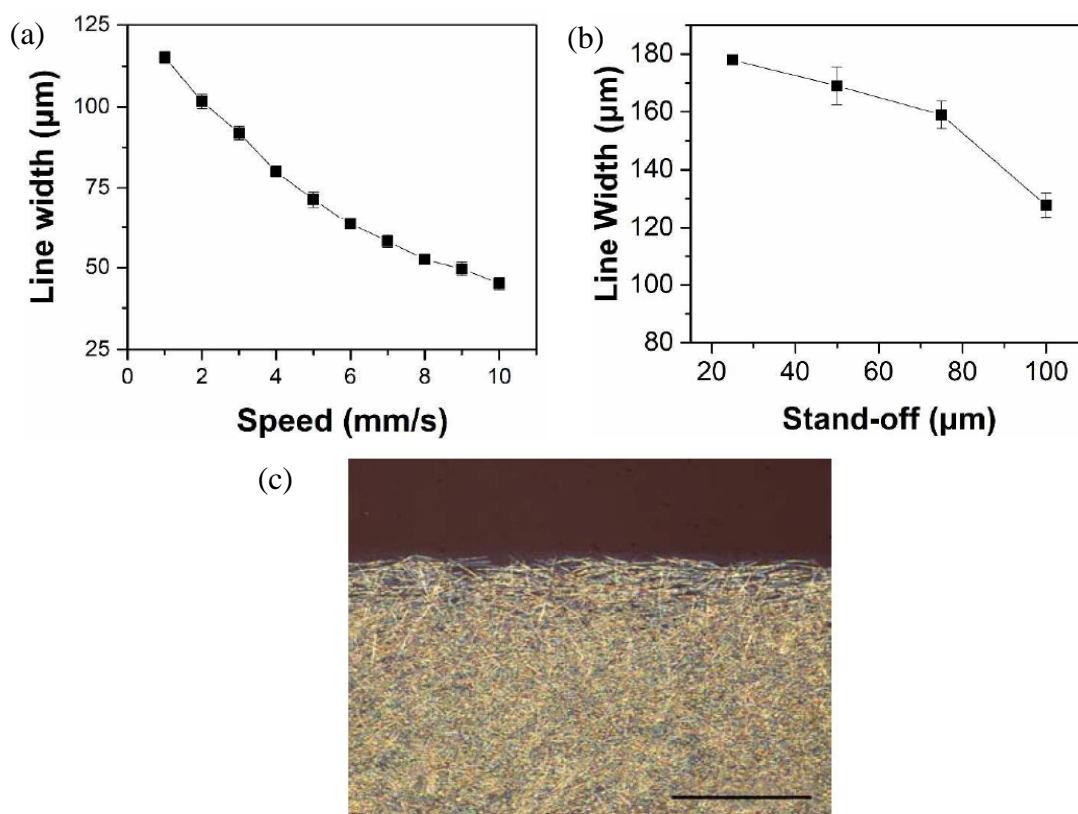


Figure 6.12 (a) and (b) Printed line width as a function of printing speed and stand-off. (c) Optical image shows the clean and smooth edge. Scale bar: 50 $\mu\text{m}$

printing resolution will improved. Figure 6.12 (a) and (b) shows the printing result under different printing speed and standoff distance. The line width is decreasing while increasing the printing speed, which can be explained that higher printing speed will have a smaller amount of ink per unit length that leads to smaller line width. Increasing standoff distance will reduce the

electrical field strength that is resulting in a smaller ink flow rate, which leads to a smaller jet size. Printed AgNW features have a clean and smooth edge as shown in the Figure 6.12 (c), which is crucial for the circuit design and devices fabrication. Form the characterization process, the best line width of  $45\mu\text{m}$  is obtained that is much smaller than the nozzle size. Moreover, this printing process is a nozzle clog-free process, which demonstrates that EHD printing can provide a high-resolution printing without clogging nozzles. For the rest of the studies, we have selected a standoff distance of  $75\mu\text{m}$  for the best printing behavior.

### 6.2.2 Morphology and Electrical Properties of Printed AgNW Conductors

The purpose of printing AgNW is to fabricate electric devices. The AgNW distribution and density in the printed lines have a great effect on its electrical properties. SEM image of printed NWs at the center and the edge of the printed lines under two different printing speed

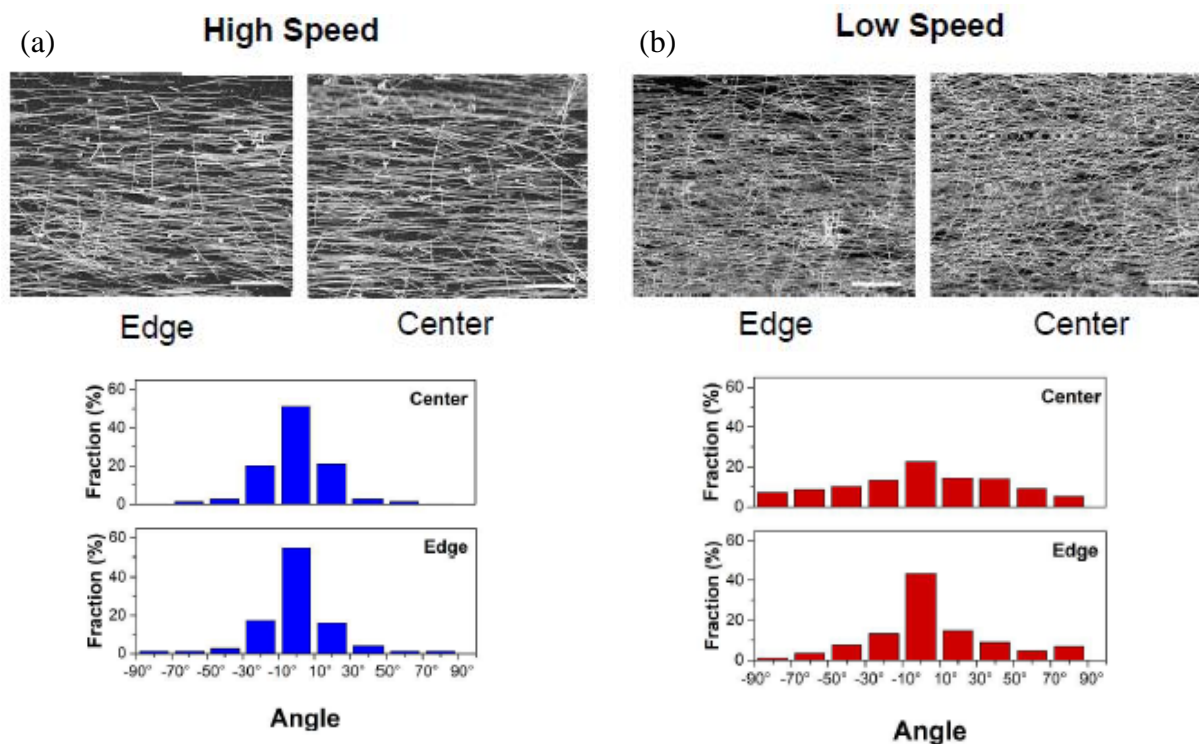


Figure 6.13 AgNW alignment at edge and center of the printed line with a printing of (a) 10mm/s and (b) 1mm/s. Scale bar:  $10\mu\text{m}$

(1mm/s and 10mm/s) has been studied, and the results show in the Figure 6.13. Based on those images, the alignment and density of the NWs can be directly measured. In each case, the number of NWs under the same area is counted and recorded with its orientation that denoted from  $-90$  to  $90^\circ$  with  $0^\circ$  pointing to the printing direction. For high printing speed, about 70% of the NWs are oriented from  $-10$  to  $10^\circ$  with respect to the printing direction, and slightly more aligned along the edge direction than it at the center due to the liquid drag force from high-speed printing. NWs are distributed more randomly under low printing speed, however, still more aligned in  $-10$  to  $10^\circ$  along the printing direction. As we know, in the drop-casting method, AgNW will form a precolation with complete randomly oriented. The alignment that observed in the EHD printing can be attributed to the shear flow. During the printing, the shear flow along the line edge will achieve better NW alignment along the edge rather than the center area, and

Table 6.1 AgNW density at the center and along the edge at two different printing speeds

	Center [ $\mu\text{m}^2$ ]	Edge [ $\mu\text{m}^2$ ]
High-speed (10mm/s)	0.59	0.58
Low-speed (1mm/s)	1.86	1.30

High printing speed will result in a higher shear flow, which causes the NWs have a better alignment under high printing speed. Table 6.1 shows the measured result of the AgNWs density and distribution. The density of the NWs is calculated by count the total number of the NWs in a  $50 \times 50\mu\text{m}$  area. Post-treatments are needed for the printed pattern before it to be used for testing of electrical property. Without the post-treatment, the printed patterns are not conductivity at all due to the high portion of the unconductivity material (PEO) in the printed patterns. The purpose of the post-treatment is to remove the PEO. The printed patterns are soaked in the DI water for 5mins to remove some of the PEO and then dried at  $50^\circ\text{C}$ . The

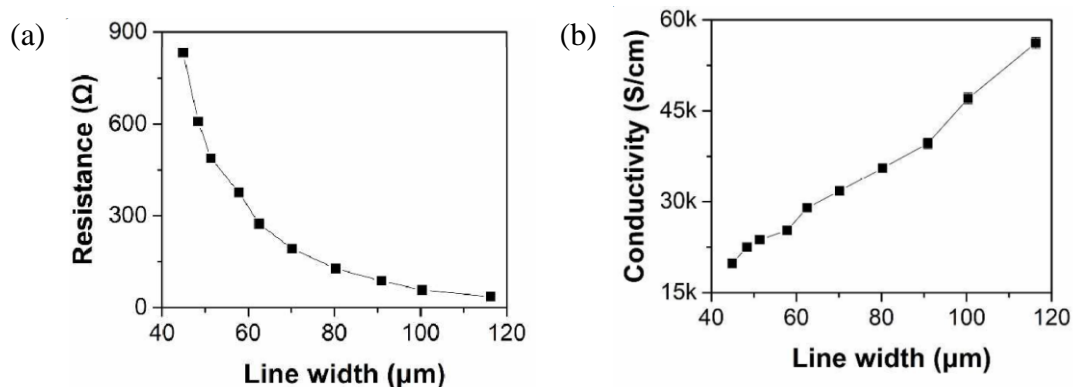


Figure 6.14 (a) The resistance of printed AgNW lines with different line widths. (b) The conductivity of the printed AgNW lines with different line widths.

patterns will be used to test its resistance. This process is repeated several time to ensure the PEO has been removed completely, and the resistance of the pattern will be minimized.

Electrical property that tested in this study is electrical conductivity. The patterns used for the test has a length of 10mm with varying line width from 45μm to 115μm, that printed by different printing speed. After the post-treatment, Four-wire (4W) measurement is used to measure the resistance of the each pattern. The measured data are shown in the Figure 6.14 (a), as larger line widths possess smaller resistance. The conductivity of the printed lines is also measured and calculated. The thickness and cross-section of printed lines are measured by a Veeco Dektak 150 Profilometer. The conductivity is calculated by  $\sigma=L/(RA)$ , where  $\sigma$  is the conductivity, L is the line length, R is the overall resistance, and A is the cross-section area. Figure 6.14 (b) shows the conductivity of the printed patterns. As the line width increases, the conductivity of the printed pattern is increasing; this is may due to the slower printing speed leads to a higher nanowire density that leads to higher conductivity.

Since we have already demonstrated the high-resolution AgNW pattern printing capability using EHD technology. Here, we have applied this method to fabricate high-resolution flexible and stretchable conductors. Different flexible or stretchable substrates, which include

PDMS (dopamine treated), PET, letter paper, nanofiber paper, polycarbonate filter (Whatman 111103) have been applied in EHD printing. The reason for using dopamine treated PDMS is that the treated PDMS surface will change from hydrophobic to hydrophilic, which allows a

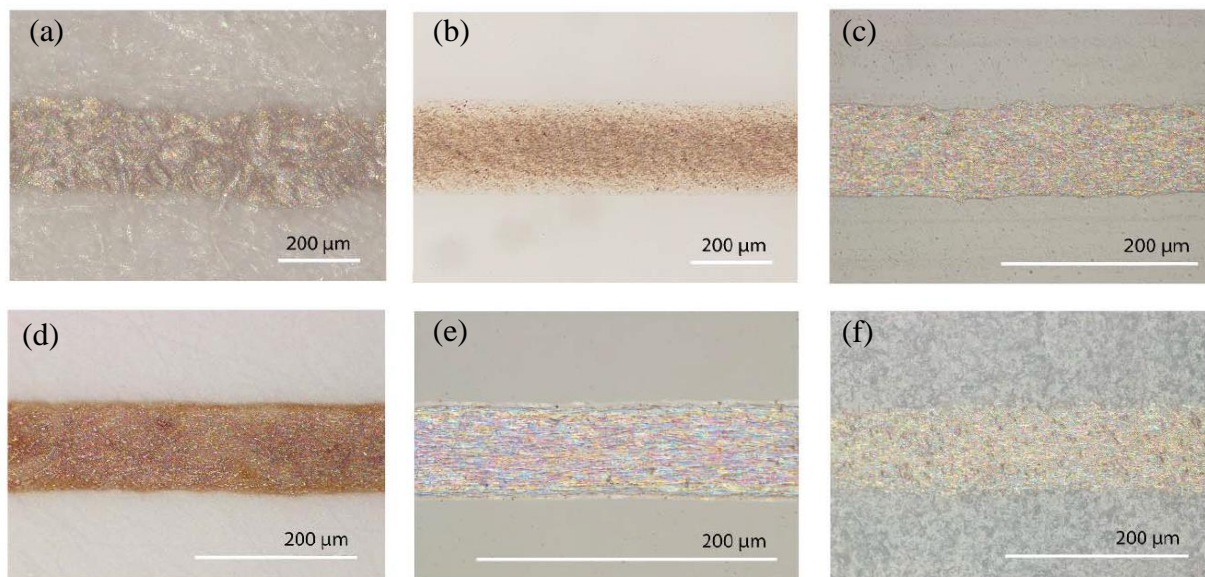


Figure 6.15 Optical image of printed AgNW lines on various substrates. (a) Printed on a variety of substrates (a) letter paper, (b) glass, (c) PET, (d) nanofiber paper, (e) PDMS and (f) polycarbonate filter.

stable ink settlement. Figure 6.15 shows the printed pattern on different substrates. With proper selecting the printing parameters, we have successfully EHD print AgNW ink on those substrates, which has the potential to fabricate flexible or stretchable conductors on those substrates.

To evaluate the flexibility and stretchability of the printed AgNW conductors, bending and tensile tests are performed in this study. For the bending test, the AgNW patterns are printed on PET film, which has a film thickness of  $\sim 120\mu\text{m}$ . After the post-treatment, printed patterns are connected with wires and located on a bending stage, which can provide a bending angle from  $0^\circ$  to  $180^\circ$  as shown in the Figure 6.16 (a). From the test, the maximum strain in the

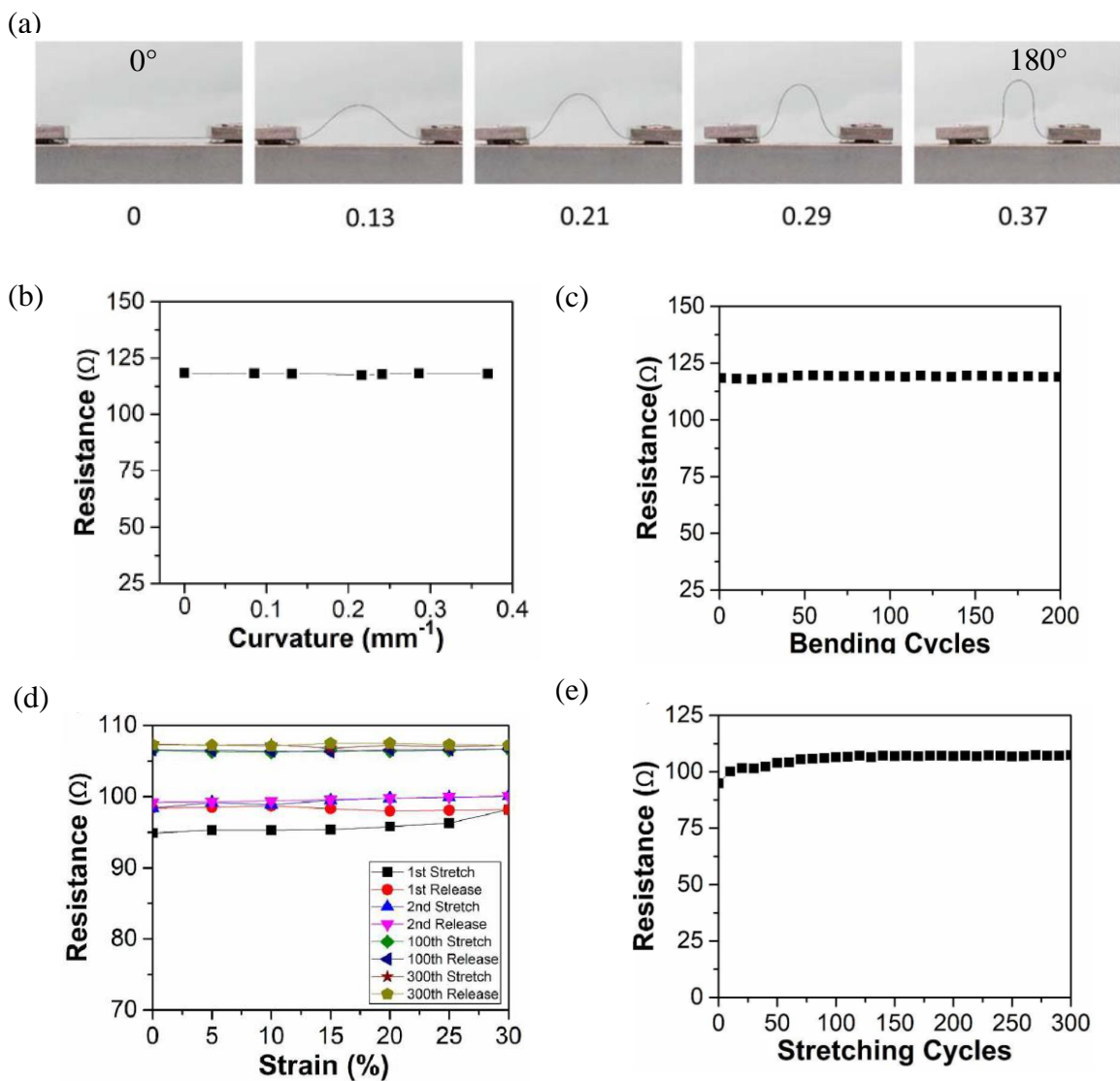


Figure 6.16 (a) Optical image of bending test of bending angle from  $0^\circ$  to  $180^\circ$ . (b) Resistance of printed AgNW pattern under different bending curvature. (c) Resistance under 200 bending cycles with a bending curvature of 0.37 (bending radius 2.7mm). (d) Resistance as a function of different strain under different stretching and releasing cycle. (f) Resistance under 300 cycles of stretching and releasing

AgNWs with a bending angle of  $180^\circ$  (bending radius is about 2.7mm) is about 0.76%. The changes of the resistance may be due to the movement and the redistribution of the AgNWs in the printed patterns. Figure 6.16 (b) showing the resistance at different bending radius during the bending test with increment bending radius from infinity to 2.7mm. A fatigue test of 200 cycles

of the bending has performed, and a stable resistance is observed from the test that shows in the Figure 6.16 (c). To study the stretchability of the printed patterns, the tensile test has been conducted for the patterns that printed on the PDMS film. To create a high stretchable AgNW conductor on PDMS, the AgNW patterns are printed on the PDMS substrate that was pre-strained at 50%, then released after post-treatment. The purpose of the pre-straining/releasing process is to generate a wavy AgNW/PDMS structure that is commonly used to fabricate stretchable electronics with a nearly stable resistance during the stretching. The prepared sample is wiring with a multimeter (34001A, keysight Technologies) and located on a stretching table for the stretching test. The maximum tensile strain that applied to the sample is 30%. A repeated stretching/releasing cycle test is also performed, and the result is shown in Figure 6.16 (d) and (c). There is a little increasing in resistance during the first stretching; after that, for each stretching process, the resistance can almost keep a stable value from 0% strain to 30% strain. For the first 50 cycles, there is a 10.6% increase in resistance; however, after 50 cycles, the resistance shows excellent stability. The reason for the increasing of resistance at the beginning of the test can be explained that the NWs have to shift or relocate during the first several stretching cycles before they finally get stable. Once NWs are stable on the substrate, a stable resistance reaction is provided during the stretching. From the bending and stretching test, the EHD printed AgNW conductors exhibited excellent flexibility and stretchability that is vital for many next-generation electronics.

### 6.2.3 EHD Printed AgNW Devices

Wearable devices are becoming more important for applications like medical device, sensing, healthcare, navigation, etc. Previous section has demonstrated the excellent flexibility and stretchability for the printed conductors, which has the potential for applying to wearable

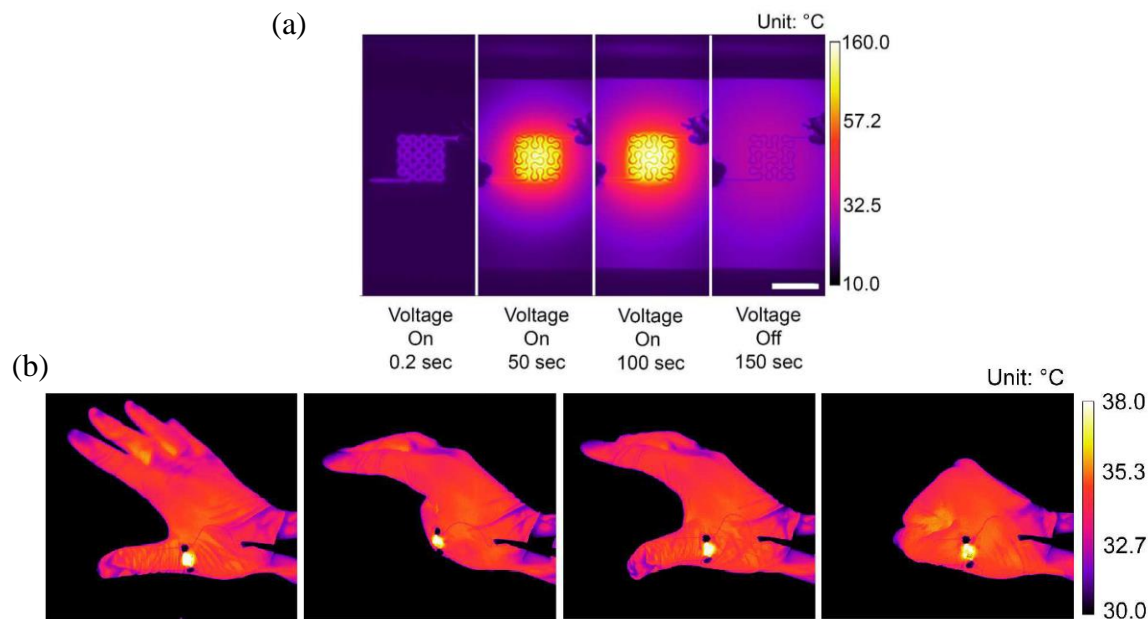


Figure 6.17 (a) IR image of printed AgNW heater under activated/de-activated condition. Scale bar: 5mm (b) IR image of AgNW heater printed on a lab-use gloves

devices. Here, we have presented two printed devices that fabricated by EHD printing technology. Figure 6.17 (a) shows the printed wearable heater with a fractal pattern of Peano curves under infrared images. To improve the flexibility and stretchability, the arc sections replace the sharp corners from the mathematically defined fractal layout. Moreover, with the Peano curves, this kind of fractal layout can cover large area (6 x 6mm for this experiment) that can reduce the cost and time. Figure 6.17 (a) also shows several infrared images of activated/deactivated heater. After activated the heater, a uniform temperature distribution is observed with a maximum temperature of 160°C at 25V. This uniform temperature distribution indicates very good performance. This same heater structure is also printed onto lab-used gloves to demonstrate the potential application for wearable devices. Once activated the heater, results from infrared images (Figure 6.17 (b) shows a stable heating performance during bending, stretching, and/or twisting process that exhibited an excellent heating performance.

Dry ECG electrodes have many advantages when compared with wet ECG, such as it can be used for a long-term health monitoring since electrolytic gel layers are not required, and it will not cause skin irritation under long-term wear [151]. Dry ECG printed by AgNW has shown an outstanding performances [152]. In this study, AgNWs are printed onto PDMS with a fractal pattern of Greece Cross, which can release the local strain under stretching or bending. Figure 6.18 (a) shows the printed pattern on a non-pre-strain PDMS film, which has a small thickness of 300 $\mu$ m for a comfort contacting between the skin and the conductive layer. Liquid metal is used to connect the wire and printed pattern. A commercial wet ECG product from 3M is also purchased for this study as a comparison. Figure 6.18 (b) shows the result of the printed

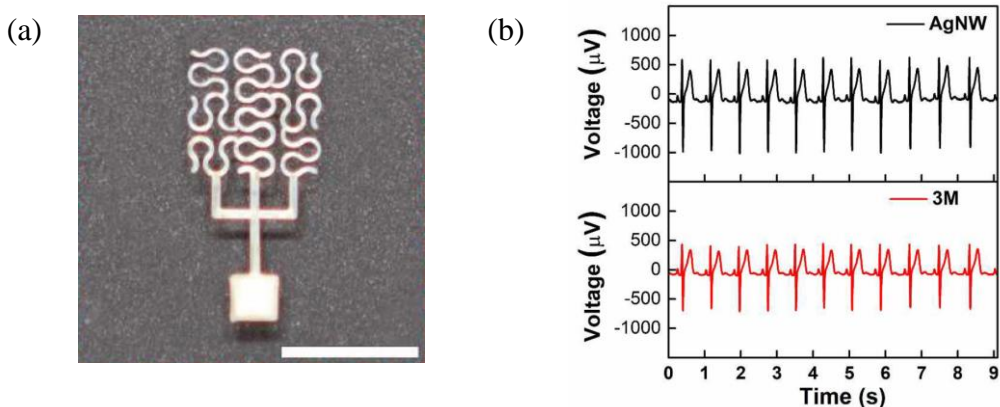


Figure 6.18 (a) Printed dry ECG on PDMS film. Scale bar: 5mm. (b) ECG signals collected from the AgNW dry ECG electrode and a commercial 3M wet electrode for comparison

ECG and commercial product. The result shows an excellent performance of the printed ECG when compared to that obtained from the 3M electrode, and the printed ECG are suitable for Long-term healthy monitoring.

### 6.3 CHAPTER SUMMER

In this chapter, we have successfully developed EHD printing process for fabrication of high-resolution flexible and stretchable electronics with molten metal and AgNWs. In the study of EHD molten metal printing, we first studied the effect of some critical printing parameters,

such as applied voltage and printing speed on the printing process. With the optimal printing parameters, high-resolution metal filament, 2D features, and 3D structures can be directly printed without any pneumatic pressure. By comparing with the traditional extrusion based metal printing, EHD printing technology can effectively improve the printing resolution to sub-50 $\mu\text{m}$ . With this printing ability, electronics with excellent flexibility and stretchability have been fabricated and test. A stable electrical response is achieved during the bending test, and the resistance only has a slight change from the rigorous bending. Different pattern designs are studied for the stretchability test, and a horseshoe pattern shows the best stretchability that can withstand a large tensile strain of 70%. Moreover, due to the low melting point property of this metal, the printed electronics are capable of self-healing. With a heat treatment and a small pressure, the electronics can recover from failure without degrading much of their electrical properties. A high-density touch sensor array is designed and fabricated to demonstrate high-resolution direct patterning capability of EHD printing. An FEA model is developed to simulate the touch sensor performance, and compared with experimental results. The experimental results agree well with the FEA results. With excellent flexibility, stretchability, self-healing, and high-resolution printing ability, direct EHD molten metal printing electronics can be applied to a variant of applications in next-generation electronics that requires good flexibility and stretchability. AgNWs material is also using for fabricating flexible and stretchable conductors. Characterization processes are performed to find the best printing parameters, and a variety of flexible or stretchable substrate has been demonstrated that can be used for EHD printing of AgNWs. The printed AgNW pattern is highly conductive with a conductivity of about  $5.6 \times 10^6$  S/m after post-treatment. With the high-resolution printing capability, flexible and stretchable conductors are successfully fabricated. Bending test and stretching test showed excellent

performance for those printed conductors, and a wearable heater and dry ECG have been directly printed and test. The result showed an excellent performance that demonstrates the EHD printing of AgNW is suitable for fabricating flexible and stretchable conductors.

## CHAPTER 7 FUTURE WORK, SUMMARY AND TIMELINE

### 7.1 RESEARCH SUMMARY

In this study, we have investigated a high-resolution EHD printing technology for micro-scale 3D structure fabrication. First, a series of process developments have been performed for the EHD printing of phase-change ink. EHD printing using DC voltage, and AC voltage was successfully developed. For the DC voltage, we have studied the continuous DC voltage and pulsed DC voltage in EHD printing. When using the continuous DC voltage, only one printing parameter will affect the printing behavior if a fixed nozzle and standoff distance are used. The droplet size and droplet printing frequency will directly determine by the applied DC voltage. In order to control the droplet printing frequency and droplet size at the same time, a DC pulse voltage based printing process is developed. The characterization process showed that with DC pulse, a small droplet with controllable printing frequency can be achieved. We have also studied the AC voltage, which can neutralize the charges remain on the printed droplets and benefit high-resolution 3D printing especially on an insulating substrate. After obtaining the best printing condition, 3D structures can be printed with good quality and high-resolution.

In order to better understand the mechanism of the drop-on-demand EHD printing with phase-change ink, FEA models are created to simulate the overall printing process from droplet formation to droplet settlement. Due to the highly complex mechanism in the EHD printing, we studied the pending state of the droplet about to detach from the Taylor cone. Experiments have been conducted to validate the simulation results, which have a good match with the experimental results. This model gives a better understanding of the mechanism of EHD printing, and it also can provide valuable guidelines for the printing process control and has the potential to predicate droplet size and footprint under different printing conditions.

For traditional EHD printing system, the ground electrode is placed under the substrate, and the printed structures will be located between the substrate and the nozzle. The printed substrate will distort the electric field, and make the process difficult to control. Moreover, the standoff distance will limit the maximum height of the printed features. In order to make the printing system substrate-independent and to overcome the standoff distance limitation on the height of the printed structures, a new ground electrode is designed and integrated with the printing nozzle. The new ground electrode has a circle hole in the middle of a thin slide, whose top surface is coated with the conductive material. FEA simulations have been performed to find the best design parameters, and the simulation results were also used to compare with the experiment results. The two results have a good agreement with each other, which indicates that the designed ring electrode can provide the same function as a traditional planar electrode and it has the capability to start and maintain the EHD printing. With this new electrode design, high-resolution 3D structures with large aspect ratio can be fabricated.

Metallic materials are very important to many applications, and existing metal additive manufacturing technology cannot provide high-resolution and cost-effective fabrication. In our study, we have successfully developed an EHD printing process for the high-resolution 2D and 3D printing of molten metal. With the carefully characterized printing parameters, high-resolution 2D and 3D metal features can be directly printed. By comparing with the traditional extrusion based metal printing, EHD printing technology can effectively improve the printing resolution to about  $45\mu\text{m}$ . With this printing ability, we have successfully printed flexible, and stretchable electronics with their flexibility and stretchability tested in the experiment. A good electrical response is achieved during the bending test and stretching tests, and the resistance only has a slight change from the rigorous bending or stretching tests. The printed electronics are

also capable of self-healing. With a heat treatment and a small pressure on the break point, the electronics can recover from failure without degrading much of their electrical properties. To demonstrate high-resolution direct patterning capability of EHD printing, a high-density touch sensor array is designed and fabricated. All of those test results demonstrated that EHD print approach is a high-resolution printing technology that can produce self-healing electronics with excellent flexibility, stretchability, which can be applied to a variant of applications in a wearable device that requires good flexibility and stretchability.

Longer metallic nanowires can provide excellent performance in the fabrication of flexible and stretchable electronics, due to their high electric conductivity, high stretchability, and good optical transmittance. However, it is very difficult to fabricate high-resolution, high conductive flexible and stretchable electronics with the commonly used printing method. In our study, we have developed an EHD printing process, which can provide high-resolution printing for silver nanowire ink. To find the best ink formula, different combinations of the AgNW inks have been tested in the EHD printing. Six different substrates, which include five flexible or stretchable substrates have been used for demonstrating the flexibility of EHD printing AgNWs. After the post-treatment, the printed features have a highest electric conductivity of  $\sim 5.6 \times 10^6$  S/m, which is enough for fabricating of flexible and stretchable electronics. Two wearable devices have been successfully fabricated. A flexible heater shows a uniform temperature distribution with the highest temperature of  $160^\circ\text{C}$ . The heater is also printed on a lab-use glove to show the stable heating performance under bending, stretching and twisting. A dry ECG is printed and compared with a commercial 3M wet ECG. The result shows excellent performance on collecting the signals, which is ideal for long-term use applications.

## 7.2 FUTURE WORK

It has been demonstrated in this study that the EHD printing technology truly a high-resolution fabrication method, which can print with a variety of materials for different applications. The future research could be divided into several different tasks: 4D printing for electronics and biomedical engineering; hybrid printing for functional devices; and explore the fundamental mechanism of the printing process.

- 4D printing can be applied to many applications such as actuator, drug delivery, and electronics. Currently, most of the current 4D printed structures have a resolution of millimeter scale or above, which limits their development in high precision applications. EHD printing technology allows printing a variety of materials used for 4D printing, for example, hydrogel and PCL. The future research, an EHD printing process will be studied for printing micro-scale 4D structures that can benefit bioengineering, health care, and electronic industry.
- Smart materials require stimulus to trigger or drive the shape changing. Printed polymeric structures will be converted to different shapes when placed under different temperatures; while the hydrogel structures have dynamically shape changing during immersion in water. Future research can focus on fabricating devices with integrated multiple smart materials, which allow the devices to have different shape changes under the different stimulus. As a result, the fabricated devices will be capable of providing multi-functions especially for applications that require high-resolution.
- For the traditional additive manufacturing, limited printing methods and materials are used during the fabrication process, which limits the functions of the products. With hybrid printing technology, most of the products that are difficult to fabricate in

traditional additive manufacturing can be directly printed. For example, if a product requires integrated electrical component, optical component, and a mechanical structure together, such products are difficult to be fabricated by traditional additive manufacturing methods. Hybrid printing with high-resolution capability will benefit in many applications, such as direct fabrication of micro transistor, sensors, and actuators. The future research can focus on the hybrid printing of electronics, which will integrate EHD printing with other additive manufacturing methods (FDM, direct writing, SLS, etc.). Based on the previous research on EHD printing of AgNW and metal, the EHD printing could be responsible for the high-resolution printing of electric components, and the remained structures of the devices will be fabricated by other additive manufacturing methods.

- It is radically important to understand fundamental physics of the overall printing processes, which contains several different stages such as droplet or jet formation, droplet or jet in-flight, and droplet or jet impact and solidification. Each stage has its unique characteristics and property parameters. Several simple models have been built in the previous work, but they are based on many assumptions and simplification, and they are still only focused on the droplet. More advanced models should be created that could predicate the droplet or jet formation, size, time-scale, in-flight and settlement morphology for different kind of materials if the properties (such as surface tension, viscosity, dipole moment, dielectric constant, conductivity, temperature, etc.) of the ink are known. Ideally, having an advanced completely modeling could save lots of time on material preparation and testing, prediction of printing behavior, and printing troubleshooting.

## REFERENCES

- [1] Beaman, J. J., Barlow, J. W., Bourell, D. L., Crawford, R. H., Marcus, H. L., & McAlea, K. P. (1997). Solid freeform fabrication: a new direction in manufacturing. *Kluwer Academic Publishers, Norwell, MA, 2061*, 25-49.
- [2] Gibson, I., Rosen, D. W., & Stucker, B. (2010). *Additive manufacturing technologies* (Vol. 238): Springer.
- [3] Hutmacher, D. W., Sittinger, M., & Risbud, M. V. (2004). Scaffold-based tissue engineering: rationale for computer-aided design and solid free-form fabrication systems. *TRENDS in Biotechnology*, 22(7), 354-362.
- [4] Kruth, J.-P., Leu, M.-C., & Nakagawa, T. (1998). Progress in additive manufacturing and rapid prototyping. *CIRP Annals-Manufacturing Technology*, 47(2), 525-540.
- [5] Melchels, F. P., Domingos, M. A., Klein, T. J., Malda, J., Bartolo, P. J., & Hutmacher, D. W. (2012). Additive manufacturing of tissues and organs. *Progress in Polymer Science*, 37(8), 1079-1104.
- [6] Mishra, S., Barton, K. L., Alleyne, A. G., Ferreira, P. M., & Rogers, J. A. (2010). High-speed and drop-on-demand printing with a pulsed electrohydrodynamic jet. *Journal of Micromechanics and Microengineering*, 20(9), 095026.
- [7] Park, J.-U., Hardy, M., Kang, S. J., Barton, K., Adair, K., kishore Mukhopadhyay, D., . . . Georgiadis, J. G. (2007). High-resolution electrohydrodynamic jet printing. *Nature materials*, 6(10), 782-789.
- [8] Poellmann, M. J., Barton, K. L., Mishra, S., & Johnson, A. J. W. (2011). Patterned hydrogel substrates for cell culture with electrohydrodynamic jet printing. *Macromolecular bioscience*, 11(9), 1164-1168.

- [9] Tan, J., & Saltzman, W. M. (2002). Topographical control of human neutrophil motility on micropatterned materials with various surface chemistry. *Biomaterials*, 23(15), 3215-3225.
- [10] Wang, K., Cai, L., Zhang, L., Dong, J., & Wang, S. (2012). Biodegradable Photo - Crosslinked Polymer Substrates with Concentric Microgrooves for Regulating MC3T3 - E1 Cell Behavior. *Advanced healthcare materials*, 1(3), 292-301.
- [11] Wei, C., & Dong, J. (2013). Direct fabrication of high-resolution three-dimensional polymeric scaffolds using electrohydrodynamic hot jet plotting. *Journal of Micromechanics and Microengineering*, 23(2), 025017.
- [12] Wei, C., & Dong, J. (2014). Hybrid hierarchical fabrication of three-dimensional scaffolds. *Journal of Manufacturing Processes*, 16(2), 257-263.
- [13] Lee, H.-H., Chou, K.-S., & Huang, K.-C. (2005). Inkjet printing of nanosized silver colloids. *Nanotechnology*, 16(10), 2436.
- [14] Russo, A., Ahn, B. Y., Adams, J. J., Duoss, E. B., Bernhard, J. T., & Lewis, J. A. (2011). Pen - on - paper flexible electronics. *Advanced Materials*, 23(30), 3426-3430.
- [15] Park, M., Im, J., Shin, M., Min, Y., Park, J., Cho, H., . . . Chung, D.-Y. (2012). Highly stretchable electric circuits from a composite material of silver nanoparticles and elastomeric fibres. *Nature nanotechnology*, 7(12), 803-809.
- [16] Blanchet, G. B., Loo, Y.-L., Rogers, J., Gao, F., & Fincher, C. (2003). Large area, high resolution, dry printing of conducting polymers for organic electronics. *Applied Physics Letters*, 82(3), 463-465.
- [17] Forrest, S. R. (2004). The path to ubiquitous and low-cost organic electronic appliances on plastic. *Nature*, 428(6986), 911-918.

- [18] Hohnholz, D., Okuzaki, H., & MacDiarmid, A. G. (2005). Plastic electronic devices through line patterning of conducting polymers. *Advanced functional materials*, 15(1), 51-56.
- [19] Rashed Khan, M., Hayes, G. J., So, J.-H., Lazzi, G., & Dickey, M. D. (2011). A frequency shifting liquid metal antenna with pressure responsiveness. *Applied Physics Letters*, 99(1), 013501.
- [20] Zhang, Q., Zheng, Y., & Liu, J. (2012). Direct writing of electronics based on alloy and metal (DREAM) ink: A newly emerging area and its impact on energy, environment and health sciences. *Frontiers in Energy*, 6(4), 311-340.
- [21] Ladd, C., So, J. H., Muth, J., & Dickey, M. D. (2013). 3D printing of free standing liquid metal microstructures. *Advanced Materials*, 25(36), 5081-5085.
- [22] Boley, J. W., White, E. L., Chiu, G. T. C., & Kramer, R. K. (2014). Direct writing of gallium - indium alloy for stretchable electronics. *Advanced functional materials*, 24(23), 3501-3507.
- [23] Zheng, Y., He, Z., Gao, Y., & Liu, J. (2013). Direct desktop printed-circuits-on-paper flexible electronics. *Scientific reports*, 3, 1786.
- [24] Zheng, Y., He, Z.-Z., Yang, J., & Liu, J. (2014). Personal electronics printing via tapping mode composite liquid metal ink delivery and adhesion mechanism. *Scientific reports*, 4, 4588.
- [25] Wang, L., & Liu, J. (2014). *Printing low-melting-point alloy ink to directly make a solidified circuit or functional device with a heating pen*. Paper presented at the Proceedings of the Royal Society of London A: Mathematical, Physical and Engineering Sciences.

- [26] Wang, L., & Liu, J. (2014). Liquid phase 3D printing for quickly manufacturing conductive metal objects with low melting point alloy ink. *Science China Technological Sciences*, 57(9), 1721-1728.
- [27] Yu, Y., Yu, Y., Liu, F., Liu, F., Liu, J., & Liu, J. (2017). Direct 3D printing of low melting point alloy via adhesion mechanism. *Rapid prototyping journal*, 23(3), 642-650.
- [28] De, S., Higgins, T. M., Lyons, P. E., Doherty, E. M., Nirmalraj, P. N., Blau, W. J., . . . Coleman, J. N. (2009). Silver nanowire networks as flexible, transparent, conducting films: extremely high DC to optical conductivity ratios. *ACS nano*, 3(7), 1767-1774.
- [29] Hu, L., Kim, H. S., Lee, J.-Y., Peumans, P., & Cui, Y. (2010). Scalable coating and properties of transparent, flexible, silver nanowire electrodes. *ACS nano*, 4(5), 2955-2963.
- [30] Yu, Z., Zhang, Q., Li, L., Chen, Q., Niu, X., Liu, J., & Pei, Q. (2011). Highly flexible silver nanowire electrodes for shape - memory polymer light - emitting diodes. *Advanced Materials*, 23(5), 664-668.
- [31] Xu, F., & Zhu, Y. (2012). Highly conductive and stretchable silver nanowire conductors. *Advanced Materials*, 24(37), 5117-5122.
- [32] Yao, S., & Zhu, Y. (2015). Nanomaterial - enabled stretchable conductors: strategies, materials and devices. *Advanced Materials*, 27(9), 1480-1511.
- [33] Lee, P., Lee, J., Lee, H., Yeo, J., Hong, S., Nam, K. H., . . . Ko, S. H. (2012). Highly stretchable and highly conductive metal electrode by very long metal nanowire percolation network. *Advanced Materials*, 24(25), 3326-3332.
- [34] Leem, D. S., Edwards, A., Faist, M., Nelson, J., Bradley, D. D., & de Mello, J. C. (2011). Efficient organic solar cells with solution - processed silver nanowire electrodes. *Advanced Materials*, 23(38), 4371-4375.

- [35] Madaria, A. R., Kumar, A., & Zhou, C. (2011). Large scale, highly conductive and patterned transparent films of silver nanowires on arbitrary substrates and their application in touch screens. *Nanotechnology*, 22(24), 245201.
- [36] Song, M., You, D. S., Lim, K., Park, S., Jung, S., Kim, C. S., . . . Park, J. (2013). Highly efficient and bendable organic solar cells with solution - processed silver nanowire electrodes. *Advanced functional materials*, 23(34), 4177-4184.
- [37] Angmo, D., Andersen, T. R., Bentzen, J. J., Helgesen, M., Søndergaard, R. R., Jørgensen, M., . . . Krebs, F. C. (2015). Roll - to - Roll Printed Silver Nanowire Semitransparent Electrodes for Fully Ambient Solution - Processed Tandem Polymer Solar Cells. *Advanced functional materials*, 25(28), 4539-4547.
- [38] Finn, D. J., Lotya, M., & Coleman, J. N. (2015). Inkjet printing of silver nanowire networks. *ACS applied materials & interfaces*, 7(17), 9254-9261.
- [39] Liang, J., Tong, K., & Pei, Q. (2016). A water - based silver - nanowire screen - print ink for the fabrication of stretchable conductors and wearable thin - film transistors. *Advanced Materials*, 28(28), 5986-5996.
- [40] Ashley, S. (1991). Rapid prototyping systems. *Mechanical Engineering*, 113(4), 34.
- [41] Kruth, J.-P. (1991). Material in excess manufacturing by rapid prototyping techniques. *CIRP Annals-Manufacturing Technology*, 40(2), 603-614.
- [42] Zein, I., Hutmacher, D. W., Tan, K. C., & Teoh, S. H. (2002). Fused deposition modeling of novel scaffold architectures for tissue engineering applications. *Biomaterials*, 23(4), 1169-1185.

- [43] Ahn, S.-H., Montero, M., Odell, D., Roundy, S., & Wright, P. K. (2002). Anisotropic material properties of fused deposition modeling ABS. *Rapid prototyping journal*, 8(4), 248-257.
- [44] Mohamed, O. A., Masood, S. H., & Bhowmik, J. L. (2015). Optimization of fused deposition modeling process parameters: a review of current research and future prospects. *Advances in Manufacturing*, 3(1), 42-53.
- [45] Smith, W. C., & Dean, R. W. (2013). Structural characteristics of fused deposition modeling polycarbonate material. *Polymer testing*, 32(8), 1306-1312.
- [46] Shofner, M., Lozano, K., Rodríguez - Macías, F., & Barrera, E. (2003). Nanofiber - reinforced polymers prepared by fused deposition modeling. *Journal of applied polymer science*, 89(11), 3081-3090.
- [47] Noorani, R. (2006). *Rapid prototyping: principles and applications*: John Wiley & Sons Incorporated.
- [48] Cooper, K. (2001). *Rapid prototyping technology: selection and application*: CRC press.
- [49] Wohlers, T. T. (2010). *Wohlers Report 2010: additive manufacturing state of the industry: annual worldwide progress report*: Wohlers Associates.
- [50] 3DAddFab- Powered by Objet Polyjet Technology. from <http://www.3daddfab.com/technology/>
- [51] Petrovic, V., Vicente Haro Gonzalez, J., Jorda Ferrando, O., Delgado Gordillo, J., Ramon Blasco Puchades, J., & Portoles Grinan, L. (2011). Additive layered manufacturing: sectors of industrial application shown through case studies. *International Journal of Production Research*, 49(4), 1061-1079.

- [52] Singh, R. (2011). Process capability study of polyjet printing for plastic components. *Journal of mechanical science and technology*, 25(4), 1011-1015.
- [53] Jacobs, P. F. (1992). *Rapid prototyping & manufacturing: fundamentals of stereolithography*: Society of Manufacturing Engineers.
- [54] Melchels, F. P., Feijen, J., & Grijpma, D. W. (2010). A review on stereolithography and its applications in biomedical engineering. *Biomaterials*, 31(24), 6121-6130.
- [55] Dhariwala, B., Hunt, E., & Boland, T. (2004). Rapid prototyping of tissue-engineering constructs, using photopolymerizable hydrogels and stereolithography. *Tissue engineering*, 10(9-10), 1316-1322.
- [56] Bens, A., Seitz, H., Bermes, G., Emons, M., Pansky, A., Roitzheim, B., . . . Tille, C. (2007). Non-toxic flexible photopolymers for medical stereolithography technology. *Rapid prototyping journal*, 13(1), 38-47.
- [57] Broer, D. J., Mol, G. N., & Challa, G. (1991). In - situ photopolymerization of oriented liquid - crystalline acrylates, 5.. Influence of the alkylene spacer on the properties of the mesogenic monomers and the formation and properties of oriented polymer networks. *Macromolecular Chemistry and Physics*, 192(1), 59-74.
- [58] Ullett, J. S., Benson-Tolle, T., Schultz, J. W., & Chartoff, R. (1999). Thermal-expansion and fracture toughness properties of parts made from liquid crystal stereolithography resins. *Materials & design*, 20(2), 91-97.
- [59] Ullett, J., Schultz, J., & Chartoff, R. (2000). Novel liquid crystal resins for stereolithography—processing parameters and mechanical analysis. *Rapid prototyping journal*, 6(1), 8-17.

- [60] Heller, C., Schwentenwein, M., Russmueller, G., Varga, F., Stampfl, J., & Liska, R. (2009). Vinyl esters: low cytotoxicity monomers for the fabrication of biocompatible 3D scaffolds by lithography based additive manufacturing. *Journal of Polymer Science Part A: Polymer Chemistry*, 47(24), 6941-6954.
- [61] Arcaute, K., Mann, B., & Wicker, R. (2010). Stereolithography of spatially controlled multi-material bioactive poly (ethylene glycol) scaffolds. *Acta biomaterialia*, 6(3), 1047-1054.
- [62] Zhang, X., Jiang, X., & Sun, C. (1999). Micro-stereolithography of polymeric and ceramic microstructures. *Sensors and Actuators A: Physical*, 77(2), 149-156.
- [63] Jiguet, S., Bertsch, A., & Renaud, P. (2002). *Microstereolithography and ceramic composite three-dimensional parts*. Paper presented at the Proceedings of the Shaping II conference, Gent, Belgium.
- [64] Provin, C., & Monneret, S. (2002). Complex ceramic-polymer composite microparts made by microstereolithography. *IEEE transactions on electronics packaging manufacturing*, 25(1), 59-63.
- [65] Bertsch, A., Jiguet, S., & Renaud, P. (2003). Microfabrication of ceramic components by microstereolithography. *Journal of Micromechanics and Microengineering*, 14(2), 197.
- [66] Lee, J. W., Lee, I. H., & Cho, D.-W. (2006). Development of micro-stereolithography technology using metal powder. *Microelectronic engineering*, 83(4), 1253-1256.
- [67] Gaspar, J., Bártolo, P. J., & Duarte, F. M. (2008). *Cure and rheological analysis of reinforced resins for stereolithography*. Paper presented at the Materials Science Forum.
- [68] Kim, H., Choi, J.-W., & Wicker, R. (2010). Scheduling and process planning for multiple material stereolithography. *Rapid prototyping journal*, 16(4), 232-240.

- [69] Vaezi, M., Seitz, H., & Yang, S. (2013). A review on 3D micro-additive manufacturing technologies. *The International Journal of Advanced Manufacturing Technology*, 67(5-8), 1721-1754.
- [70] Park, J., Tari, M. J., & Hahn, H. T. (2000). Characterization of the laminated object manufacturing (LOM) process. *Rapid prototyping journal*, 6(1), 36-50.
- [71] Halloran, J. W., Tomeckova, V., Gentry, S., Das, S., Cilino, P., Yuan, D., . . . Wu, T. (2011). Photopolymerization of powder suspensions for shaping ceramics. *Journal of the European Ceramic Society*, 31(14), 2613-2619.
- [72] Sachs, E. M., Haggerty, J. S., Cima, M. J., & Williams, P. A. (1993). Three-dimensional printing techniques: Google Patents.
- [73] Butscher, A., Bohner, M., Hofmann, S., Gauckler, L., & Müller, R. (2011). Structural and material approaches to bone tissue engineering in powder-based three-dimensional printing. *Acta biomaterialia*, 7(3), 907-920.
- [74] Lu, K., & Reynolds, W. T. (2008). 3DP process for fine mesh structure printing. *Powder technology*, 187(1), 11-18.
- [75] Seitz, H., Rieder, W., Irsen, S., Leukers, B., & Tille, C. (2005). Three - dimensional printing of porous ceramic scaffolds for bone tissue engineering. *Journal of Biomedical Materials Research Part B: Applied Biomaterials*, 74(2), 782-788.
- [76] Tay, B., Evans, J., & Edirisinghe, M. (2003). Solid freeform fabrication of ceramics. *International Materials Reviews*, 48(6), 341-370.
- [77] Bandyopadhyay, A., Krishna, B., Xue, W., & Bose, S. (2009). Application of laser engineered net shaping (LENS) to manufacture porous and functionally graded structures for load bearing implants. *Journal of Materials Science: Materials in Medicine*, 20(1), 29.

- [78] Balla, V. K., Bose, S., & Bandyopadhyay, A. (2008). Processing of bulk alumina ceramics using laser engineered net shaping. *International Journal of Applied Ceramic Technology*, 5(3), 234-242.
- [79] Liao, Y., Li, H., & Chiu, Y. (2006). Study of laminated object manufacturing with separately applied heating and pressing. *The International Journal of Advanced Manufacturing Technology*, 27(7), 703-707.
- [80] Xiong, Y. (2009). *Investigation of the laser engineered net shaping process for nanostructured cermets*: University of California, Davis.
- [81] Biamino, S., Penna, A., Ackelid, U., Sabbadini, S., Tassa, O., Fino, P., . . . Badini, C. (2011). Electron beam melting of Ti-48Al-2Cr-2Nb alloy: Microstructure and mechanical properties investigation. *Intermetallics*, 19(6), 776-781.
- [82] Sing, S. L., An, J., Yeong, W. Y., & Wiria, F. E. (2016). Laser and electron - beam powder - bed additive manufacturing of metallic implants: A review on processes, materials and designs. *Journal of Orthopaedic Research*, 34(3), 369-385.
- [83] Yu, P., Qian, M., Tomus, D., Brice, C. A., Schaffer, G. B., & Muddle, B. C. (2009). *Electron beam processing of aluminium alloys*. Paper presented at the Materials science forum.
- [84] Cormier, D., Harrysson, O., & West, H. (2004). Characterization of H13 steel produced via electron beam melting. *Rapid prototyping journal*, 10(1), 35-41.
- [85] Gaytan, S., Murr, L., Martinez, E., Martinez, J., Machado, B., Ramirez, D., . . . Wicker, R. (2010). Comparison of microstructures and mechanical properties for solid and mesh cobalt-base alloy prototypes fabricated by electron beam melting. *Metallurgical and Materials Transactions A*, 41(12), 3216-3227.

- [86] Murr, L., Esquivel, E., Quinones, S., Gaytan, S., Lopez, M., Martinez, E., . . . Martinez, J. (2009). Microstructures and mechanical properties of electron beam-rapid manufactured Ti-6Al-4V biomedical prototypes compared to wrought Ti-6Al-4V. *Materials characterization*, 60(2), 96-105.
- [87] Murr, L. E., Gaytan, S., Ceylan, A., Martinez, E., Martinez, J., Hernandez, D., . . . Collins, S. (2010). Characterization of titanium aluminide alloy components fabricated by additive manufacturing using electron beam melting. *Acta Materialia*, 58(5), 1887-1894.
- [88] Parthasarathy, J., Starly, B., Raman, S., & Christensen, A. (2010). Mechanical evaluation of porous titanium (Ti6Al4V) structures with electron beam melting (EBM). *Journal of the mechanical behavior of biomedical materials*, 3(3), 249-259.
- [89] Subramanian, K., Vail, N., Barlow, J., & Marcus, H. (1995). Selective laser sintering of alumina with polymer binders. *Rapid prototyping journal*, 1(2), 24-35.
- [90] Kruth, J.-P., Wang, X., Laoui, T., & Froyen, L. (2003). Lasers and materials in selective laser sintering. *Assembly Automation*, 23(4), 357-371.
- [91] Niu, H., & Chang, I. (2000). Selective laser sintering of gas atomized M2 high speed steel powder. *Journal of materials science*, 35(1), 31-38.
- [92] Regenfuß, P., Ebert, R., Klötzer, S., Hartwig, L., Exner, H., Brabant, T., & Petsch, T. (2004). Industrial laser micro sintering. *Proceedings of the 4th LANE, Erlangen, Germany, Sept*, 21-24.
- [93] Haferkamp, H., Ostendorf, A., Becker, H., Czerner, S., & Stippler, P. (2004). Combination of Yb: YAG-disc laser and roll-based powder deposition for the micro-laser sintering. *Journal of materials processing technology*, 149(1), 623-626.

- [94] Salmoria, G. V., Paggi, R. A., Lago, A., & Beal, V. E. (2011). Microstructural and mechanical characterization of PA12/MWCNTs nanocomposite manufactured by selective laser sintering. *Polymer testing*, 30(6), 611-615.
- [95] Tang, H.-H., Chiu, M.-L., & Yen, H.-C. (2011). Slurry-based selective laser sintering of polymer-coated ceramic powders to fabricate high strength alumina parts. *Journal of the European Ceramic Society*, 31(8), 1383-1388.
- [96] Clare, A. T., Chalker, P. R., Davies, S., Sutcliffe, C. J., & Tsopanos, S. (2008). Selective laser melting of high aspect ratio 3D nickel–titanium structures two way trained for MEMS applications. *International Journal of Mechanics and Materials in Design*, 4(2), 181-187.
- [97] Inkjet. from <http://www.dp3project.org/technologies/digital-printing/inkjet>
- [98] Kamphoefner, F. J. (1972). Ink jet printing. *IEEE Transactions on Electron Devices*, 19(4), 584-593.
- [99] Perçin, G., & Khuri-Yakub, B. T. (2002). Piezoelectrically actuated flextensional micromachined ultrasound droplet ejectors. *IEEE transactions on ultrasonics, ferroelectrics, and frequency control*, 49(6), 756-766.
- [100] Perçin, G., & Khuri-Yakub, B. T. (2002). Micromachined droplet ejector arrays for controlled ink-jet printing and deposition. *Review of Scientific Instruments*, 73(5), 2193-2196.
- [101] Perçin, G., & Khuri-Yakub, B. T. (2003). Piezoelectric droplet ejector for ink-jet printing of fluids and solid particles. *Review of Scientific Instruments*, 74(2), 1120-1127.
- [102] Yamaguchi, K., Sakai, K., Yamanaka, T., & Hirayama, T. (2000). Generation of three-dimensional micro structure using metal jet. *Precision Engineering*, 24(1), 2-8.

- [103] Haferl, S., & Poulidakos, D. (2003). Experimental investigation of the transient impact fluid dynamics and solidification of a molten microdroplet pile-up. *International journal of heat and mass transfer*, 46(3), 535-550.
- [104] Collins, R. T., Jones, J. J., Harris, M. T., & Basaran, O. A. (2008). Electrohydrodynamic tip streaming and emission of charged drops from liquid cones. *Nature Physics*, 4(2), 149-154.
- [105] Ferraro, P., Grilli, S., Miccio, L., & Vespini, V. (2008). Wettability patterning of lithium niobate substrate by modulating pyroelectric effect to form microarray of sessile droplets. *Applied Physics Letters*, 92(21), 213107.
- [106] Ferraro, P., Coppola, S., Grilli, S., Paturzo, M., & Vespini, V. (2010). Dispensing nanoscopic droplets and liquid patterning by pyroelectrodynamics shooting. *Nature nanotechnology*, 5(6), 429-435.
- [107] Tan, M. K., Friend, J. R., & Yeo, L. Y. (2009). Interfacial jetting phenomena induced by focused surface vibrations. *Physical Review Letters*, 103(2), 024501.
- [108] Alvarez, M., Friend, J., & Yeo, L. Y. (2008). Rapid generation of protein aerosols and nanoparticles via surface acoustic wave atomization. *Nanotechnology*, 19(45), 455103.
- [109] Alvarez, M., Yeo, L. Y., Friend, J. R., & Jamriska, M. (2009). Rapid production of protein-loaded biodegradable microparticles using surface acoustic waves. *Biomicrofluidics*, 3(1), 014102.
- [110] Dungchai, W., Chailapakul, O., & Henry, C. S. (2011). A low-cost, simple, and rapid fabrication method for paper-based microfluidics using wax screen-printing. *Analyst*, 136(1), 77-82.

- [111] Krebs, F. C. (2009). Fabrication and processing of polymer solar cells: a review of printing and coating techniques. *Solar energy materials and solar cells*, 93(4), 394-412.
- [112] Khan, S., Lorenzelli, L., & Dahiya, R. S. (2015). Technologies for printing sensors and electronics over large flexible substrates: a review. *IEEE Sensors Journal*, 15(6), 3164-3185.
- [113] Søndergaard, R. R., Hösel, M., & Krebs, F. C. (2013). Roll - to - Roll fabrication of large area functional organic materials. *Journal of Polymer Science Part B: Polymer Physics*, 51(1), 16-34.
- [114] Taylor, G. (1964). *Disintegration of water drops in an electric field*. Paper presented at the Proceedings of the Royal Society of London A: Mathematical, Physical and Engineering Sciences.
- [115] Gupta, A., Seifalian, A. M., Ahmad, Z., Edirisinghe, M. J., & Winslet, M. C. (2007). Novel electrohydrodynamic printing of nanocomposite biopolymer scaffolds. *Journal of bioactive and compatible polymers*, 22(3), 265-280.
- [116] Jaworek, A. (2007). Micro-and nanoparticle production by electrospraying. *Powder technology*, 176(1), 18-35.
- [117] Lee, D.-Y., Shin, Y.-S., Park, S.-E., Yu, T.-U., & Hwang, J. (2007). Electrohydrodynamic printing of silver nanoparticles by using a focused nanocolloid jet. *Applied Physics Letters*, 90(8), 081905.
- [118] Cloupeau, M., & Prunet-Foch, B. (1994). Electrohydrodynamic spraying functioning modes: a critical review. *Journal of Aerosol Science*, 25(6), 1021-1036.

- [119] Gries, K., Vieker, H., Götzhäuser, A., Agarwal, S., & Greiner, A. (2012). Preparation of Continuous Gold Nanowires by Electrospinning of High - Concentration Aqueous Dispersions of Gold Nanoparticles. *Small*, 8(9), 1436-1441.
- [120] Hansen, N. S., Cho, D., & Joo, Y. L. (2012). Metal Nanofibers with Highly Tunable Electrical and Magnetic Properties via Highly Loaded Water - Based Electrospinning. *Small*, 8(10), 1510-1514.
- [121] Kim, J. S., Chung, W. S., Kim, K., Kim, D. Y., Paeng, K. J., Jo, S. M., & Jang, S. Y. (2010). Performance optimization of polymer solar cells using electrostatically sprayed photoactive layers. *Advanced functional materials*, 20(20), 3538-3546.
- [122] Reneker, D. H., Yarin, A. L., Fong, H., & Koombhongse, S. (2000). Bending instability of electrically charged liquid jets of polymer solutions in electrospinning. *Journal of Applied Physics*, 87(9), 4531-4547.
- [123] Sill, T. J., & von Recum, H. A. (2008). Electrospinning: applications in drug delivery and tissue engineering. *Biomaterials*, 29(13), 1989-2006.
- [124] Smith, D. P. (1986). The electrohydrodynamic atomization of liquids. *IEEE Transactions on Industry Applications*(3), 527-535.
- [125] Collins, R. T., Sambath, K., Harris, M. T., & Basaran, O. A. (2013). Universal scaling laws for the disintegration of electrified drops. *Proceedings of the National Academy of Sciences*, 110(13), 4905-4910.
- [126] Galliker, P., Schneider, J., Eghlidi, H., Kress, S., Sandoghdar, V., & Poulikakos, D. (2012). Direct printing of nanostructures by electrostatic autofocussing of ink nanodroplets. *Nature communications*, 3, 890.

- [127] Sekitani, T., Noguchi, Y., Zschieschang, U., Klauk, H., & Someya, T. (2008). Organic transistors manufactured using inkjet technology with subfemtoliter accuracy. *Proceedings of the National Academy of Sciences*, 105(13), 4976-4980.
- [128] Wang, K., & Stark, J. P. (2010). Direct fabrication of electrically functional microstructures by fully voltage-controlled electrohydrodynamic jet printing of silver nano-ink. *Applied Physics A*, 99(4), 763-766.
- [129] Kang, D., Lee, M., Kim, H., James, S., & Yoon, S. (2011). Electrohydrodynamic pulsed-inkjet characteristics of various inks containing aluminum particles. *Journal of Aerosol Science*, 42(10), 621-630.
- [130] Xu, L., Wang, X., Lei, T., Sun, D., & Lin, L. (2011). Electrohydrodynamic deposition of polymeric droplets under low-frequency pulsation. *Langmuir*, 27(10), 6541-6548.
- [131] Onses, M. S., Sutanto, E., Ferreira, P. M., Alleyne, A. G., & Rogers, J. A. (2015). Mechanisms, capabilities, and applications of high - resolution electrohydrodynamic jet printing. *Small*, 11(34), 4237-4266.
- [132] Forbes, T. P., Degertekin, F. L., & Fedorov, A. G. (2010). Electrohydrodynamics of charge separation in droplet-based ion sources with time-varying electrical and mechanical actuation. *Journal of the American Society for Mass Spectrometry*, 21(4), 501-510.
- [133] Kim, H., Song, J., Chung, J., & Hong, D. (2010). Onset condition of pulsating cone-jet mode of electrohydrodynamic jetting for plane, hole, and pin type electrodes. *Journal of Applied Physics*, 108(10), 102804.
- [134] Lee, M. W., Kim, N. Y., & Yoon, S. S. (2013). On pinchoff behavior of electrified droplets. *Journal of Aerosol Science*, 57, 114-124.

- [135] López-Herrera, J., Popinet, S., & Herrada, M. (2011). A charge-conservative approach for simulating electrohydrodynamic two-phase flows using volume-of-fluid. *Journal of Computational Physics*, 230(5), 1939-1955.
- [136] Wei, C., Cai, L., Sonawane, B., Wang, S., & Dong, J. (2012). High-precision flexible fabrication of tissue engineering scaffolds using distinct polymers. *Biofabrication*, 4(2), 025009.
- [137] Ganan-Calvo, A., Davila, J., & Barrero, A. (1997). Current and droplet size in the electro spraying of liquids. Scaling laws. *Journal of Aerosol Science*, 28(2), 249-275.
- [138] Gañán-Calvo, A. M. (2004). On the general scaling theory for electro spraying. *Journal of fluid mechanics*, 507, 203-212a.
- [139] Wei, C., & Dong, J. (2014). Development and modeling of melt electrohydrodynamic-jet printing of phase-change inks for high-resolution additive manufacturing. *Journal of Manufacturing Science and Engineering*, 136(6), 061010.
- [140] Borra, J.-P., Ehouarn, P., & Boulaud, D. (2004). Electrohydrodynamic atomisation of water stabilised by glow discharge—operating range and droplet properties. *Journal of Aerosol Science*, 35(11), 1313-1332.
- [141] Mahoney, J. F., Yahiku, A. Y., Daley, H. L., Moore, R. D., & Perel, J. (1969). Electrohydrodynamic ion source. *Journal of Applied Physics*, 40(13), 5101-5106.
- [142] Choi, J., Kim, Y.-J., Lee, S., Son, S. U., Ko, H. S., Nguyen, V. D., & Byun, D. (2008). Drop-on-demand printing of conductive ink by electrostatic field induced inkjet head. *Applied Physics Letters*, 93(19), 193508.

- [143] Lee, S., Byun, D., Jung, D., Choi, J., Kim, Y., Yang, J. H., . . . Ko, H. S. (2008). Pole-type ground electrode in nozzle for electrostatic field induced drop-on-demand inkjet head. *Sensors and Actuators A: Physical*, 141(2), 506-514.
- [144] Lee, S., An, K., Son, S., & Choi, J. (2013). Satellite/spray suppression in electrohydrodynamic printing with a gated head. *Applied Physics Letters*, 103(13), 133506.
- [145] Lee, S., Kim, H., & Chung, J. (2012). Electro-hydrodynamic printing using hole-type electrode. *SPIE MOEMS-MEMS*, 82480J.
- [146] Park, S.-E., Lee, D.-Y., Kim, S.-Y., Shin, Y.-S., Yu, T.-U., & Hwang, J. (2008). *Design of electrohydrodynamic lens for stabilizing of eletrohydrodynamic jet printing*. Paper presented at the Journal of Physics: Conference Series.
- [147] Tse, L., & Barton, K. (2014). A field shaping printhead for high-resolution electrohydrodynamic jet printing onto non-conductive and uneven surfaces. *Applied Physics Letters*, 104(14), 143510.
- [148] Gao, F., & Sonin, A. A. (1994). *Precise deposition of molten microdrops: the physics of digital microfabrication*. Paper presented at the Proceedings of the Royal Society of London A: Mathematical, Physical and Engineering Sciences.
- [149] Choi, H. K., Park, J.-U., Park, O. O., Ferreira, P. M., Georgiadis, J. G., & Rogers, J. A. (2008). Scaling laws for jet pulsations associated with high-resolution electrohydrodynamic printing. *Applied Physics Letters*, 92(12), 123109.
- [150] Gonzalez, M., Axisa, F., Bulcke, M. V., Brosteaux, D., Vandeveldel, B., & Vanfleteren, J. (2008). Design of metal interconnects for stretchable electronic circuits. *Microelectronics Reliability*, 48(6), 825-832.

- [151] Jang, K. I., Jung, H. N., Lee, J. W., Xu, S., Liu, Y. H., Ma, Y., . . . Kim, B. H. (2016). Ferromagnetic, Folded Electrode Composite as a Soft Interface to the Skin for Long - Term Electrophysiological Recording. *Advanced functional materials*, 26(40), 7281-7290.
- [152] Myers, A. C., Huang, H., & Zhu, Y. (2015). Wearable silver nanowire dry electrodes for electrophysiological sensing. *RSC Advances*, 5(15), 11627-11632.